NASA CR-72345
AVSSD-0272-67-RR

MAGNETOPLASMADYNAMIC THRUSTOR RESEARCH

by

S. Bennett, G. Enos, R. John, and W. Powers

prepared for

NATIONAL AERONAUTICS AND SPACE ADMINISTRATION

Contract NAS 3-8907

AVCO MISSILES, SPACE AND ELECTRONICS GROUP
SPACE SYSTEMS DIVISION
Lowell Industrial Park
Lowell, Massachusetts 01852

Requests for copies of this report should be referred to

National Aeronautics and Space Administration
Office of Scientific and Technical Information
Attention: AFSS-A
Washington, D. C. 20546

NASA CR-72345
AVSSD-0272-67-RR

FINAL REPORT

MAGNETOPLASMADYNAMIC THRUSTOR RESEARCH

by

S. Bennett, G. Enos, R. John, and W. Powers

prepared for

NATIONAL AERONAUTICS AND SPACE ADMINISTRATION

May 21, 1967

Contract NAS 3-8907

Technical Management
NASA Lewis Research Center
Cleveland, Ohio
Electric Propulsion Office
Stanley Domitz

AVCO MISSILES, SPACE AND ELECTRONICS GROUP
SPACE SYSTEMS DIVISION
Lowell Industrial Park
Lowell, Massachusetts 01852

PRECEDING PAGE BLANK NOT FILMED.

MAGNETOPLASMADYNAMIC THRUSTOR RESEARCH

by

S. Bennett, G. Enos, R. John, and W. Powers

ABSTRACT

Radiation- and water-cooled MPD thrustors were operated in a range of power of 10 to 100 kilowatts, in the I_{sp} range 1000 to 5000 seconds, using ammonia as the propellant. Parametric studies were made of the effects of configuration, field strength, ambient pressure, propellant composition, and current on performance. A life test was made of a radiation-cooled thrustor at the 3000 second, 36 kilowatt level.

CONTENTS

CONTENTS (Concl'd)

ILLUSTRATIONS

ILLUSTRATIONS (Cont'd)

ILLUSTRATIONS (Concl'd)

TABLES

MAGNETOPLASMADYNAMIC THRUSTOR RESEARCH

by S. Bennett, G. Enos, R. John, and W. Powers

Avco Space Systems Division

SUMMARY

An extensive comparison of MPD arcjet performance for liquid-cooled and radiation-cooled configurations has been made. Tests were conducted with ammonia propellant of 2-inch-, 3-inch-, and 4-inch-diameter radiation-cooled designs having tungsten anodes and cathodes. Comparative data were obtained with water-cooled engines of the same internal geometry. In addition, parametric variations in throat diameter, mass flow, magnetic field strength, power level, test tank pressure, and propellant composition were carried out using water-cooled configurations to determine optimum performance conditions. A major conclusion derived from the experimental test program is that there is no significant difference in measured propulsion performance produced by the mode of engine cooling. The overall thrust efficiency in any case is poorer at very low mass flow rates, resulting in high engine temperatures for the radiation-cooled engine. The maximum power input which can be tolerated with the radiation-cooled version varies approximately with the arcjet linear dimensions. It is also concluded, based on a series of tests with water-cooled configurations, that there is no strong dependence upon throat size or throat configuration, at least in the range of 0.5- to 0.65-inch throat diameter. Beyond this range some flow instability develops at larger diameters, and some inability to handle the power develops at smaller diameters.

A radiation-cooled MPD arcjet design of 4-inch outside diameter appears to meet closely the objectives of the present study. A 75-hour lifetime test was performed on such an engine at the 3600-second, 34 percent overall efficiency level under exhaust environment conditions which were not optimum. Results of all tests performed indicate that at equivalent back pressures (about 100 microns), the performance of either the radiation- or the water-cooled MPD thrustor is substantially identical to test results reported by the NASA Lewis Laboratory on comparable designs. The improved performance noted on the NASA Lewis tests at very low back pressures suggests, therefore, about a 45 percent corresponding overall efficiency for the above test.

A formula to predict thrust, based on thrust mechanisms proposed previously, was compared to experimental data. According to this formula there are three important thrust producing mechanisms: aerodynamic forces, self-magnetic forces, and external magnetic forces. The contribution of each mechanism can be calculated from the current, the applied magnetic field, and the engine configuration (the latter within a rather restricted range of variation).

Analysis of the MPD arcjet discharge has been made using an analytical model of a j x B arc assuming one-dimensional, steady continuum fluid mechanics. The analysis considers the conservation relations for a three-fluid gas (electrons, ions, and neutrals) with appropriate transfer terms in mass, momentum, and energy for the three species. An applied axial magnetic field and an induced azimuthal

field is assumed. The voltage characteristic is an empirical input. Transport coefficients and reaction rates are deduced from experimentally determined cross sections. Solutions are obtained through a set of first-order ordinary differential equations which are solved on a high-speed digital computer. Results for hydrogen gas typify the physical processes occurring in the MPD arc, showing a strong discharge centered about the throat region of the nozzle. A low-pressure limit exists for the establishment of a high-current discharge and the current carried is pressure dependent.

A preliminary evaluation of a radiation-cooled magnetic field coil design and an associated magnet subsystem was made to establish a technical approach to this requirement. Comparisons of the system weights for aluminum or copper magnets, each with a 1-inch inner radius at 1 kilogauss (kG), show a requirement of about 2 or 3 percent of the engine power-supply weight. Aluminum has a weight advantage at fields below 1 kilogauss, and copper at fields above 1 kilogauss. The total magnet- and power-supply weight, within the approximations of the study, is less than 50 pounds, and the operating temperature is below 500°C. A Bitter-type magnet design shows promise as an efficient and practical solution for a self-cooling design.

A Bitter solenoid was constructed and tested. Its performance agreed closely with analytical predictions.

I. INTRODUCTION

A. PROGRAM OBJECTIVES

The general objectives of Research and Development of a Magnetoplasmadynamic Arc Thrustor, conducted under Contract NAS3-8907 with the NASA Lewis Research Center, have been to conduct experimental and analytical investigations of the Magnetoplasmadynamic (MPD) Arcjet Thrustor. The scope of the program includes analysis and experimental evaluation of factors which establish the efficiency and reliability of the MPD arc thrustor: (1) parametric studies of the optimization of MPD thrustors, (2) analytical and experimental studies of the acceleration mechanism, (3) analysis of the cooling requirements, and (4) magnetic field coil design and cooling requirements.

B. PROGRAM ORGANIZATION

The program originates with the Spacecraft Technology Procurement Section of the NASA Lewis Research Center. The NASA project manager is Mr. S. Domitz. The work on this contract was performed by the Avco Research and Technology Laboratories in the Aero-Plasma Physics Directorate under Dr. R. R. John. Dr. S. Bennett is associate project manager. Other principal Avco/SSD participants are Dr. A. Tuchman, Dr. A. Malliaris, Mr. W. Powers, and Mr. G. Enos. The Avco-Everett Research Laboratory personnel who directly assisted in the analytical effort on this program are Dr. R. Patrick, Dr. J. Workman, and Mr. A. Schneiderman.

C. BACKGROUND

1. Power Range

On the basis of best present estimates,[1-4] it appears that the development of power supplies within the next 10- to 15-year period will most likely be in the 5- to 50-kilowatt range. This power range has, therefore, been selected for primary attention in MPD thrustor development.

2. MPD Thrustor Performance

A number of laboratories[6-14] have carried out MPD thrustor research. Although the devices differ in detail, the basic configuration is as indicated in Figure 1. A summary performance curve[15] is given as Figure 2. Apart from a continued interest in increasing the overall efficiency, the major problems now pertain to the development of a long-life radiation-cooled configuration and to the determination of the effect of test environment on engine performance.

3. Propellant Characteristics

The most promising propellants presently under consideration for MPD thrustor operation are lithium and ammonia. The major advantage of lithium seems to reside in a smaller anode heating during operation. Therefore, its thermal efficiency is higher, leading to possibly higher overall efficiencies, and the anode heat rejection problem is less severe. The major advantages

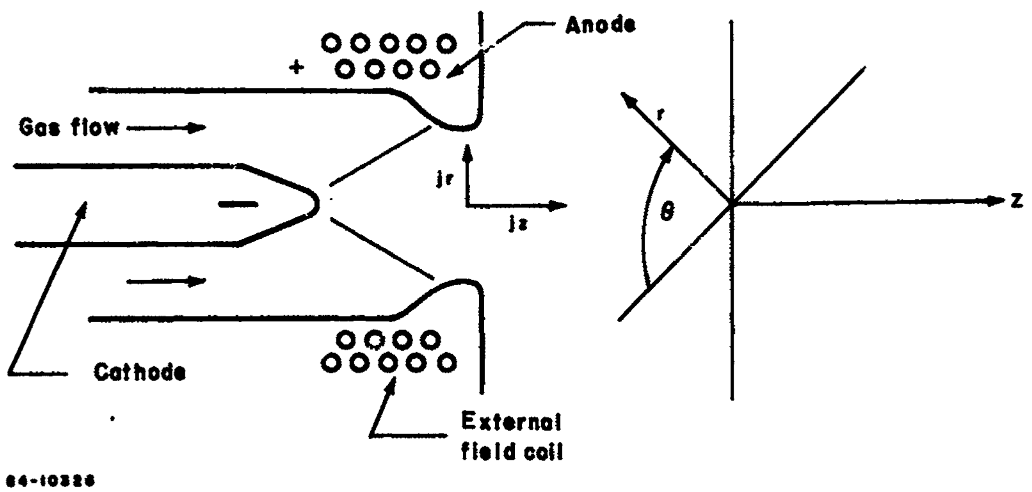

Figure 1 SKETCH OF GENERALIZED MPD THRUSTOR CONFIGURATION

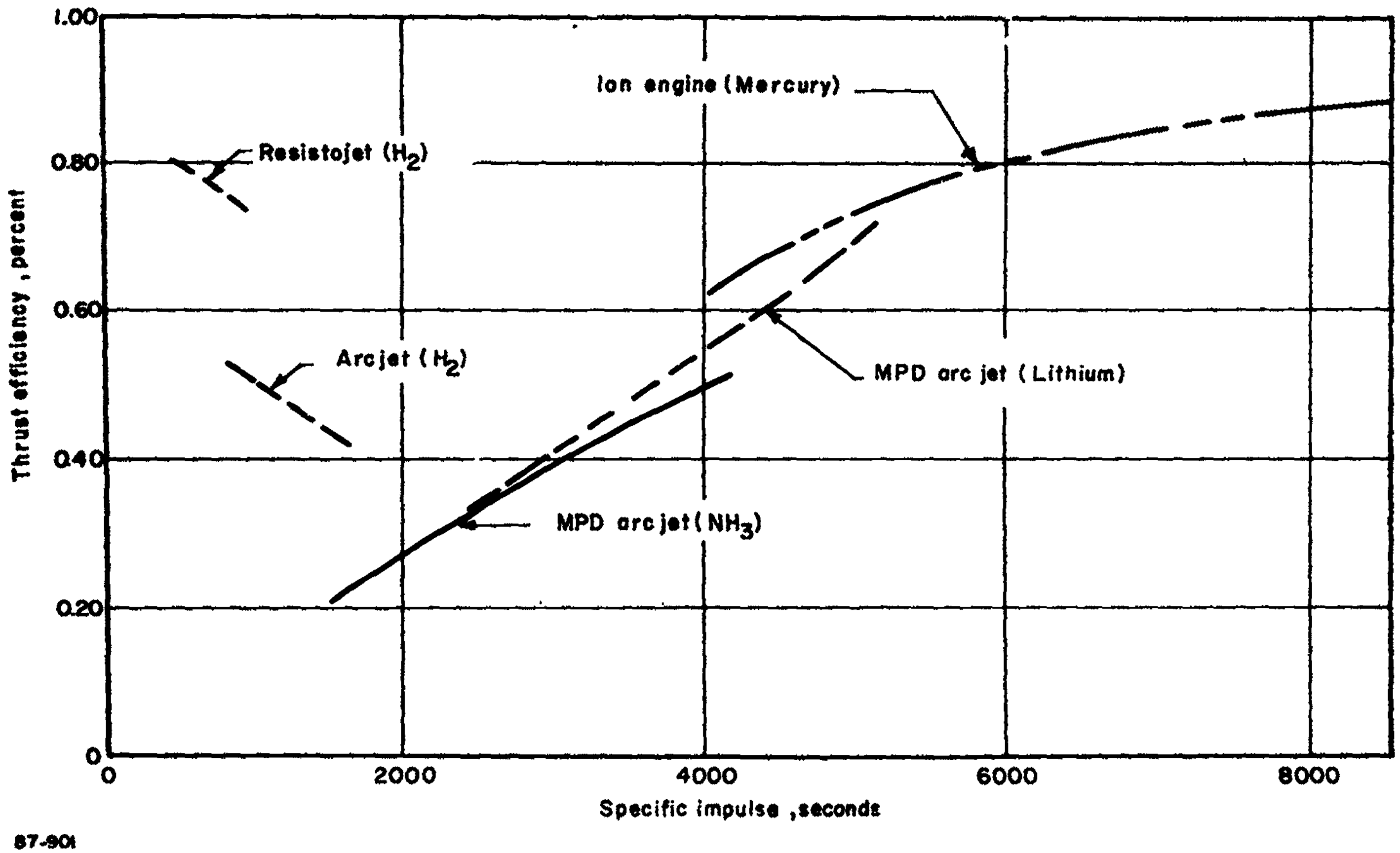

Figure 2 OVERALL EFFICIENCY VERSUS SPECIFIC IMPULSE

of ammonia are the avoidance of high temperatures in the feed system and the fact that space flight qualified ammonia feed systems have already been developed. Thus, major emphasis in this program has been upon ammonia.

4. Magnet Assembly

In the 5- to 50-kilowatt power range, MPD thrustors require external magnets. Although it is not definitively established, it appears that a solenoid of about 1 kilogauss axial field strength with an inner radius of one or two inches is adequate. Development of a magnet configuration to provide this field at minimum weight and/or power is desired.

5. Conclusions

The main objective of this program is, therefore, the development of a long-lived, radiation-cooled, ammonia-fueled MPD thrustor with minimum magnetic field requirement for the power range from 5 to 50 kilowatts.

II. EXPERIMENTAL RESULTS

A. EXPERIMENTAL VARIATION OF OPERATING PARAMETERS, WATER-COOLED

1. Introduction

A series of experiments have been performed on a sequence of water-cooled MPD arcjets operated with ammonia as the propellant. During the course of these measurements the quantities B (magnetic field strength), I (arc current), $\dot{m}$ (metered ammonia mass flow), and d (a characteristic thrustor dimension) have been systematically varied. The dependent variables V (arc voltage), and P_{amb} (the environmental tank pressure) have also varied but have not been controlled, except in one series of experiments where available external mass flow was used to control P_{amb}. Test results are given in Tables I through V.

2. Engine Configuration

Five engines were tested in the sequence. These engines have been designated X-7C-1 through X-7C-5. The engines have a common anode housing, magnet, and cathode assembly. They differ in the inner diameter of the straight throat section. A photograph of the X-7C series engines is given in Figure 3, and a sketch is presented in Figure 4. For comparison, the X-2C engine, which has been operated under a wide variety of conditions, is sketched in Figure 5. The essential difference is that the X-2C cathode lies upstream of a true throat, while the X-7C configuration is a straight one.

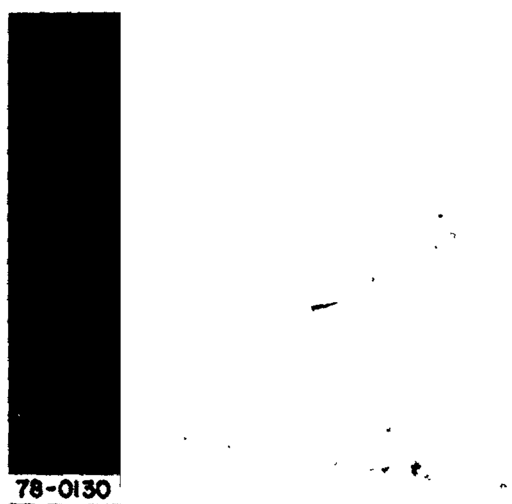

Figure 3 PHOTOGRAPH OF THE MPD CONFIGURATION X-7C USED FOR TESTS OF SENSITIVITY OF PERFORMANCE TO CONFIGURATION

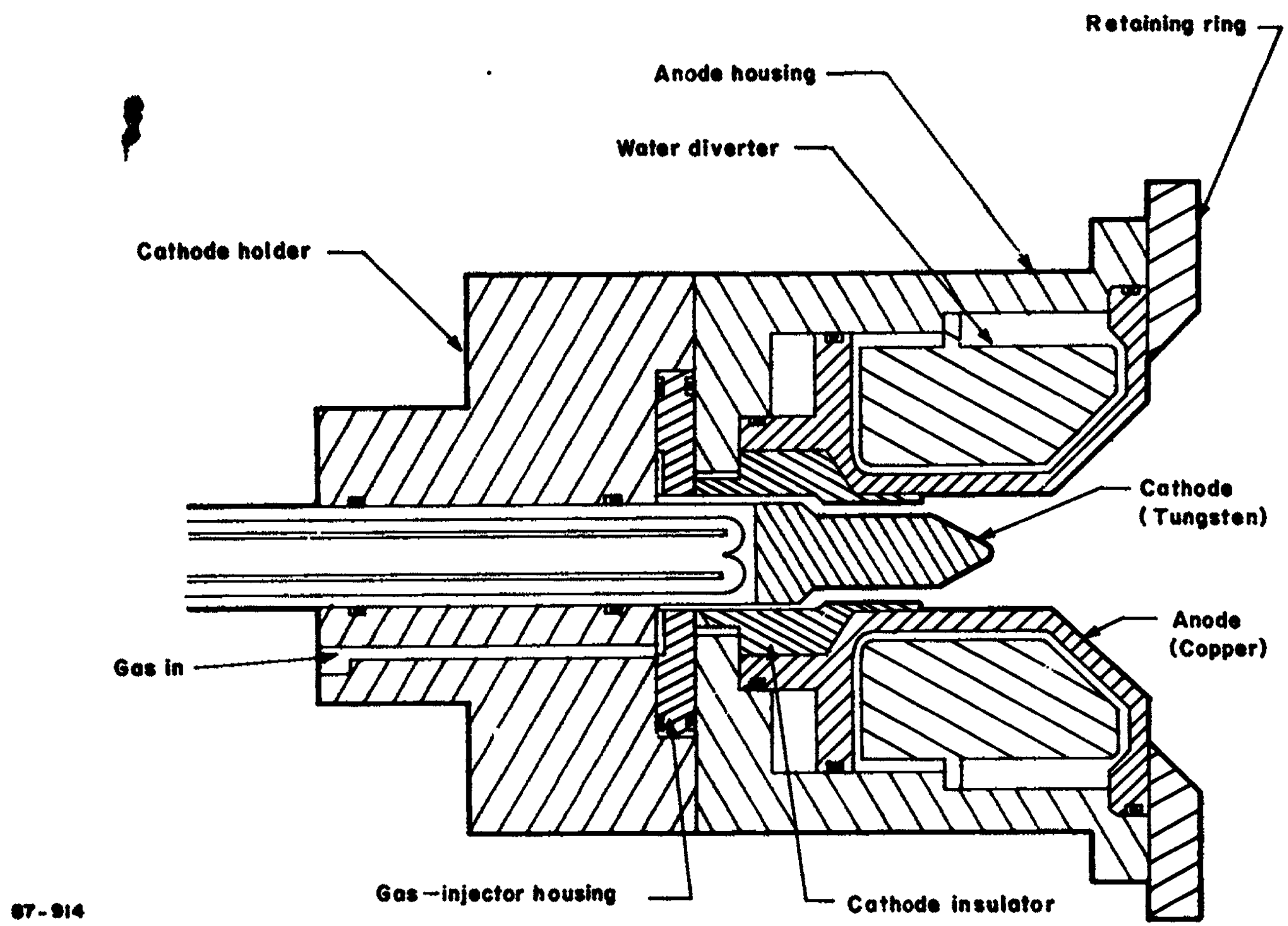

Figure 4 SCHEMATIC DRAWING OF X-7C MPD THRUSTOR

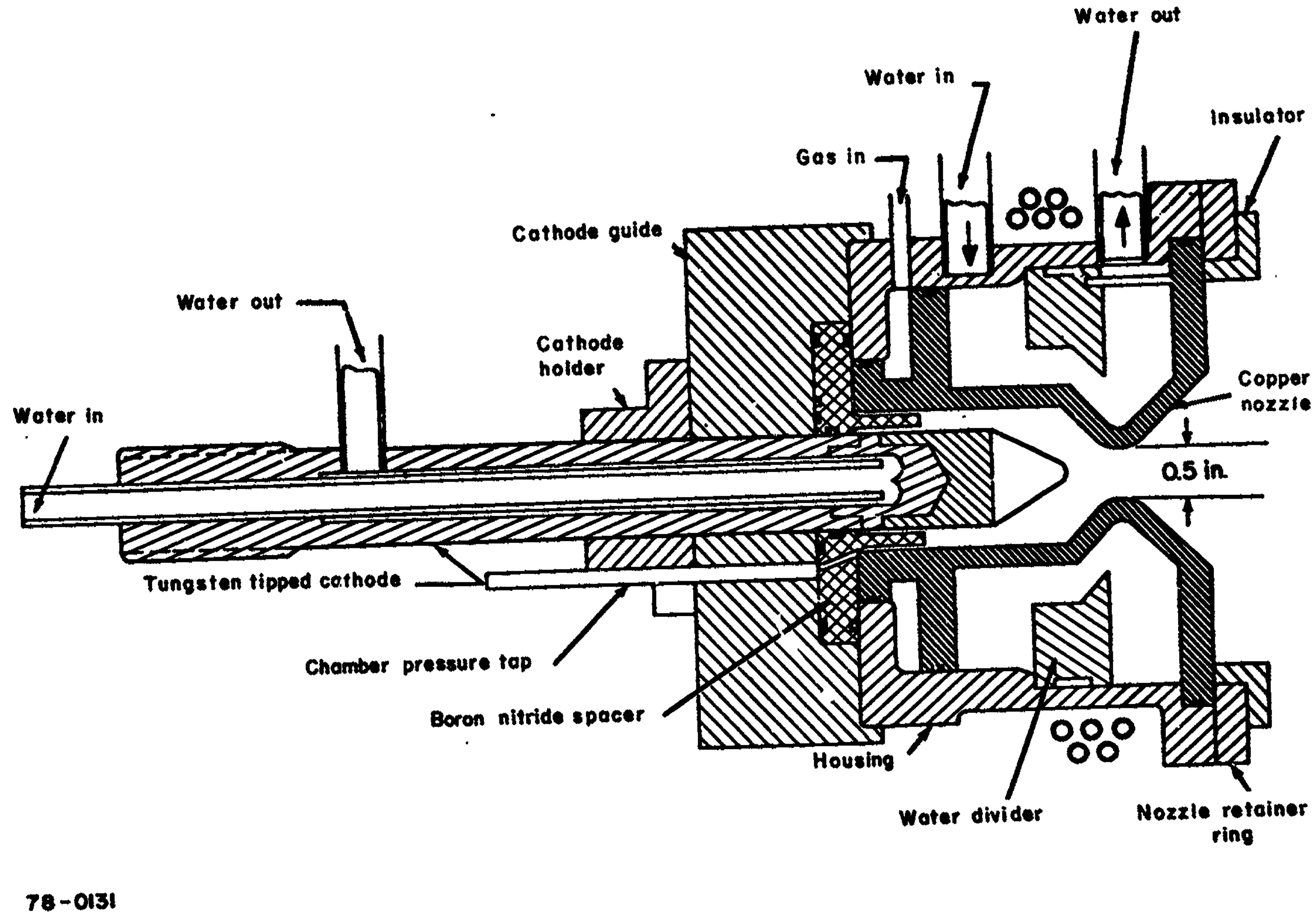

Figure 5 SCHEMATIC DRAWING OF THE X-2C MPD THRUSTOR

TABLE I

PERFORMANCE OF X-7C-1 ENGINE

Test	Current, amperes	Voltage, volts	Power, kW	Thrust, grams	Mass Flow, g/sec	Field Strength, kG	Anode Power, kW	Specific Impulse, sec	Efficiency, percent
1	300	69	20.7	31.9	.068	.83	14.0	470	3.5
2	400	64	25.6	39.9	.068	.83	16.9	590	4.4
3	500	63	31.5	47.8	.068	.83	19.5	700	5.1
4	600	61	36.6	57.5	.068	.83	22.8	850	6.4
5	800	61.5	49.2	78.3	.068	.83	29.0	1150	8.8
6	1000	66.5	66.5	105.	.068	.83	37.3	1540	11.7
7	1200	64	76.8	118.	.068	.83	40.6	1730	12.8
8	1400	62	86.8	134.	.068	.83	43.8	1960	14.6
9	300	64	19.2	31.9	.068	.83	13.7	470	3.7
10	300	64	19.2	28.5	.053	.83	13.7	540	3.8
11	400	62	24.8	38.3	.053	.83	15.6	720	5.4
12	500	60	30.0	44.7	.053	.83	17.9	840	6.0
13	600	60	36.0	54.2	.053	.83	20.8	1020	7.4
14	800	64	51.2	79.8	.053	.83	27.7	1500	11.2
15	1000	68	68.0	98.6	.053	.83	35.7	1850	13.0
16	1200	65	78.0	111.	.053	.83	40.6	2080	14.3
17	1400	61	85.5	128.	.053	.83	45.4	2400	17.4
18	300	64	19.2	28.5	.053	.83	14.0	540	3.8
19	300	65	19.5	25.4	.036	.83	13.0	700	4.4
20	400	60	24.0	33.5	.036	.83	14.6	930	6.3
21	500	57	28.5	39.9	.036	.83	16.9	1100	7.5
22	600	57	34.2	51.1	.036	.83	20.8	1420	10.2
23	800	58	46.4	67.1	.036	.83	26.0	1860	12.9
24	1000	64	64.0	89.3	.036	.83	32.5	2480	16.6
25	1200	65	78.0	105.	.036	.83	40.6	2910	18.8
26	1400	65	91.0	121.	.036	.83	47.1	3360	21.5
27	300	63	18.9	25.4	.036	.83	12.4	700	4.5
28	300	66	19.8	31.9	.068	1.25	10.7	470	3.6
29	400	63	25.2	41.5	.068	1.25	13.0	610	4.8
30	500	58	29.0	49.5	.068	1.25	15.2	730	6.0
31	600	54	32.4	54.3	.068	1.25	17.5	800	6.4
32	800	52	41.6	72.0	.068	1.25	24.6	1060	8.8
33	1000	52	52.0	92.6	.068	1.25	29.2	1360	11.6
34	1200	53	63.7	118.	.068	1.25	32.5	1580	15.5
35	1400	54	75.6	137.	.068	1.25	35.7	2000	17.5

TABLE I (Cont'd)

Test	Current, amperes	Voltage, volts	Power, kW	Thrust, grams	Mass Flow, g/sec	Field Strength, kG	Anode Power, kW	Specific Impulse, sec	Efficiency, percent
36	300	66	19.8	31.9	.068	1.25	10.7	470	3.6
37	300	66	19.8	28.7	.053	1.25	11.7	540	3.8
38	400	63	25.2	36.7	.053	1.25	14.6	690	4.8
39	500	55	27.5	38.3	.053	1.25	17.5	720	4.8
40	600	53	31.8	44.7	.053	1.25	20.1	840	5.7
41	800	51	40.8	60.7	.053	1.25	24.6	1140	8.2
42	1000	50	50.0	81.5	.053	1.25	28.8	1530	12.0
43	1200	49	58.8	102.	.053	1.25	31.4	1920	16.0
44	1400	49	68.7	118.	.053	1.25	35.7	2220	18.4
45	300	66	19.8	28.7	.053	1.25	11.7	540	3.8
46	300	65.5	19.6	23.9	.036	1.25	12.0	660	3.9
47	400	57	22.8	31.9	.036	1.25	14.6	890	6.0
48	500	54	27.0	38.3	.036	1.25	17.2	1060	7.2
49	600	52	31.2	43.2	.036	1.25	19.5	1200	8.0
50	800	47	37.6	55.8	.036	1.25	24.0	1540	10.9
51	1000	45	45.0	67.2	.036	1.25	28.2	1860	13.1
52	1200	45	54.0	79.8	.036	1.25	32.1	2210	15.7
53	1400	45	63.0	95.8	.036	1.25	37.0	2650	19.5
54	300	65	19.5	23.9	.036	1.25	12.0	660	3.9
55	300	72	21.6	35.1	.068	1.66	10.4	510	4.0
56	400	64	25.6	38.3	.068	1.66	13.7	560	4.0
57	500	62	31.0	49.6	.068	1.66	17.2	730	5.6
58	600	60	36.0	57.6	.068	1.66	20.8	850	6.5
59	800	58	46.4	76.8	.068	1.66	26.4	1120	9.0
60	1000	58	58.0	104.	.068	1.66	29.7	1520	13.2
61	1200	58	69.5	128.	.068	1.66	34.4	1880	16.7
62	1400	58.5	81.8	153.	.068	1.66	38.9	2240	20.2
63	300	73	21.9	35.1	.068	1.66	10.4	510	4.0
64	300	69	20.7	28.7	.053	1.66	11.7	540	3.6
65	400	65	26.0	36.7	.053	1.66	13.7	690	4.7
66	500	64	32.0	47.8	.053	1.66	17.9	900	6.5
67	600	63	37.8	60.7	.053	1.66	21.1	1140	8.8
68	800	56	44.8	70.3	.053	1.66	26.1	1320	10.
69	1000	54	54.0	92.6	.053	1.66	29.7	1740	14.3
70	1200	55	66.0	108.	.053	1.66	33.1	2030	16.1
71	1400	55	77.0	134.	.053	1.66	37.0	2520	21.1

TABLE I (Cont'd)

Test	Current, amperes	Voltage, volts	Power, kW	Thrust, grams	Mass Flow, g/sec	Field Strength, kW	Anode Power, kW	Specific Impulse, sec	Efficiency, percent
72	300	69	20.7	28.7	.053	1.66	11.7	540	3.6
73	300	69	20.7	27.1	.036	1.66	11.4	750	4.7
74	400	66	26.4	36.7	.036	1.66	14.6	1020	6.8
75	500	66	33.0	49.5	.036	1.66	18.2	1370	9.9
76	600	69	41.4	60.7	.036	1.66	22.8	1680	11.9
77	800	52	41.6	47.5	.036	1.66	24.7	1590	10.6
78	1000	50	50.0	76.8	.036	1.66	28.6	2030	15.7
79	1200	50	60.0	92.5	.036	1.66	33.1	2560	19.0
80	1400	51	71.4	111.	.036	1.66	38.6	3080	23.0
81	300	70	21.0	27.1	.036	1.66	11.4	750	4.7
82	300	75	22.5	35.1	.068	2.08	12.0	520	3.9
83	400	72	28.8	44.7	.068	2.08	15.6	660	4.9
84	500	70.5	35.2	57.4	.068	2.08	19.5	840	6.6
85	600	69	41.4	65.5	.068	2.08	22.8	960	7.4
86	800	64	51.2	84.5	.068	2.08	29.3	1240	9.9
87	1000	63	63.0	111.	.068	2.08	32.5	1630	13.8
88	1200	63	75.6	138.	.068	2.08	35.7	2020	17.9
89	1400	64	89.6	169.	.068	2.08	40.6	2480	22.5
90	300	75	22.5	35.1	.068	2.08	12.0	520	3.9
91	300	75	22.5	32.7	.053	2.08	12.3	620	4.3
92	400	73	29.2	44.2	.053	2.08	15.6	830	6.1
93	500	73	36.5	57.2	.053	2.08	19.5	1080	8.1
94	600	74	44.4	73.8	.053	2.08	23.7	1390	11.1
95	800	61	48.8	78.6	.053	2.08	28.6	1480	11.5
96	1000	59	59.0	105.	.053	2.08	30.9	1980	17.0
97	1200	59	70.8	131.	.053	2.08	34.7	2460	22.0
98	1400	59	82.6	154.	.053	2.08	37.9	2900	26.0
99	300	75	22.5	32.7	.053	2.08	12.3	620	4.3
100	300	77	23.1	30.3	.036	2.08	13.0	840	5.3
101	400	75	30.0	39.3	.036	2.08	15.9	1090	6.9
102	500	76	38.0	55.8	.036	2.08	20.2	1540	11.0
103	600	76	45.6	72.0	.036	2.08	24.4	1990	15.2
104	800	55	44.0	65.6	.036	2.08	27.6	1820	13.0
105	1000	54	54.0	84.5	.036	2.08	31.7	2340	17.7
106	1200	55	66.0	108.	.036	2.08	34.7	2990	23.6
107	1400	55	77.0	129	.036	2.08	37.9	3600	28.9

TABLE I (Concl'd)

Test	Current, amperes	Voltage volts	Power, kW	Thrust, gram	Mass Flow, g/sec	Field Strength, kG	Anode Power, kW	Specific Impulse, sec	Efficiency, percent
108	300	75	22.5	35.1	.068	2.08	12.0	520	3.9
109	300	85	25.5	36.7	.068	2.5	11.7	540	3.7
110	400	83	33.2	49.5	.068	2.5	15.2	730	5.2
111	500	82	41.0	67.1	.068	2.5	20.1	990	7.8
112	600	83	49.8	87.7	.068	2.5	24.7	1290	10.9
113	800	83	66.4	103.	.068	2.5	31.9	1510	11.3
114	1000	68	68.0	123.	.068	2.5	34.8	1800	15.7
115	1200	68	81.6	146.	.068	2.5	39.0	2140	18.5
116	1400	69	96.6	185.	.068	2.5	42.2	2720	25.0
117	300	85	25.5	36.7	.068	2.5		540	3.7
118	300	86	25.8	33.5	.053	2.5	13.0	630	4.0
119	400	84	33.6	49.4	.053	2.5	16.8	930	6.6
120	500	84	42.0	65.5	.053	2.5	20.8	1230	9.1
121	600	84	50.4	81.5	.053	2.5	25.3	1530	12.0
122	800	66	52.8	79.8	.053	2.5	29.2	1500	11.0
123	1000	65	65.0	111.	.053	2.5	34.1	2090	17.2
124	1200	65	78.0	136.	.053	2.5	38.	2560	21.5
125	1400	65	91.0	167.	.053	2.5	40.6	3150	27.8
126	300	86	25.8	33.5	.053	2.5		630	4.0
127	300	87	26.1	31.9	.036	2.5	13.0	890	5.2
128	400	85	34.0	46.3	.036	2.5	17.2	1280	8.4
129	500	85	42.5	63.9	.036	2.5	21.7	1770	12.8
130	600	86.5	51.9	79.8	.036	2.5	26.2	2210	16.4
131	800	61	48.8	86.5	.036	2.5	29.8	2400	20.4
132	1000	60	60.0	111.	.036	2.5	32.5	3080	27.4
133	1200	60	72.0	136.	.036	2.5	37.4	3800	34.7
134	1400	58	81.2	169.	.036	2.5	40.6	4690	47.0
135	300	86.5	25.9	31.9	.036	2.5		890	

TABLE II

PERFORMANCE OF X-7C-2 ENGINE

Test	Current amperes	Voltage, volts	Power, kW	Thrust, grams	Mass Flow, g/sec	Field Strength, kG	Anode Power, kW	Specific Impulse, sec	Efficiency, percent
1	300	85	25.5	14.8	.0088	.9	16.1	1680	7.
2	400	87	34.8	25.1	.0088	.9	21.0	2850	9.8
3	500	81	40.5	35.4	.0088	.9	26.0	4020	14.8
4	300	87	26.1	14.8	.0068	.9	16.1	2180	6.
5	400	91	36.4	28.1	.0068	.9	22.4	3840	15.3
6	500	100	50.0	38.5	.0068	.9	31.7	5660	21.
7	300	125	37.5	23.6	.0048	.9	24.6	4920	14.8
8	400	123	49.2	35.4	.0048	.9	33.8	7370	25.5
9	500	120	60.0	41.5	.0048	.9	40.5	8640	28.7
10	300	115	34.5	28.1	.0163	1.8	16.9	1720	6.7
11	400	124	49.6	50.3	.0163	1.8	22.8	3080	15.
12	500	110	55.0	62.2	.0163	1.8	26.4	3810	20.7
13	300	137	41.1	37.1	.0163	1.8	17.6	2280	9.9
14	300	145	43.5	38.6	.0127	1.8	17.6	3040	13.
15	475	129	61.3	59.3	.0127	1.8	28.8	4660	21.7
16	400	125	50.0	44.4	.0127	1.8	23.6	3500	14.9
17	300	124	37.2	38.5	.0163	2.7	16.5	2360	11.7
18	400	126	50.4	56.3	.0163	2.7	22.8	3450	18.4
19	500	125	62.5	71.1	.0163	2.7	28.8	4360	23.8
20	300	160	48.0	44.4	.0127	2.7	21.1	3500	15.5
21	400	145	58.0	54.8	.0127	2.7	29.2	4320	19.6
22	500	140	70.0	73.1	.0127	2.7	35.1	5750	29.0

TABLE III

PERFORMANCE OF X-7C-3 ENGINE

Test	Current, amperes	Voltage, volts	Power, kW	Thrust, grams	Mass Flow, g/sec	Field Strength, kG	Anode Power, kW	Specific Impulse, sec	Efficiency, percent
1	400	135	54.0	46.7	.0088	1.8	12.0	5300	22.1
2	500	93	46.5	47.8	.0088	.9	23.8	5430	25.8
3	400	85	34.0	35.1	.0088	.9	18.9	3990	19.8
4	300	64	19.2	17.5	.0088	.9	11.7	1990	8.7
5	300	65	19.5	15.9	.0068	.9	11.7	2340	9.2
6	500	95	47.5	44.7	.0068	.9	22.8	6570	29.8
7	400	70	28.0	25.4	.0068	.9	15.6	3730	16.3
8	500	115	57.5	51.0	.0088	1.8	26.0	5800	24.7

TABLE IV

PERFORMANCE OF X-7C-4 ENGINE

Test	Current, amperes	Voltage, volts	Power, kW	Mass. Flow, g/sec	Thrust, grams	Field Strength, kG	Anode Power, kW	Specific Impulse, sec	Efficiency, percent
1	300	46	13.8	.068	34.6	.83	10.4	510	6.1
2	400	45	18.0	.068	38.1	.83	12.8	560	5.7
3	500	43	21.5	.068	43.3	.83	15.1	635	6.1
4	600	42	25.2	.068	48.4	.83	17.5	710	6.6
5	800	41.5	33.2	.068	58.8	.83	22.2	865	7.4
6	1000	41.5	41.5	.068	71.0	.83	26.6	1040	8.6
7	1200	41.5	49.8	.068	83.1	.83	30.2	1220	9.8
8	1400	41.5	58.2	.068	91.8	.83	32.9	1350	10.0
9	300	46	13.8	.068	34.6	.83	10.4	510	6.1
10	300	45.5	13.7	.053	25.9	.83	10.4	490	3.3
11	400	43	17.2	.053	27.6	.83	12.4	520	4.0
12	500	41.5	20.8	.053	34.6	.83	14.8	655	5.2
13	600	41	24.6	.053	38.1	.83	16.8	720	5.4
14	800	40	32.0	.053	50.2	.83	21.5	945	7.1
15	1000	40	40.0	.053	62.3	.83	25.2	1070	8.8
16	1200	40	48.0	.053	76.2	.83	28.2	1430	10.9
17	1400	38	53.2	.053	86.5	.83	30.2	1630	12.7
18	300	45.5	13.7	.053	25.9	.83	10.4	490	3.3
19	300	45.	13.5	.036	19.0	.83	10.4	530	3.5
20	400	42.	16.8	.036	22.4	.83	12.1	620	4.0
21	500	40.	20.0	.036	27.6	.83	14.5	765	5.1
22	600	39.	23.4	.036	31.1	.83	16.5	865	5.2
23	800	37.	29.6	.036	45.0	.83	20.2	1250	9.2
24	1000	36.	36.0	.036	55.4	.83	23.2	1540	11.4
25	1200	35.	42.0	.036	64.0	.83	25.2	1770	13.0
26	1400	34.	47.7	.036	72.7	.83	27.9	2010	14.8
27	300	45.	13.5	.036	19.0	.83	10.4	530	3.5
28	300	40.	12.0	.016	12.1	.83	9.0	760	3.7
29	400	36	14.4	.016	17.2	.83	10.7	1080	6.2
30	500	35	16.5	[illegible]	19.0	.83	12.8	1190	6.6
31	600	33	19.8	.016	22.4	.83	14.5	1400	7.6
32	800	32	25.6	.016	31.1	.83	17.5	1940	11.3
33	1000	32	32.0	.016	38.1	.83	20.8	2380	13.6
34	1200	32.5	39.0	.016	46.7	.83	24.5	2910	16.8

TABLE IV (Cont'd)

Test	Current, amperes	Voltage, volts	Power, kW	Mass Flow, g/sec	Thrust, grams	Field Strength, kG	Anode Power, kW	Specific Impulse, sec	Efficiency, percent
35	1400	34.5	48.3	.016	51.9	.83	30.2	3240	16.8
36	300	40	12.0	.016	12.1	.83	9.4	760	3.7
37	300	40.5	12.2	.0127	12.1	.83	9.0	950	4.5
38	400	36	14.4	.0127	13.7	.83	10.7	1080	4.9
39	500	34	17.0	.0127	17.3	.83	12.1	1360	6.7
40	600	32	19.2	.0127	20.7	.83	14.1	1630	8.5
41	800	31	24.8	.0127	27.6	.83	16.8	2170	11.6
42	1000	32	32.0	.0127	34.6	.83	20.8	2720	14.2
43	1200	33	39.6	.0127	41.5	.83	25.9	3270	16.4
44	1400	37	51.8	.0127	46.7	.83	32.9	3670	15.9
45	300	40	12.0	.0127	12.1	.83	9.4	950	4.6
46	300	39	11.7	.0092	10.7	.83	8.4	1160	5.1
47	400	35	14.0	.0092	13.8	.83	10.4	1500	7.1
48	500	33	16.5	.0092	17.2	.83	12.1	1870	9.4
49	600	32	19.2	.0092	20.7	.83	14.1	2250	11.7
50	800	31	24.8	.0092	24.1	.83	17.5	2620	12.2
51	1000	32	32.0	.0092	29.3	.83	22.2	3180	14.0
52	1200	35	42.0	.0092	34.6	.83	28.2	3760	14.9
53	1400	36	50.4	.0092	39.8	.83	32.9	4330	16.4
54	300	45	13.5	.0092	17.3	.83	9.4	1880	11.4
55	300	38	11.4	.0088	12.1	.83	8.0	1380	7.1
56	400	36	14.4	.0088	15.5	.83	10.1	1760	9.1
57	500	35	17.5	.0088	20.7	.83	12.1	2350	13.4
58	600	44	26.4	.0088	34.6	.83	15.8	3930	24.8
59	800	47	37.6	.0088	41.5	.83	22.2	4720	25.0
60	1000	51	51.0	.0088	50.2	.83	28.2	5700	27.0
61	1200	39	46.8	.0088	41.5	.83	29.2	4720	20.0
62	1400	45	63.0	.0088	60.6	.83	33.6	6890	31.8
63	300	43	12.9	.0088	17.2	.83	8.4	1960	12.5
64	300	45	13.5	.0068	15.5	.83	8.4	2280	12.5
65	400	45	18.0	.0068	18.7	.83	10.7	2750	13.7
66	500	45	22.5	.0068	25.9	.83	13.1	3810	21.0
67	600	45	27.0	.0068	29.3	.83	16.1	4310	22.4
68	800	52	41.6	.0068	41.5	.83	22.5	6100	29.4

TABLE IV (Cont'd)

Test	Current, amperes	Voltage, volts	Power, kW	Mass Flow, g/sec	Thrust, grams	Field Strength, kG	Anode Power, kW	Specific Impulse, sec	Efficiency, percent
69	1000	49	49.0	.0068	46.7	.83	27.9	6870	31.5
70	1200	42	50.4	.0068	45.0	.83	30.2	6620	28.4
71	1400	47	65.8	.0068	53.7	.83	33.6	7900	31.0
72	300	45	13.5	.0068	15.5	.83	8.4	2280	12.5
73	300	46	13.8	.0048	15.5	.83	8.0	3230	17.3
74	400	49	19.6	.0048	20.7	.83	11.1	4310	21.8
75	500	50	25.0	.0048	25.2	.83	14.1	5250	25.4
76	600	54	32.4	.0048	32.9	.83	17.5	6850	33.4
77	800	55	44.0	.0048	41.5	.83	23.2	8650	39.2
78	1000	53	53.0	.0048	48.4	.83	28.2	10100	44.2
79	1200	45	54.0	.0048	45.0	.83	31.2	9380	37.5
80	1400	44	61.6	.0048	46.7	.83	~	9730	35.5
81	300	45	13.5	.0048	15.5	.83	8.0	3230	17.8
82	300	54	16.2	.068	31.9	1.25	9.0	470	4.5
83	400	50	20.0	.068	38.3	1.25	11.4	560	5.2
84	500	49	24.5	.068	46.2	1.25	13.8	680	6.1
85	600	48	28.8	.068	54.2	1.25	16.1	800	7.2
86	800	47	37.6	.068	68.6	1.25	20.5	1010	8.8
87	1000	47	47.0	.068	84.5	1.25	25.2	1240	10.7
88	1200	46.5	55.8	.068	101	1.25	29.2	1480	12.9
89	1400	46.5	65.0	.068	115	1.25	33.2	1690	14.3
90	300	54	16.2	.068	31.9	1.25	9.4	470	4.5
91	300	53	15.9	.053	22.3	1.25	9.0	420	2.8
92	400	50	20.0	.053	28.6	1.25	11.8	540	3.7
93	500	47	23.5	.053	36.7	1.25	13.8	690	5.2
94	600	46	27.6	.053	43.1	1.25	16.1	810	6.1
95	800	45	36.0	.053	57.4	1.25	20.5	1080	8.3
96	1000	45	45.0	.053	71.8	1.25	24.9	1350	10.4
97	1200	44	52.8	.053	86.2	1.25	28.2	1620	12.8
98	1400	44	61.6	.053	104	1.25	31.6	1950	18.6
99	300	53	15.9	.053	22.3	1.25	9.7	420	2.8
100	300	52	15.6	.036	19.1	1.25	9.7	530	3.1
101	400	46	18.4	.036	22.3	1.25	11.8	620	3.6
102	500	44	22.0	.036	28.7	1.25	13.8	800	5.0

TABLE IV (Cont'd)

Test	Current, amperes	Voltage, volts	Power, kW	Mass Flow, g/sec	Thrust, grams	Field Strength, kG	Anode Power, kW	Specific Impulse, sec	Efficiency, percent
103	600	43	25.8	.036	35.1	1.25	15.8	980	6.4
104	800	42	33.6	.036	49.5	1.25	19.8	1370	9.7
105	1000	41	41.0	.036	65.5	1.25	23.5	1810	14.0
106	1200	41	48.2	.036	75.0	1.25	26.2	2080	15.6
107	1400	40	56.0	.036	89.5	1.25	29.2	2480	19.1
108	300	51	15.3	.036	19.1	1.25	9.7	530	3.2
109	300	49	14.7	.016	14.3	1.25	9.0	890	4.2
110	400	42	16.8	.016	17.5	1.25	11.1	1090	5.5
111	500	41	20.5	.016	20.7	1.25	13.1	1290	6.3
112	600	38	22.8	.016	25.5	1.25	14.8	1590	8.5
113	800	36	28.8	.016	35.1	1.25	18.1	2190	12.9
114	1000	36	36.0	.016	44.7	1.25	21.8	2790	16.6
115	1200	37	43.2	.016	52.7	1.25	26.5	3290	19.3
116	1400	39	54.6	.016	63.8	1.25	31.2	3980	22.4
117	300	45	13.5	.016	14.3	1.25	9.0	890	4.5
118	300	44.5	13.3	.0127	12.7	1.25	8.7	1000	4.6
119	400	43	17.2	.0127	19.1	1.25	11.1	1500	8.0
120	500	42	21.0	.0127	25.5	1.25	13.8	2010	11.7
121	600	47	28.2	.0127	36.7	1.25	16.8	2890	18.1
122	800	37	29.6	.0127	33.5	1.25	19.1	2640	14.4
123	1000	36	36.0	.0127	43.1	1.25	22.5	3400	19.5
124	1200	37	44.4	.0127	47.8	1.25	27.6	3760	19.5
125	1400	39	54.7	.0127	57.5	1.25	32.6	4530	22.9
126	300	45	13.5	.0127	14.3	1.25	9.0	1130	5.7
127	300	46	13.8	.0092	14.3	1.25	8.7	1500	7.7
128	400	47	18.8	.0092	20.7	1.25	11.4	2040	11.9
129	500	50	25.0	.0092	28.7	1.25	14.4	2720	17.2
130	600	52	31.2	.0092	38.3	1.25	17.5	3390	24.6
131	800	52	41.6	.0092	47.8	1.25	22.5	5200	28.7
132	1000	39	39.0	.0092	46.3	1.25	24.2	5050	28.7
133	1200	40	48.0	.0092	51.1	1.25	29.2	5550	28.4
134	1400	42	58.8	.0092	60.7	1.25	33.2	6600	32.8
135	300	45	13.5	.0092	14.3	1.25	8.7	1500	7.9
136	300	45	13.5	.0088	14.3	1.25	8.7	1630	8.3

TABLE IV (Cont'd)

Test	Current, amperes	Voltage, volts	Power, kW	Mass Flow, g/sec	Thrust, grams	Field Strength, kG	Anode Power, kW	Specific Impulse, sec	Efficiency, percent
137	400	45	18.0	.0088	19.1	1.25	11.1	2170	11.0
138	500	43	21.5	.0088	22.3	1.25	13.4	2530	12.6
139	600	52	31.2	.0088	35.1	1.25	16.8	3990	21.6
140	800	54	43.2	.0088	51.2	1.25	22.8	5810	33.1
141	1000	54	54.0	.0088	63.8	1.25	27.9	7250	41.2
142	1200	51	61.2	.0088	68.7	1.25	31.9	7800	42.
143	1400	46	64.4	.0088	67.1	1.25	~	7630	38.2
144	300	46	13.8	.0088	14.3	1.25	9.0	1630	8.1
145	300	49	14.7	.0068	14.3	1.25	9.0	2100	10.
146	400	47	18.8	.0068	19.1	1.25	11.4	2810	13.7
147	500	47	23.5	.0068	25.5	1.25	13.8	3250	23.6
148	600	49	29.4	.0068	31.9	1.25	17.1	4690	24.5
149	800	55	44.0	.0068	51.2	1.25	22.6	7520	42.
150	1000	57.5	57.5	.0068	67.2	1.25	29.0	9880	55.5
151	1200	49	58.8	.0068	52.3	1.25	32.2	9150	46.7
152	1400	46	64.4	.0068	60.6	1.25	~	8920	40.4
153	300	49	14.7	.0068	14.3	1.25	9.0	2100	10.
154	300	52	15.6	.0048	14.3	1.25	9.0	2980	13.1
155	400	52	20.8	.0048	20.7	1.25	11.8	4320	20.6
156	500	55	27.5	.0048	28.7	1.25	14.5	5980	30.0
157	600	57.5	34.5	.0048	38.3	1.25	17.8	7980	42.5
158	800	62.5	50.0	.0048	54.3	1.25	23.5	11300	59.0
159	1000	57.5	57.5	.0048	57.5	1.25	29.2	12000	57.5
160	1200	51	61.2	.0048	57.5	1.25	33.6	12000	54.0
161	1400	54	25.6	.0048	70.3	1.25	~	14600	65.5
162	300	51	15.3	.0048	14.3	1.25	8.7	2980	13.3
163	300	57	17.1	.068	33.5	1.66	8.4	490	4.6
164	400	54	21.6	.068	39.9	1.66	10.0	590	5.2
165	500	52	26.0	.068	47.9	1.66	14.1	705	6.2
166	600	52	31.2	.068	55.8	1.66	18.2	820	7.0
167	800	52	41.6	.068	75.0	1.66	21.5	1100	9.6
168	1000	52	52.0	.068	94.	1.66	26.2	1380	12.0
169	1200	51	61.2	.068	113.	1.66	31.0	1660	14.8
170	1400	50.5	70.7	.068	128	1.66	35.2	1830	16.3
171	300	59.	17.7	.068	33.5	1.66	9.0	490	4.5

TABLE IV (Cont'd)

Test	Current, amperes	Voltage, volts	Power, kW	Mass Flow, g/sec	Thrust, grams	Field Strength, kG	Anode Power, kW	Specific Impulse, sec	Efficiency, percent
172	300	58	17.4	.053	23.9	1.66	9.4	450	3.0
173	400	52	20.8	.053	28.7	1.66	11.8	540	3.6
174	500	50	25.0	.053	36.7	1.66	13.8	690	4.9
175	600	49.5	29.7	.053	46.3	1.66	16.5	820	6.5
176	800	51	46.3	.053	67.2	1.66	20.8	1270	10.0
177	1000	51	51.0	.053	88.0	1.66	25.2	1650	13.7
178	1200	50	60.0	.053	103.0	1.66	29.6	1940	16.0
179	1400	47	65.8	.053	118.	1.66	33.6	2220	19.2
180	300	58	17.4	.053	23.9	1.66	9.4	450	3.0
181	300	57	17.1	.036	19.1	1.66	9.4	530	2.9
182	400	50	20.0	.036	23.5	1.66	11.8	650	3.7
183	500	50	25.0	.036	33.5	1.66	14.8	930	6.0
184	600	50	30.0	.036	39.9	1.66	16.8	1110	7.1
185	800	49	39.2	.036	57.5	1.66	21.5	1590	11.3
186	1000	50	50.0	.036	78.3	1.66	25.2	2170	16.3
187	1200	45	54.0	.036	91.	1.66	27.9	2520	20.4
188	1400	43	60.2	.036	104.	1.66	30.6	2880	24.0
189	300	57	17.1	.036	19.1	1.66	9.4	530	2.9
190	300	51	15.3	.016	12.7	1.66	9.0	790	3.1
191	400	50	20.0	.016	23.9	1.66	11.8	1490	8.5
192	500	50	25.0	.016	28.7	1.66	14.8	1790	9.9
193	600	50	30.0	.016	39.9	1.66	18.2	2490	15.9
194	800	50	40.0	.016	52.7	1.66	23.2	3290	20.8
195	1000	42	42.0	.016	51.2	1.66	26.2	3200	19.7
196	1200	42	50.4	.016	67.1	1.66	29.6	4200	26.8
197	1400	41	57.4	.016	75.0	1.66	34.2	4680	29.5
198	300	50	15.0	.016	12.7	1.66	9.4	790	3.2
199	300	50	15.0	.0127	14.3	1.66	9.4	1030	5.1
200	400	50	20.0	.0127	20.7	1.66	12.1	1630	8.1
201	500	51	25.5	.0127	28.7	1.66	14.8	2260	12.2
202	600	51	30.6	.0127	36.7	1.66	17.5	2890	16.6
203	800	51	40.8	.0127	49.5	1.66	23.5	3900	22.7
204	1000	53	53.0	.0127	67.1	1.66	28.6	5280	32.1
205	1200	49	58.8	.0127	68.7	1.66	33.0	5420	30.3
206	1400	45	[illegible]	.0127	70.3	1.66	–	5540	29.2

TABLE IV (Cont'd)

Test	Current, amperes	Voltage, volts	Power kW	Mass Flow, g/sec	Thrust, grams	Field Strength, kG	Anode Power, kW	Specific Impulse, sec	Efficiency, percent
207	300	50	15.0	.0127	14.3	1.66	9.0	1030	5.1
208	300	51	15.3	.0092	12.7	1.66	9.4	1380	5.5
209	400	51	20.4	.0092	20.7	1.66	11.4	2250	10.8
210	500	51	25.5	.0092	30.3	1.66	14.1	3300	19.7
211	600	52	31.2	.0092	33.5	1.66	17.5	3640	18.8
212	600	46	44.8	.0092	52.7	1.66	23.5	5720	32.3
213	1000	60	60.0	.0092	70.3	1.66	29.6	7640	43.
214	1200	50	60.0	.0092	65.6	1.66	34.6	7140	37.5
215	1400	50	70.0	.0092	68.7	1.66	40.2	6870	35.2
216	300	50	15.0	.0092	12.7	1.66	9.4	1380	5.6
217	300	50	15.0	.0088	12.7	1.66	9.0	1440	5.9
218	400	45	18.0	.0088	17.5	1.66	11.1	1990	9.3
219	500	43	21.5	.0088	23.9	1.66	16.5	2720	14.5
220	600	43	25.8	.0088	30.3	1.66	19.5	3440	19.4
221	800	49	39.2	.0088	49.5	1.66	22.2	5620	34.1
222	1000	58	58.0	.0088	68.7	1.66	32.2	7800	43.3
223	1200	59	20.8	.0088	83.1	1.66	35.6	9450	53.3
224	1400	51	71.4	.0088	72.0	1.66	41.2	8180	39.6
225	300	50	15.0	.0088	12.7	1.66	9.0	1440	5.9
226	300	50	15.0	.0068	12.7	1.66	8.7	1870	7.6
227	400	45	18.0	.0068	15.9	1.66	11.1	2340	10.0
228	500	45	22.5	.0068	20.7	1.66	13.5	3040	13.4
229	600	47	28.2	.0068	33.5	1.66	16.1	4930	28.1
230	800	43	34.4	.0068	47.8	1.66	22.5	7030	47.0
231	1000	50	50.0	.0068	70.3	1.66	28.9	10300	70.0
232	1200	55	66.0	.0068	70.3	1.66	36.7	10300	52.8
233	1400	53	74.2	.0068	70.3	1.66	42.9	10300	47.1
234	300	50	15.0	.0068	12.7	1.66	8.7	1870	7.6
235	300	48	14.4	.0048	11.2	1.66	8.0	2340	8.7
236	400	49	19.3	.0048	14.3	1.66	10.8	2980	10.6
237	500	55	27.5	.0048	30.3	1.66	14.5	6310	33.4
238	600	55	33.0	.0048	36.7	1.66	16.8	7650	40.8
239	800	61	48.8	.0048	59.1	1.66	23.6	12300	71.7
240	1000	64	64.0	.0048	78.2	1.66	29.2	16200	95.5
241	1200	64	76.8	.0048	88.0	1.66	-	18300	101.

TABLE IV (Cont'd)

Test	Current, amperes	Voltage, volts	Power, kW	Mass Flow, g/sec	Thrust, grams	Field Strength, kG	Anode Power, kW	Specific Impulse, sec	Efficiency, percent
242	1400	64	89.6	.0048	86.2	1.66	~	17900	83.
243	300	50	15.0	.0048	12.7	1.66	8.0	2640	10.7
244	300	65	19.5	.068	35.2	2.08	9.0	520	4.5
245	400	55	22.0	.068	41.5	2.08	12.1	610	5.5
246	500	55	27.5	.068	52.8	2.08	14.5	780	7.2
247	600	55	33.0	.068	62.3	2.08	18.1	910	8.3
248	800	55	44.0	.068	83.2	2.08	23.2	1220	11.1
249	1000	55	55.0	.068	105	2.08	24.8	1540	14.1
250	1200	55	66.0	.068	127	2.08	31.9	1860	17.2
251	1400	55	77.0	.068	14.0	2.08	35.2	2050	18.0
252	300	65	19.5	.068	35.2	2.08	9.3	520	4.5
253	300	65	19.5	.053	28.6	2.08	9.3	540	3.8
254	400	54	21.6	.053	33.5	2.08	12.8	630	4.7
255	500	50	25.0	.053	39.9	2.08	16.1	750	5.8
256	600	50	30.0	.053	51.2	2.08	18.8	960	7 9
257	800	51	40.8	.053	70.3	2.08	23.2	1320	12.1
258	1000	51	51.0	.053	101	2.08	28.2	1900	18.1
259	1200	51	61.2	.053	118	2.08	31.2	2220	20.6
260	1400	51	71.4	.053	135	2.08	34.5	2540	23.1
261	300	63	18.9	.053	30.3	2.08	10.1	570	4.6
262	300	52	15.6	.036	31.9	2.08	10.7	880	8.7
263	400	52	20.8	.036	41.5	2.08	13.8	1150	11.0
264	500	50	25.0	.036	51.	2.08	16.5	1410	13.9
265	600	50	30.0	.036	59.	2.08	18.1	1630	15.5
266	800	48	38.4	.036	78.	2.08	22.2	2160	21.1
267	1000	49	49.0	.036	84.5	2.08	25.9	2340	19.5
268	1200	46	55.2	.036	99	2.08	29.2	2740	23.6
269	1400	45	63.0	.036	111	2.08	33.6	3070	26.2
270	300	63	18.9	.036	31.9	2.08	10.7	880	7.2
271	300	53	15.9	.016	14.3	2.08	9.4	890	3.8
272	400	51	20.4	.016	19.1	2.08	12.1	1190	5.4
273	500	50	25.0	.016	28.7	2.08	14.8	1800	9.9
274	600	50	30.0	.016	36.7	2.08	17.8	2290	13.5
275	800	42	33.6	.016	44.8	2.08	21.2	2800	18 0

TABLE IV (Cont'd)

Test	Current, amperes	Voltage, volts	Power, kW	Mass Flow, g/sec	Thrust, grams	Field Strength, kG	Anode Power, kW	Specific Impulse, sec	Efficiency, percent
276	1000	42	42.0	.016	55.9	2.08	26.2	3490	22.4
277	1200	43	51.6	.016	67.2	2.08	31.2	4200	26.2
278	1400	45	63.0	.016	81.5	2.08	38.5	5150	31.7
279	300	52	15.6	.016	14.3	2.08	10.0	890	3.9
280	300	53	15.9	.0127	14.3	2.08	10.0	1120	4.9
281	400	51	20.4	.0127	22.3	2.08	12.8	1760	9.2
282	500	51	25.5	.0127	31.9	2.08	15.5	2510	15.0
283	600	52	31.2	.0127	38.3	2.08	18.1	3020	17.8
284	800	55	44.0	.0127	57.5	2.08	23.5	4530	28.4
285	1000	50	50.0	.0127	64	2.08	28.2	5050	31.1
286	1200	45	54.0	.0127	67.2	2.08	35.2	5290	31.6
237	1400	46	64.4	.0127	78.3	2.08	41.8	6160	36.1
288	300	50	15.0	.0127	14.3	2.08	10.7	1120	5.2
289	300	52	15.6	.0092	11.1	2.08	9.4	1210	4.1
290	400	50	20.0	.0092	19.1	2.08	12.1	2080	9.5
291	500	46	23.0	.0092	23.9	2.08	14.8	2690	13.0
292	600	45	27.0	.0092	28.7	2.08	16.8	3120	16
293	800	48	38.4	.0092	44.7	2.08	22.8	4850	27.2
294	1000	55	55.0	.0092	70.3	2.08	30.2	7650	47
295	1200	51	61.2	.0092	72.0	2.08	~	7830	44.2
296	1400	52	72.8	.0092	79.8	2.08	~	8680	45.8
297	300	47	14.1	.0092	11.1	2.08	~	1210	4.6
298	300	46	13.8	.0088	9.6	2.08	9.4	1090	3.7
299	400	44	17.2	.0088	14.3	2.08	11.8	1620	6.5
300	500	42	21.0	.0083	19.1	2.08	13.8	2170	9.5
301	600	41	24.4	.0088	25.5	2.08	16.1	2900	14.5
302	800	41	32.8	.0088	38.3	2.08	21.2	4350	24.4
303	1000	45	45.0	.0088	52.7	2.08	27.9	5980	33.7
304	1200	40	48.0	.0088	70.3	2.08	35.2	8000	56.2
305	1400	51	71.4	.0088	81.5	2.08	43.6	9260	51.0
306	300	45	13.5	.0088	9.6	2.08	-	1090	3.8
307	300	45	13.5	.0068	12.7	2.08	-	1870	8.4
308	400	47	18.8	.0068	19.1	2.08	-	2810	13.7
309	500	46	23.0	.0068	22.3	2.08	-	3280	15.3

TABLE IV (Cont'd)

Test	Current, amperes	Voltage, volts	Power, kW	Mass Flow, g/sec.	Thrust, grams	Field Strength, kG	Anode Power, kW	Specific Impulse, sec	Efficiency, percent
310	600	45	27.0	.0068	27.1	2.08	-	3980	19.2
311	800	46	36.8	.0068	43.1	2.08	-	6340	35.7
312	1000	45	45.0	.0068	49.5	2.08	-	7280	38.5
313	1200	50	60.0	.0068	70.3	2.08	-	10300	58.3
314	1400	56	78.4	.0068	73.5	2.08	-	10800	48.7
315	300	47	14.1	.0068	12.7	2.08	-	1870	8.1
316	300	50	15.0	.0048	12.7	2.08	8.7	3020	10.8
317	400	50	20.0	.0048	17.5	2.08	11.1	4170	15.3
318	500	51	25.5	.0048	23.8	2.08	14.8	5310	22.2
319	600	52	31.2	.0048	35.1	2.08	18.5	6500	39.6
320	800	60	48.0	.0048	55.8	2.08	24.9	10000	65.0
321	1000	66	66.0	.0048	81.5	2.08	30.2	13700	100
322	1200	70	84.0	.0048	111.	2.08	35.8	23000	147
323	1400	66	92.4	.0048	110	2.08	45.3	22900	131
324	300	50	15.0	.0048	12.7	2.08	9.4	3020	10.8
325	300	70	21.0	.068	44.7	2.50	9.0	660	6.7
326	400	58	23.2	.068	51.1	2.50	12.1	750	7.9
327	500	58	29.0	.068	60.6	2.50	15.1	890	8.9
328	600	58	34.8	.068	76.7	2.50	18.1	1120	11.9
329	800	60	48.0	.068	102	2.50	23.5	1500	15.3
330	1000	60	60.0	.068	127	2.50	27.9	1860	19.0
331	1200	60	72.0	.068	143	2.50	33.0	2100	20.0
332	1400	60	84.0	.068	168	2.50	-	3460	23.8
333	300	73	21.9	.068	44.7	2.50	9.0	660	6.4
334	300	68	20.4	.053	33.5	2.50	9.3	630	5.0
335	400	55	22.0	.053	36.7	2.50	12.8	690	5.6
336	500	53	26.5	.053	47.8	2.50	16.8	900	7.8
337	600	53	31.8	.053	57.4	2.50	18.8	1080	9.4
338	800	55	44.0	.053	86.2	2.50	23.6	1620	15.3
339	1000	55	55.	.053	111	2.50	27.6	2090	20.3
340	1200	55	66.	.053	137	2.50	31.2	2580	25.8
341	1400	55	77.	.053	153	2.50	34.2	2880	27.6
342	300	66	19.8	.053	33.5	2.50	10.0	630	5.1
343	300	57	17.1	.036	23.8	2.50	11.4	660	4.4

TABLE IV (Cont'd)

Test	Current, amperes	Voltage, volts	Power, kW	Mass Flow, g/sec	Thrust, grams	Field Strength, kG	Anode Power, kW	Specific Impulse, sec	Efficiency, percent
344	400	53	21.2	.036	25.5	2.50	14.1	710	4.1
345	500	51	25.5	.036	33.5	2.50	16.1	930	5.9
346	600	51	30.6	.036	51.1	2.50	19.1	1420	11.4
347	800	51	40.8	.036	76.6	2.50	22.9	2130	19.2
348	1000	51	51.0	.036	101	2.50	26.9	2800	26.7
349	1200	51	61.2	.036	122	2.50	29.9	3380	32.5
350	1400	50	70.0	.036	135	2.50	34.2	3640	34.8
351	300	55	16.5	.036	23.8	2.50	10.7	660	4.5
352	300	52	15.6	.016	14.3	2.50	12.1	890	4.0
353	400	49	19.6	.016	22.3	2.50	14.1	1400	7.6
354	500	46	23.0	.016	27.1	2.50	15.5	1700	9.6
355	600	45	27.0	.016	39.9	2.50	17.8	2490	17.8
356	800	45	36.0	.016	54.2	2.50	21.5	3400	24.5
357	1000	45	45.0	.016	70.2	2.50	26.2	4380	32.8
358	1200	45	54.0	.016	83.0	2.50	33.6	5180	38.3
359	1400	50	70.0	.016	102	2.50	40.2	6350	44.6
360	300	53	15.9	.016	14.3	2.50	10.8	890	3.9
361	300	50	15.0	.0127	12.7	2.50	11.4	1000	3.8
362	400	46	18.4	.0127	19.1	2.50	13.4	1500	7.5
363	500	45	22.5	.0127	25.5	2.50	15.5	2010	10.9
364	600	45	27.0	.0127	31.9	2.50	16.8	2510	14.3
365	800	45	36.0	.0127	47.8	2.50	21.5	3760	24.0
366	1000	45	45.0	.0127	67.0	2.50	27.9	5260	37.7
367	1200	50	60.0	.0127	83.0	2.50	34.9	6540	43.5
368	1400	50	70.0	.0127	99.0	2.50	42.9	7790	53.0
369	300	50	15.0	.0127	12.7	2.50	11.4	1000	3.8
370	300	50	15.0	.0092	11.1	2.50	10.0	1210	4.3
371	400	48	19.2	.0092	19.1	2.50	12.8	2080	10.0
372	500	45	22.5	.0092	27.1	2.50	14.8	2940	17.0
373	600	44	26.4	.0092	30.2	2.50	17.5	3280	18.0
374	800	45	36.0	.0092	46.2	2.50	22.2	5020	31.0
375	1000	50	50.0	.0092	62.2	2.50	28.9	6760	40.5
376	1200	55	66.0	.0092	78	2.50	35.9	8500	48.2
377	1400	55	77.0	.0092	91	2.50	45.2	9900	56.0

TABLE IV (Concl'd)

Test	Current, amperes	Voltage, volts	Power, kW	Mass Flow, g/sec	Thrust, grams	Field Strength, kG	Anode Power, kW	Specific Impulse, sec	Efficiency, percent
378	300	49	14.7	.0092	11.1	2.50	11.4	1210	4.3
379	300	50	15.0	.0088	12.7	2.50	10.7	1440	5.9
380	400	48	19.2	.0088	15.9	2.50	12.4	1810	7.3
381	500	45	22.5	.0088	22.3	2.50	14.8	2540	12.1
382	600	45	27.0	.0088	28.7	2.50	17.5	3260	16.6
383	800	50	40.0	.0088	46.3	2.50	24.9	5260	29.3
384	1000	56	56.0	.0088	70.3	2.50	31.9	8000	48
385	1200	53	63.5	.0088	94.3	2.50	40.2	10700	76.5
386	1400	61	85.4	.0088	103	2.50	46.8	11700	68.0
387	300	48	14.4	.0088	12.7	2.50	10.7	1440	6.1
388	300	50	15.0	.0068	12.7	2.50	10.1	1870	7.6
389	400	50	20.0	.0068	19.1	2.50	12.8	2810	12.9
390	500	49	24.5	.0068	25.5	2.50	15.8	3750	18.7
391	600	50	30.0	.0068	36.7	2.50	19.5	5400	31.7
392	800	58	46.4	.0068	59.1	2.50	26.6	8700	53.2
393	1000	63	63.0	.0068	83	2.50	33.6	12200	77.3
394	1200	69	82.7	.0068	107	2.50	40.2	15700	98.0
395	1400	70	98.0	.0068	132	2.50	48.6	19300	125
		65	91.0	.0068	118	2.50		17300	108
396	300	50	15.0	.0068	12.7	2.50	10.7	3310	15.3
397	300	55	16.5	.0048	15.9	2.50	10.7	3310	15.3
398	400	55	22.0	.0048	22.3	2.50	13.4	4650	22.6
399	500	58	29.0	.0048	31.9	2.50	16.5	6650	35.2
400	600	60	36.0	.0048	41.5	2.50	19.5	8650	48.0
401	800	65	52.0	.0048	60.6	2.50	25.6	12600	71.
402	1000	70	70.0	.0048	94.2	2.50	30.6	19600	94.
403	1200	75	90.0	.0048	121	2.50	36.8	25200	163
404	1400	72	101.0	.0048	129	2.50	45.3	26900	165
405	300	55	16.5	.0048	15.9	2.50	10.7	3310	15.3

TABLE V

PERFORMANCE OF X-7C-5 ENGINE

Test	Current, amperes	Voltage, volts	Power, kW	Mass Flow, g/sec	Thrust, grams	Field Strength, kG	Anode Power, kW	Specific Impulse, sec	Efficiency, percent
1	300	54	16.2	.068	35.1	2.08	10.2	520	5.4
2	400	52	20.8	.068	44.7	2.08	13.4	660	6.8
3	500	51	25.5	.068	47.8	2.08	16.5	700	6.3
4	600	51	30.6	.068	52.7	2.08	19.0	770	6.4
5	800	50.5	40.4	.068	65.5	2.08	25.0	960	7.5
6	1000	50	50.0	.068	76.7	2.08	30.1	1200	8.3
7	300	53	15.9	.068	35.1	2.08	10.2	520	5.5
8	300	52	15.6	.053	25.5	2.08	10.2	480	3.8
9	400	50	20.0	.053	30.3	2.08	13.6	570	4.2
10	500	49	24.5	.053	35.1	2.08	16.5	660	4.6
11	600	48	28.8	.053	39.9	2.08	19.4	750	5.0
12	800	47	37.6	.053	51.1	2.08	24.7	960	6.3
13	1000	46	46.0	.053	63.8	2.08	29.8	1200	8.0
14	300	51.5	15.4	.053	25.5	2.08	10.2	480	3.8
15	300	48.5	14.5	.036	17.5	2.08	9.8	490	2.8
16	400	46	18.4	.036	23.9	2.08	13.6	660	4.1
17	500	46	23.0	.036	28.7	2.08	16.2	800	4.8
18	600	45.5	27.3	.036	35.1	2.08	19.0	980	6.0
19	800	45	36.0	.036	47.8	2.08	24.1	1320	8.5
20	1000	42	42.0	.036	57.5	2.08	27.6	1600	10.5
21	300	48.5	14.5	.036	17.5	2.08	9.8	490	2.8
22	300	45	13.5	.016	12.7	2.08	9.5	790	3.6
23	400	43	17.2	.016	17.5	2.08	12.0	1090	5.3
24	500	42	21.0	.016	25.5	2.08	14.0	1590	9.3
25	600	40	24.0	.016	31.9	2.08	15.8	1990	12.7
26	800	35	28.0	.016	36.7	2.08	18.4	2290	14.5
27	1000	34	34.0	.016	38.3	2.08	22.8	2390	13.0
28	300	46	13.8	.016	12.7	2.08	9.5	790	3.6
29	300	45	13.5	.0127	12.7	2.08	8.9	1000	4.5
30	400	44	17.6	.0127	22.3	2.08	11.4	1750	8.5
31	500	42	21.0	.0127	27.1	2.08	13.4	2130	13.2
32	600	40	24.0	.0127	33.6	2.08	15.2	2640	17.8
33	800	35	28.0	.0127	35.1	2.08	17.8	2760	16.7
34	1000	34	34.0	.0127	38.3	2.08	23.1	3020	16.3
35	300	45	13.5	.0127	12.7	2.08	8.9	1000	4.5

TABLE V (Cont'd)

Test	Current, amperes	Voltage, volts	Power, kW	Mass Flow, g/sec	Thrust, grams	Field Strength, kG	Anode Power, kW	Specific Impulse, sec	Efficiency, percent
36	300	43	12.9	.0092	11.1	2.08	8.9	1210	5.0
37	400	43	17.2	.0092	19.1	2.08	9.8	2080	11.1
38	500	44	22.0	.0092	25.5	2.08	12.0	2770	15.4
39	600	40	24.0	.0092	31.9	2.08	14.3	3470	16.6
40	800	35	28.0	.0092	33.6	2.08	18.4	3650	17.5
41	1000	36	36.0	.0092	38.3	2.08	24.7	4160	21.3
42	300	43	12.9	.0092	11.1	2.08	8.9	1210	5.0
43	300	44	13.2	.0088	14.3	2.08	8.9	1620	8.1
44	400	43	17.2	.0088	20.7	2.08	8.9	2350	13.0
45	500	42	21.0	.0088	28.7	2.08	10.8	3260	20.4
46	600	41	24.6	.0088	33.6	2.08	12.0	3820	24.0
47	800	36	29.6	.0088	35.1	2.08	19.6	3990	21.7
48	1000	38	38.0	.0088	39.9	2.08	26.0	4540	21.8
49	300	43	13.9	.0088	14.3	2.08	8.9	1620	8.1
50	300	42	12.6	.0068	14.3	2.08	8.0	2100	11.5
51	400	42	16.8	.0068	19.1	2.08	11.4	2810	15.3
52	500	42	21.0	.0068	23.9	2.08	14.0	3510	19.2
53	600	42	25.2	.0068	30.3	2.08	16.5	4450	25.8
54	800	41	32.8	.0068	35.1	2.08	21.8	5160	26.6
55	1000	40	40.0	.0068	38.3	2.08	27.2	5630	27.1
56	300	40	12.0	.0068	14.3	2.08	8.2	2100	11.5
57	300	41	12.3	.0048	11.1	2.08	8.0	2310	10
58	400	44	17.6	.0048	15.9	2.08	11.1	3310	14.4
59	500	46	23.0	.0048	23.9	2.08	14.6	4970	24.8
60	600	46.5	27.9	.0048	28.7	2.08	17.4	5970	29.4
61	800	44	35.2	.0048	31.9	2.08	22.5	6640	29.0
62	1000	45	45.0	.0048	36.8	2.08	29.8	7670	30.1
63	300	36	10.8	.0048	8.0	2.08	7.6	1660	6.0
64	300	36	10.8	.068	25.5	.83	7.3	370	4.3
65	400	35	14.0	.068	27.1	.83	8.9	400	3.7
66	500	38	19.0	.068	35.2	.83	12.0	520	4.6
67	600	37	22.2	.068	38.3	.83	13.6	560	4.7
68	800	36	28.8	.068	44.8	.83	17.4	660	4.9
69	1000	36	36.0	.068	54.4	.83	22.2	800	5.8
70	300	45	13.5	.068	27.1	.83	8.9	400	3.8

TABLE V (Cont'd)

Test	Current, amperes	Voltage, volts	Power, kW	Mass Flow, g/sec	Thrust, grams	Field Strength, kG	Anode Power, kW	Specific Impulse, sec	Efficiency, percent
71	300	44	13.2	.053	22.3	.83	9.2	420	3.4
72	400	43	17.2	.053	25.5	.83	12.4	480	3.4
73	500	42	21.0	.053	28.7	.83	15.2	540	3.5
74	600	41	24.6	.053	31.9	.83	17.1	600	3.8
75	800	40	32.0	.053	41.5	.83	21.8	780	4.9
76	1000	38	38.0	.053	51.2	.83	25.0	960	6.3
77	300	43	12.9	.053	22.3	.83	9.5	420	3.5
78	300	43	12.9	.036	14.3	.83	10.2	400	2.1
79	400	41	16.4	.036	15.9	.83	12.4	440	2.0
80	500	38	19.0	.036	20.7	.83	14.0	580	3.0
81	600	36	21.6	.036	22.3	.83	16.5	620	3.1
82	800	35	28.0	.036	30.3	.83	19.6	840	4.4
83	1000	33	33.0	.036	36.7	.83	23.5	1020	5.5
84	300	41	12.3	.036	14.3	.83	9.8	400	2.2
85	300	36	10.8	.016	8.0	.83	7.95	500	1.8
86	400	35	14.0	.016	9.6	.83	10.1	600	2.0
87	500	35	17.5	.016	12.7	.83	13.0	790	2.8
88	600	35	21.0	.016	17.5	.83	15.2	1090	4.4
89	800	34	27.2	.016	23.9	.83	18.7	1490	6.3
90	1000	26	26.0	.016	15.9	.83	21.0	990	2.9
91	1000	29	29.0	.016	22.3	.83	21.6	1390	5.1
92	1000	33	33.0	.016	28.7	.83	22.2	1790	7.5
93	300	32	9.6	.016	8.0	.83	7.6	500	2.0
94	300	30	9.0	.0127	3.2	.83	6.7	250	.4
95	400	32	12.8	.0127	6.4	.83	9.8	500	1.2
96	500	33	16.5	.0127	9.6	.83	12.3	750	2.1
97	600	35	21.0	.0127	14.3	.83	15.5	1130	3.7
98	800	34	28.2	.0127	22.3	.83	19.0	1760	6.7
99	1000	34	34.0	.0127	31.9	.83	23.8	2510	11.3
100	300	30	9.0	.0127	3.2	.83	7.3	250	.4
101	300	56	16.8	.068	38.3	2.50	11.4	560	6.2
102	400	55	22.0	.068	47.8	2.50	14.9	700	7.4
103	500	54	27.0	.068	54.4	2.50	18.1	800	7.8
104	600	54	32.4	.068	62.3	2.50	20.9	910	10.2
105	800	53	42.4	.068	75.0	2.50	27.2	1100	9.4
106	1000	53	53.0	.068	89.5	2.50	31.4	1310	10.7
107	300	56	16.8	.068	38.3	2.50	11.1	560	6.2

TABLE V (Cont'd)

Test	Current, amperes	Voltage, volts	Power, kW	Mass Flow, g/sec	Thrust, grams	Field Strength, kG	Anode Power, kW	Specific Impulse, sec	Efficiency, percent
108	300	53	15.9	.053	31.9	2.50	11.7	600	5.8
109	400	52	20.8	.053	38.3	2.50	14.5	720	6.4
110	500	52	26.0	.053	44.8	2.50	17.4	850	7.0
111	600	51	30.6	.053	51.2	2.50	20.6	960	7.8
112	800	50.5	40.4	.053	64.0	2.50	26.3	1200	9.2
113	1000	50	50.0	.053	76.7	2.50	30.7	1440	10.7
114	300	53	15.9	.053	31.9	2.50	11.7	600	5.8
115	300	51	15.3	.036	19.1	2.50	11.1	530	3.2
116	400	48	19.2	.036	25.5	2.50	14.2	710	4.5
117	500	48	24.0	.036	31.9	2.50	17.4	890	5.6
118	600	48	28.8	.036	38.3	2.50	20.0	1160	6.8
119	800	47	37.6	.036	51.2	2.50	25.0	1420	9.3
120	1000	45	45.0	.036	64.0	2.50	28.5	1770	12.1
121	300	49	14.7	.036	19.1	2.50	10.8	530	3.3
122	300	45	13.5	.016	12.7	2.50	11.1	790	3.6
123	400	43	17.2	.016	19.1	2.50	13.0	1190	6.4
124	500	42	21.0	.016	27.1	2.50	14.9	1670	10.5
125	600	41	24.6	.016	31.9	2.50	16.5	1990	12.5
126	800	38	30.4	.016	39.9	2.50	20.0	2500	15.7
127	1000	37	37.0	.016	46.3	2.50	25.0	2890	17.4
128	300	43	12.9	.016	12.7	2.50	11.4	790	3.8
129	300	43	12.9	.0127	9.6	2.50	10 8	750	2.7
130	400	41	16.4	.0127	15.9	2.50	12.4	1250	5.8
131	500	40.5	20.3	.0127	25.5	2.50	14.0	2000	12.1
132	600	40.5	24.3	.0127	35.1	2.50	15.8	2760	19.1
133	800	40	32.0	.0127	44.7	2.50	20.6	3520	23.6
134	1000	39	39.0	.0127	47.9	2.50	26.3	3760	22.2
135	300	43	12.9	.0127	9.6	2.50	10.4	750	2.7
136	300	43	12.9	.0092	8.0	2.50	10.2	870	2.6
137	400	40	16.0	.0092	14.3	2.50	12.0	1560	6.7
138	500	39	19.5	.0092	22.3	2.50	13.6	2430	13.3
139	600	41	24.6	.0092	31.9	2.50	16.5	3470	20.6
140	800	42	33.6	.0092	40.0	2.50	22.5	4350	24.8
141	1000	41	41.0	.0092	44.7	2.50	28.2	4870	-25.4
142	300	41	12.3	.0092	8.0	2.50	10.4	870	2.7
143	300	41	12.3	.0088	8.0	2.50	9.8	910	2.8
144	400	39	15.6	.0088	14.3	2.50	11.4	1620	7.2
145	500	37	18.5	.0088	20.7	2.50	13.0	2350	12.7

TABLE V (Cont'd)

Test	Current, amperes	Voltage, volts	Power, kW	Mass Flow, g/sec	Thrust, grams	Field Strength, kG	Anode Power, kW	Specific Impulse, sec	Efficiency, percent
146	600	37	22.2	.0088	28.7	2.50	15.2	3260	20.3
147	800	42	33.6	.0083	40.0	2.50	22.5	4550	26.1
148	1000	41	41.0	.0088	43.2	2.50	29.8	4900	24.8
149	300	40	12.0	.0088	8.0	2.50	9.8	910	3.0
150	300	40	12.0	.0068	8.0	2.50	9.5	1170	3.8
151	400	38	15.2	.0068	11.1	2.50	11.4	1630	5.7
152	500	36	18.0	.0068	15.6	2.50	13.0	2300	9.6
153	600	37	22.2	.0068	21.9	2.50	15.5	3220	15.3
154	800	46	36.8	.0068	38.3	2.50	24.7	5630	28.3
155	1000	44	44.0	.0068	41.5	2.50	30.4	6100	27.6
156	300	38	11.4	.0068	8.0	2.50	9.5	910	3.1
157	300	39	11.7	.0048	6.4	2.50	9.2	1330	3.5
158	400	37	14.8	.0048	12.8	2.50	11.0	2660	11.0
159	500	38	19.0	.0048	19.1	2.50	13.3	3980	19.2
160	600	42	25.2	.0048	25.5	2.50	17.4	5310	25.8
161	800	49	39.2	.0048	40.9	2.50	25.6	8330	39.3
162	1000	46.5	46.5	.0048	41.5	2.50	31.0	8640	37.1
163	300	38	11.4	.0048	6.4	2.50	9.2	1330	36.0
164	300	51	15.3	.068	37.8	1.66	10.4	560	6.6
165	400	49	19.6	.068	41.5	1.66	14.0	610	6.2
166	500	49	24.5	.068	44.8	1.66	16.8	660	7.0
167	600	48	28.8	.068	51.2	1.66	20.6	750	6.4
168	800	46	36.8	.068	57.6	1.66	25.6	850	6.4
169	1000	45	45.0	.068	70.3	1.66	30.4	1030	7.8
170	300	51	15.3	.068	37.8	1.66	10.8	560	6.6
171	300	48	14.4	.053	28.7	1.66	11.0	540	5.2
172	400	46	18.4	.053	31.9	1.66	14.0	600	5.0
173	500	45	22.5	.053	33.6	1.66	16.8	630	4.5
174	600	44	26.4	.053	41.5	1.66	20.0	780	5.8
175	800	43.5	34.8	.053	49.6	1.66	25.6	940	6.5
176	1000	43	43.0	.053	59.2	1.66	30.1	1120	7.4
177	300	48	14.4	.053	28.7	1.66	10.4	540	5.2
178	300	46	13.8	.036	19.1	1.66	10.8	530	3.5
179	400	43	17.2	.036	20.7	1.66	14.0	570	3.3
180	500	42	21.0	.036	25.5	1.66	16.5	710	4.1
181	600	42	25.2	.036	31.9	1.66	19.4	880	5.4
182	800	41	32.8	.036	40.0	1.66	23.8	1110	6.5
183	1000	39	39.0	.036	49.6	1.66	26.6	1370	8.5

TABLE V (Cont'd)

Test	Current, amperes	Voltage, volts	Power, kW	Mass Flow, g/sec	Thrust, grams	Field Strength, kG	Anode Power, kW	Specific Impulse, sec	Efficiency, percent
184	300	44	13.2	.036	19.1	1.66	10.8	530	3.7
185	300	40	12.0	.016	8.0	1.66	9.5	500	3.3
186	400	38	15.2	.016	14.3	1.66	11.7	890	4.0
187	500	36	18.0	.016	17.5	1.66	13.6	1090	5.2
188	600	35	21.0	.016	20.7	1.66	15.2	1290	6.2
189	800	32	25.6	.016	27.1	1.66	18.4	1690	8.6
190	1000	31.5	31.5	.016	31.9	1.66	22.8	1980	9.7
191	300	40	12.0	.016	[illegible].0	1.66	9.5	500	3.3
192	300	37	11.1	.0127	6.4	1.66	8.6	500	1.4
193	400	35	14.0	.0127	11.1	1.66	10.2	870	3.3
194	500	34	17.0	.0127	14.3	1.66	12.0	1120	4.6
195	600	32	19.2	.0127	19.1	1.66	14.0	1500	7.2
196	800	31	24.8	.0127	25.5	1.66	17.4	2010	10.0
197	1000	31	31.0	.0127	31.9	1.66	22.2	2510	12.4
198	300	36	10.8	.0127	6.4	1.66	8.9	500	1.5
199	300	35	10.5	.0092	4.8	1.66	8.2	520	1.1
200	400	34	13.6	.0092	9.6	1.66	9.8	1040	3.5
201	500	33	16.5	.0092	15.9	1.66	11.4	1720	8.0
202	600	32	19.2	.0092	19.1	1.66	13.3	2070	10.0
203	800	32	25.6	.0092	25.5	1.66	16.4	2770	13.2
204	1000	33	33.0	.0092	30.3	1.66	23.1	3300	14.6
205	300	35	10.5	.0092	4.8	1.66	8.6	520	1.1
206	300	35.5	10.7	.0088	4.8	1.66	8.3	540	1.0
207	400	34	13.6	.0088	9.6	1.66	9.5	1090	3.7
208	500	32	16.0	.0088	14.3	1.66	11.7	1620	7.0
209	600	31.5	18.9	.0088	17.5	1.66	13.0	1990	8.8
210	800	32	25.6	.0088	25.5	1.66	17.8	2900	13.8
211	1000	35	35.0	.0088	31.9	1.66	24.4	3630	15.8
212	300	33	9.9	.0088	4.8	1.66	7.3	540	1.3
213	300	33	9.9	.0068	4.8	1.66	7.3	710	1.6
214	400	32	12.8	.0068	8.0	1.66	8.9	1170	3.5
215	500	32	16.0	.0068	14.3	1.66	10.8	2100	9.1
216	600	32	19.2	.0068	17.5	1.66	13.0	2580	11.2
217	800	33	26.4	.0068	22.3	1.66	18.4	3280	13.3
218	1000	37	37.0	.0068	30.3	1.66	26.6	4450	17.5
219	300	33	9.9	.0068	4.8	1.66	7.6	710	1.6

TABLE V (Cont'd)

Test	Current, amperes	Voltage, volts	Power, kW	Mass Flow, g/sec	Thrust, grams	Field Strength, kG	Anode Power, kW	Specific Impulse, sec	Efficiency, percent
220	300	32	9.6	.0048	3.2	1.66	7.0	670	1.1
221	400	31	12.3	.0048	8.0	1.66	8.9	1660	5.2
222	500	31	15.5	.0048	12.7	1.66	11.4	2650	10.0
223	600	32	19.2	.0048	15.9	1.66	14.0	3320	13.2
224	800	39	31.2	.0048	23.9	1.66	21.8	4980	18.3
225	1000	44	44.0	.0048	31.9	1.66	30.0	6650	23.2
226	300	32	9.6	.0048	3.2	1.66	7.3	670	1.1
227	300	32	9.6	.0027	3.2	1.66	6.7	1180	1.9
228	400	36	14.4	.0027	8.0	1.66	9.8	2960	7.9
229	500	42	21.0	.0027	14.3	1.66	13.3	5280	17.3
230	600	46	27.6	.0027	20.7	1.66	17.4	7650	27.6
231	800	49	39.2	.0027	27.1	1.66	25.4	10000	34.6
232	1000	51	51.0	.0027	33.5	1.66	33.3	12400	39.2
233	300	34	10.2	.0027	3.2	1.66	8.0	1180	1.8
234	300	55	16.5	.068	39.9	2.50	10.8	590	6.8
235	300	54	16.2	.053	33.5	2.50	11.1	630	6.3
236	300	51.5	15.5	.036	23.9	2.50	11.1	660	4.9
237	300	43	12.9	.016	15.9	2.50	10.8	990	5.9
238	300	41	12.3	.0127	12.7	2.50	9.8	1000	5.0
239	300	40	12.0	.0092	11.1	2.50	9.2	1210	5.4
240	300	37	11.1	.0052	11.1	2.50	8.9	2140	10.3
241	300	40	12.0	.0035	11.1	2.50	8.6	3180	14.1
242	300	43	12.9	.0029	12.7	2.50	8.6	4380	20.7
243	300	45	13.5	.0024	14.3	2.50	8.9	5960	30.3
244	300	50	15.0	.00185	15.9	2.50	9.2	8600	43.7
245	300	60	18.0	.00125	20.7	2.50	8.3	16500	91.0
246	300	71	21.3	.0007	25.5	2.50	8.6	36650	210.
247	400	45	18.0	.0035	15.9	2.50	12.8	4540	19.2
248	400	46	18.4	.0029	17.5	2.50	12.8	6030	27.7
249	400	50	20.0	.0024	19.1	2.50	12.8	8950	36.5
250	400	54	21.6	.00185	22.3	2.50	12.8	12000	62.8

TABLE V (Concl'd)

Test	Current, amperes	Voltage, volts	Power, kW	Mass Flow, g/sec	Thrust, grams	Field Strength, kG	Anode Power, kW	Specific Impulse, sec	Efficiency, percent
251	400	65	27.0	.00125	31.9	2.5	13.8	2550	145
252	400	44	17.6	.0035	15.9	2.5	12.8	4540	19.7
253	500	45	22.5	.0035	19.1	2.5	15.4	5460	22.2
254	500	49	24.5	.0029	23.9	2.5	16.5	9750	38.5
255	500	53	26.5	.0024	27.1	2.5	16.5	11300	55.5
256	500	61	30.5	.00185	31.9	2.5	16.8	17200	86.7
257	500	68	34.0	.00125	35.1	2.5	17.8	38100	14.0
258	500	49	24.5	.0035	22.3	2.5	16.8	6380	28.0
259	600	52	31.2	.0035	31.9	2.5	19.9	9100	44.8
260	600	55	33.0	.0029	33.6	2.5	19.9	11600	56.7
261	600	57	34.2	.0024	35.1	2.5	20.2	14600	72.3
262	600	65	39.0	.00185	36.7	2.5	21.5	19800	89.8
263	600	74	44.4	.00125	47.9	2.5	22.1	38300	19.8
264	600	54	32.4	.0035	31.9	2.5	19.9	9100	43.3
265	800	58	46.4	.0035	47.9	2.5	28.5	13700	68.
266	800	60	48.0	.0029	47.9	2.5	28.8	16500	79.3
267	800	62	49.6	.0024	51.2	2.5	28.8	21300	105
268	800	67.5	54.0	.00185	56.1	2.5	30.2	30300	151
269	800	74	59.2	.00125	59.2	2.5	30.8	47400	227
270	800	57.5	46.0	.0035	47.9	2.5	27.6	13700	68.
271	1000	59	50.0	.0035	59.2	2.5	36.2	16900	81.
272	1000	61	61.0	.0029	60.7	2.5	36.2	21000	100.
273	1000	65	65.0	.0024	62.3	2.5	37.6	25900	120.
274	1000	71	71.0	.00185	65.5	2.5	39.3	35300	157
275	1000	80	80.0	.00125	67.2	2.5	41.8	53700	217
276	1000	56	56.0	.0035	59.2	2.5		13700	86.

Throat dimensions for the X-7C series are listed in Table VI.

TABLE VI

THROAT DIMENSIONS OF X-7C ENGINES

Engine	Throat Diameter (inches)
X-7C-1	0.85
X-7C-2	1.25
X-7C-3	1.05
X-7C-4	0.60
X-7C-5	0.40

Note: Throat diameter of X-2C = 0.5 inch.

3. Discussion of Results

The X-7C engines are numbered in the order in which they were fabricated and tested. After operation of the X-7C-1 with 0.85-inch throat, the X-7C-2 with 1.25-inch throat was fabricated. This operated erratically in the power and mass flow ranges tested. The X-7C-3 was intended as intermediate between the X-7C-1 and X-7C-2, with a throat of 1.05 inches. This also operated erratically. At this point smaller thrustors were used, and these operated stably at 0.60 inch (X-7C-4) and 0.40 inch (X-7C-5). For data analysis we have concentrated upon the X-7C-1, -4, and -5, in the belief that the erratic operation of the X-7C-2 and -3 did not produce reliable data.

a. Anode Fall Voltage

The anode fall voltage, V_{an}, is defined as

$$V_{an} = \frac{P_{an}}{I} \qquad (1)$$

where P_{an} is the power delivered to the anode coolant, in watts, and I is the arc current in amperes. Based on the data of Tables I through V, the anode fall voltage decreases with current and increases with magnetic field. There is no clear-cut variation with throat diameter, although there is an indication that there may be an optimum for diameters near 0.6 inch, with generally higher anode fall voltages at 0.4 inch and 0.85 inch. The first two statements are exemplified in Figure 6, drawn from Table IV, and the final observation is indicated in Table VII below.

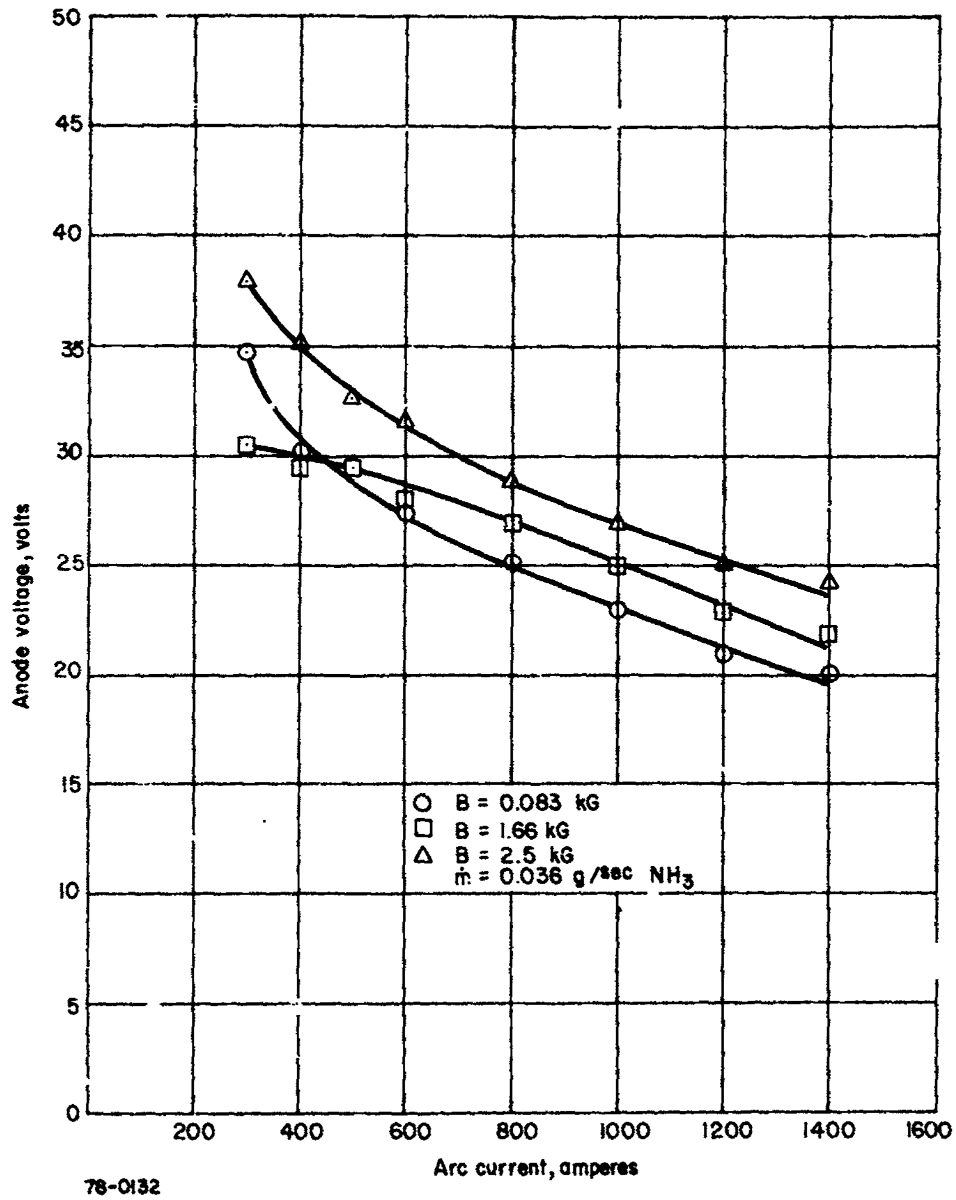

Figure 6 ANODE VOLTAGE VERSUS ARC CURRENT FOR X-7C-4 ENGINE

TABLE VII

VARIATION OF ANODE FALL VOLTAGE WITH THROAT DIAMETER
$\dot{m} \approx 0.036$ g/sec

I amperes	B kilogauss	Anode Fall Voltage d = 0.4-inch Volts	d = 0.6-inch Volts	d = 0.85-inch Volts
600	0.83	29.2	27.5	35.4
	1.66	34.2	28.0	39.4
1000	0.83	24.9	23.2	33.6
	1.66	28.3	25.2	29.6

b. Total Arc Voltage

The total arc voltage increases in general with B, with rare exceptions, and with the throat diameter. The behavior with arc current is not entirely monotonic; the voltage is higher at low currents (order of 300 amperes) than at intermediate currents (order of 800 to 1000 amperes) but then varies little with further current increase, occasionally even rising 1 or 2 percent at 1400 amperes. The behavior of arc voltage with B and I is shown in Figure 7, and the variation with throat diameter is indicated in Table VIII.

TABLE VIII

VARIATION OF ARC VOLTAGE WITH THROAT DIAMETER
$\dot{m} = 0.036$ g/sec

I amperes	B kilogauss	Arc Voltage d = 0.4-inch Volts	d = 0.6-inch Volts	d = 0.85-inch Volts
600	0.83	36	39	57
	1.66	42	50	69
1000	0.83	33	36	64
	1.66	39	50	50

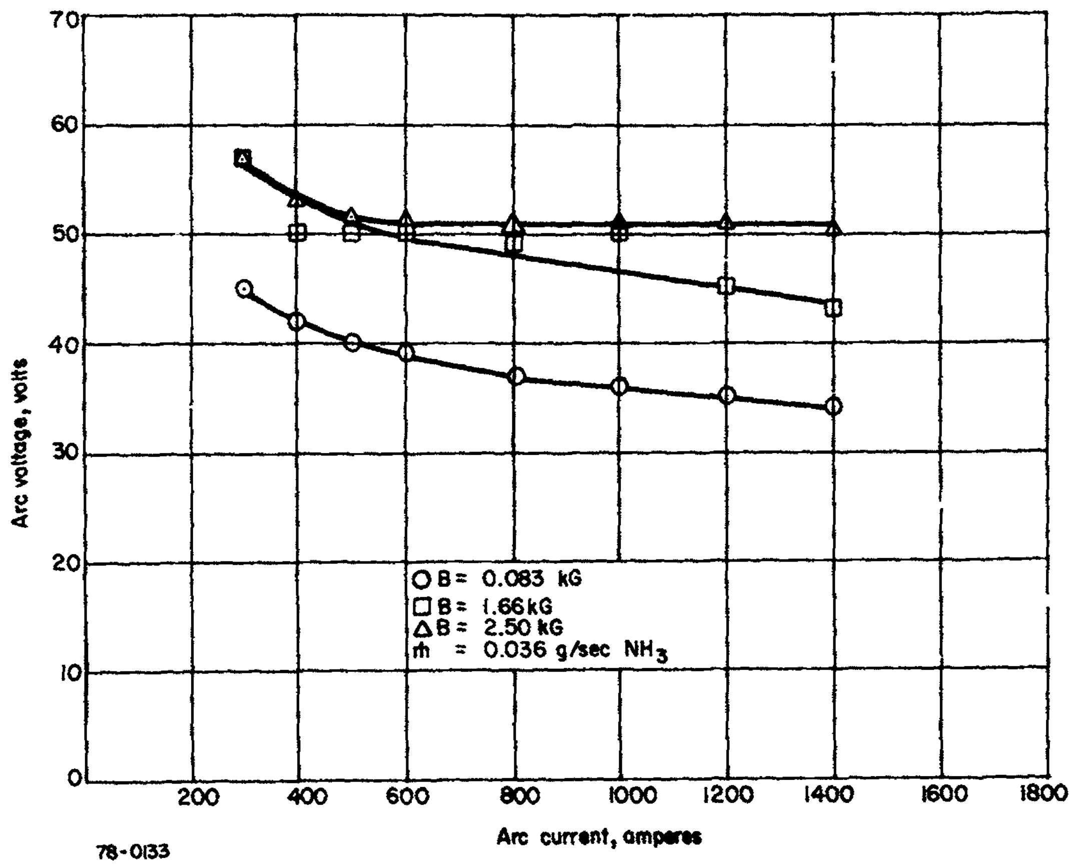

Figure 7 ARC VOLTAGE VERSUS ARC CURRENT FOR X-7C-4 ENGINE

c. Thermal Efficiency

The thermal efficiency is defined by

$$\epsilon_t = \frac{\textit{Power Input - Power to Engine Coolant}}{\textit{Power Input}} \qquad (2)$$

It is not evident from the definition, but is true as a practical matter, that

$$\epsilon_t = \frac{V - V_{an}}{V} \qquad (3)$$

The reason is that the heating of the cathode coolant is quite small relative to the heating of the anode coolant, so that

$$\textit{Power to Engine Coolant} = \textit{Power to Anode} + \textit{Power to Cathode}$$

$$\approx \textit{Power to Anode} = I\,V_{an}$$

Thus, the behavior of thermal efficiency with respect to variation in I, B, and throat diameter can be understood by reference to the behavior of V and V_{an}.

From Figures 6 and 7, V_{an} falls with increasing current at a rate greater than the rate at which V falls, so that ϵ_t increases, in general, with current. Further, the increase in V with B is, for the most part (but not always), more pronounced than the rise in V_{an} with B, so that the thermal efficiency usually increases as B is increased. Finally, referring to Tables VII and VIII, since the arc voltage increases fairly steadily with throat diameter while the anode fall has a minimum (for the engine tested) at 0.6 inch, the thermal efficiency is poorest for the 0.4-inch engine and about the same, on the average, for the other two. Figure 8 displays the variation of thermal efficiency as a function of current and magnetic field, while Table IX indicates the dependence of thermal efficiency on throat diameter.

TABLE IX

VARIATION OF THERMAL EFFICIENCY WITH THROAT DIAMETER

$\dot{m} = 0.036$ g/sec

I amperes	B kilogauss	Thermal Efficiency		
		d = 0.4 inch %	d = 0.6 inch %	d = 0.85 inch %
600	0.83	18.9	29.5	38.0
	1.66	18.6	44.0	42.9
1000	0.83	24.6	35.6	47.6
	1.66	30.1	49.6	40.8

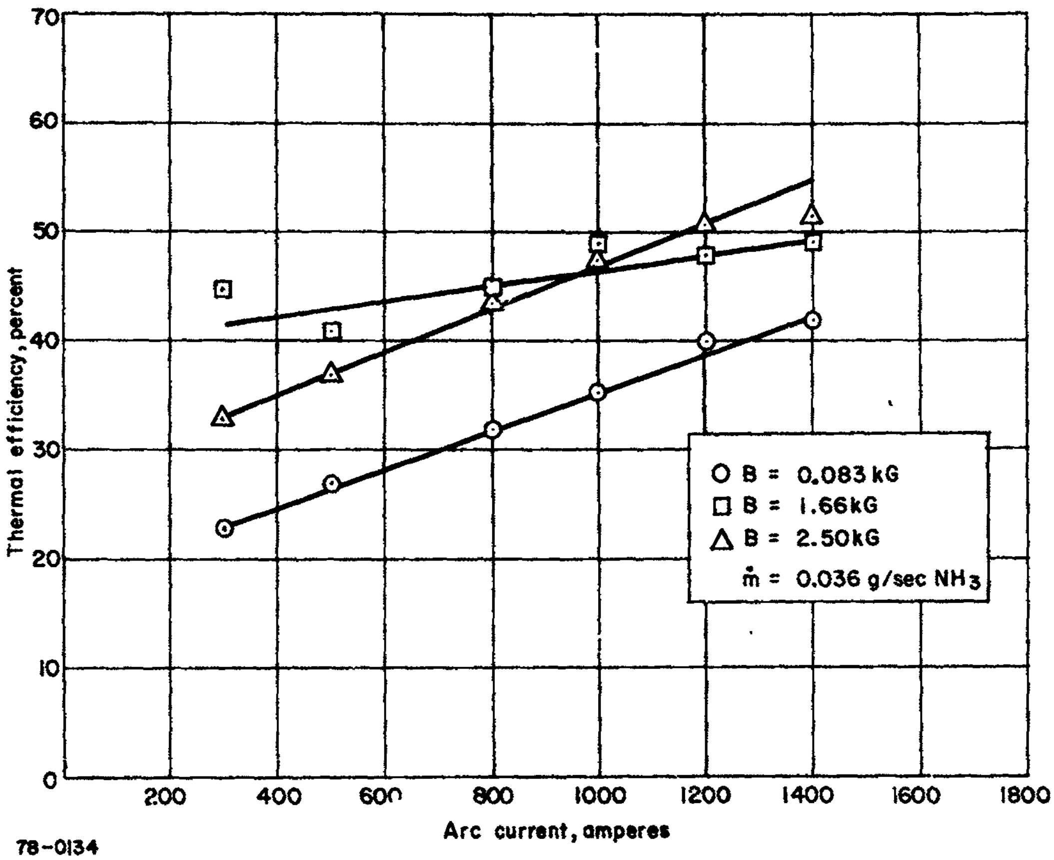

Figure 8 THERMAL EFFICIENCY VERSUS ARC CURRENT FOR X-7C-4 ENGINE

d. Thrust

The dependence of measured thrust upon I and B was determined from the data of Tables IV and V in the following way: First, at a number of fixed currents and mass flow rates, thrust was plotted as a function of magnetic field strength. For each current and mass flow rate, a linear fit was made to the data by inspection. It was observed that the slope of the line required to fit the data depended upon current, but not upon mass flow rate. Figure 9 is an example of the large number of curves drawn. Next, the slope of the T versus B curve was plotted as a function of current for the X-7C-4 and X-7C-5 engines, as indicated in Figure 10.

With the assumption[13, 14] that the thrust can be written as

$$T = f_1(IV, \dot{m}) + f_2(I) + KIB \tag{5}$$

where f_1 represents the thrust owing to aerodynamic forces and f_2 the thrust owing to self magnetic forces, then the plots of T versus B yield slopes equal to KI. When the slopes are plotted versus I, the slope of this second plot is K. To the extent that the contribution of the external magnetic field to the thrust can be represented by a term of the form KIB, each of these plots should be linear. Further, since K is thought to be related to a dimension of the discharge, there should be a difference in K between the X-7C-4 and X-7C-5 thrustors. According to Figure 10, this appears to be the case. For the X-7C-4 engine the points for the two lowest currents fall significantly off the curve, but each of the other points fits well on one of the two lines.

The absolute value of l, in the relation $T = lIB$, can also be calculated from the data for the two engines, and it is found to be 2.7 millimeters for the X-7C-4 engine and 1.75 millimeters for the X-7C-5 engine. In terms of actual spacing, the distance between the cathode (at the shoulder) and the straight section of the nozzle is, for the X-7C-4 engine, 2.86 millimeters, while for the X-7C-5 engine the distance between cathode shoulder and straight nozzle section is 1.90 millimeters.

It is, of course, somewhat arbitrary to define the relevant length from the cathode shoulder. If the cathode tip is used instead, the relevant distances are 3.8 and 2.54 millimeters, which agree much less well with the measured slopes.

Further, the X-7C-1 engine data do not fit the pattern indicated above. The correlation of thrust with B at constant I and $\dot{m}$ is relatively

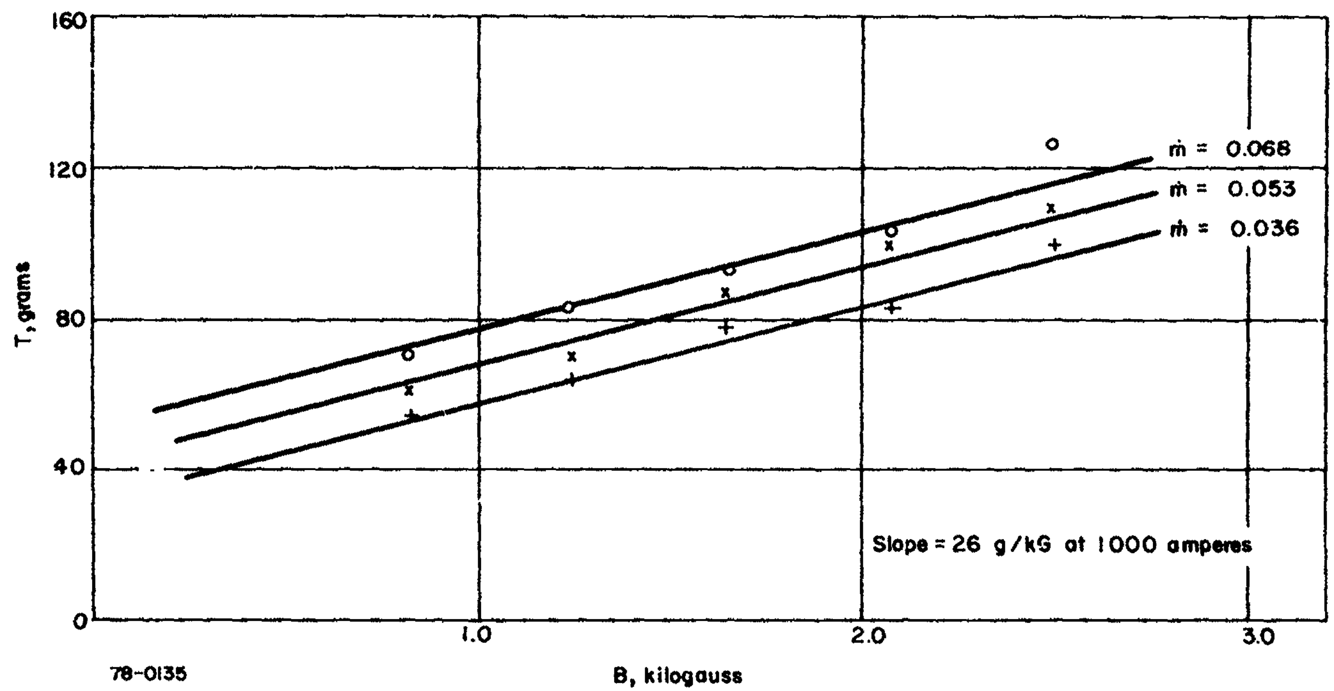

Figure 9 THRUST VERSUS APPLIED FIELD STRENGTH WITH DIFFERENT MASS FLOW RATES X-7C-4

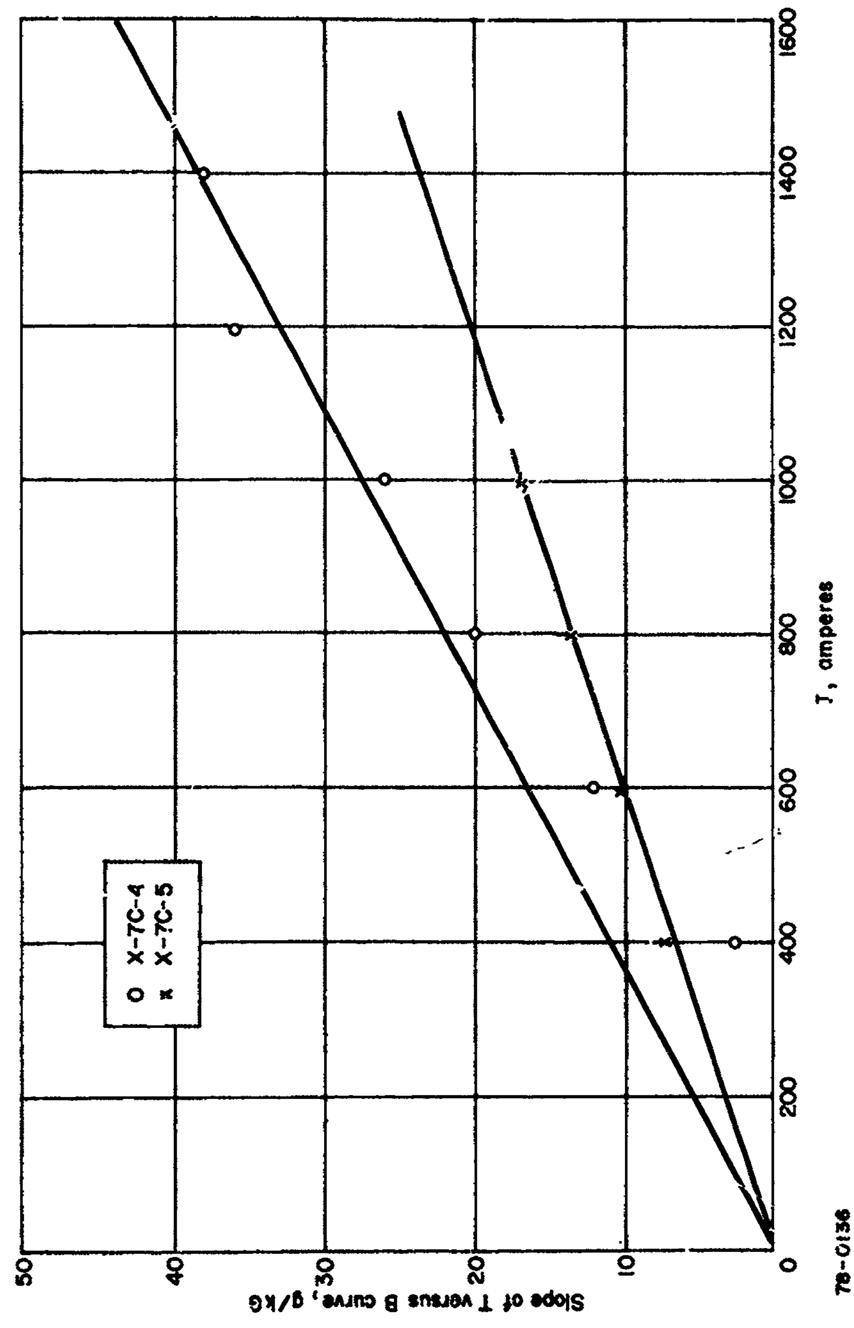

Figure 10 SLOPE OF T VERSUS B, AS A FUNCTION OF CURRENT

poor, and if best fits are used for this correlation, then the correlation of measured slopes with I is also poor. It is possible that the increased tendency of the thrustor to slip between low and high voltage modes is a source of this difficulty.

Still, the fairly clear indication that a portion of the thrust arising from the external field interaction can be correlated with I, B, and a thrustor dimension makes it worthwhile to attempt to write a thrust formula. We assume that the thrust is made up of three contributions: one originates in aerodynamic forces associated with the passage of gas through an arc discharge which raises the stagnation enthalpy; a second contribution arises from self-magnetic forces, which have been discussed in detail previously[13]; and a third contribution is produced by the external magnetic field and is equal to the product lIB. We assume, for convenience, that these forces are additive, although it is fairly clear that there must be some interaction between the fields which produce each force so that they should not, in practice, be strictly additive.

For the aerodynamic forces we assume simply that they are such as to impart a specific impulse of 350 seconds to the ammonia propellant. This is arbitrary but reasonably well grounded in experiment.[39] At very low mass flows and high powers the thermal I_{sp} may be somewhat higher than this, and at very high mass flows or low powers it can clearly be made as low as desired, but in the range of parameters of interest this assumption is fairly good. In any case the fraction of total thrust attributable to this term is small in the range of $I_{sp} > 2000$ sec, so even substantial errors would not greatly affect the results.

For the self-magnetic forces, we assume that the discharge leaves the cathode at the shoulder and proceeds radially to the anode. The formula to calculate thrust is already available, and the choice of discharge dimensions is fixed by the thrustor geometry, so that no further arbitrary choices are needed.

For the self-magnetic forces

$$T = \frac{I^2}{9.8 \times 10^4} \left(\frac{1}{2} + \ln \frac{r_a}{r_c} \right)$$

$$= 0.96 \times 10^{-5} I^2 \sim 10^{-5} I^2$$

For the external magnetic field forces, we assume that the force exerted on the propellant is given by lIB and that the rotational kinetic energy imparted to the flow by this force is recovered in the expansion, so that the thrust is also lIB.

Thus, the thrust formula can be written for the X-7C-4 and X-7C-5 thrustors as follows:

(X-7C-4)

$$T = 350\,\dot{m} + 10^{-5} I^2 + 2.86 \times 10^{-2} IB \qquad (6)$$

(X-7-C-5)

$$T = 350\,\dot{m} + 10^{-5} I^2 + 1.90 \times 10^{-2} IB \qquad (7)$$

In these expressions, T the thrust is given in grams for $\dot{m}$ in grams/second, I in amperes, and B in kilogauss. It should be noted that the ratio r_a/r_c happens to be identical for the two engines.

Figures 11 and 12 have been prepared to exhibit the extent to which the thrust formulas represent measured performance. In each case the quantities plotted are measured thrust versus predicted thrust, with the prediction based on both the thrust formula and the known operating conditions for each thrustor.

In each case the correlation is fairly good. In a first approximation the thrust is represented by the prediction to an accuracy of about 20 percent for most of the range of thrust presented. On closer inspection there appears to be a systematic deviation in the sense that the thrust formulas overpredict the thrust at low thrust levels and underpredict it at high thrust levels.

It is possible to speculate on many reasons why this might be the case (nonconstancy of the aerodynamic term, interaction terms between applied and self magnetic fields, etc.), but it does not seem worthwhile to pursue this approach further without more detailed experimental measurements. There is ample evidence that mode changes can be introduced by variation of parameters such as engine size, current, or magnetic field. It is entirely possible that less dramatic mode changes can be produced by smaller variations of these parameters. In this case, measurements of internal pressures and current density distributions are necessary to build a more detailed theory.

e. Effects of Ambient Pressure

The possible interaction of the test environment with the MPD thrustor has been a source of concern since operation on entirely entrained mass flow was reported by Ducati,[16] and since a series of experiments indicating entrainment was performed at this laboratory.[17] In an attempt to obtain some insight into the importance of entrainment in the presence of substantial thrustor mass flow rates, a series of measurements has been made on the X-7C-4 thrustor. The measurements were made in the following way: a thrustor mass flow rate and magnetic field strength were set, and a second mass flow rate was bled directly into the test chamber. At one setting of this external mass flow rate, the thrustor current was then varied between 300 and 1000 amperes; and readings of thrust, voltage, anode coolant temperature rise, and test chamber pressure were recorded for thrustor currents of 300, 400, 500, 600, 800, and 1000 amperes. The thrustor current was then returned to 300 amperes, the external mass flow rate was changed to a new setting, and the process was repeated. When the test tank pressure had finally been driven up to about 500 microns, the external mass flow rate was reduced and a new setting of thrustor mass flow rate and/or magnetic field strength was chosen. In this way data were accumulated for thrustor mass flow rates of 23 and 53 milligrams/second, at applied magnetic field strengths of 1.25 and 2.50 kilogauss, for arc currents of 300 to 1000 amperes, and for ambient pressures from about 80 to 400 microns.

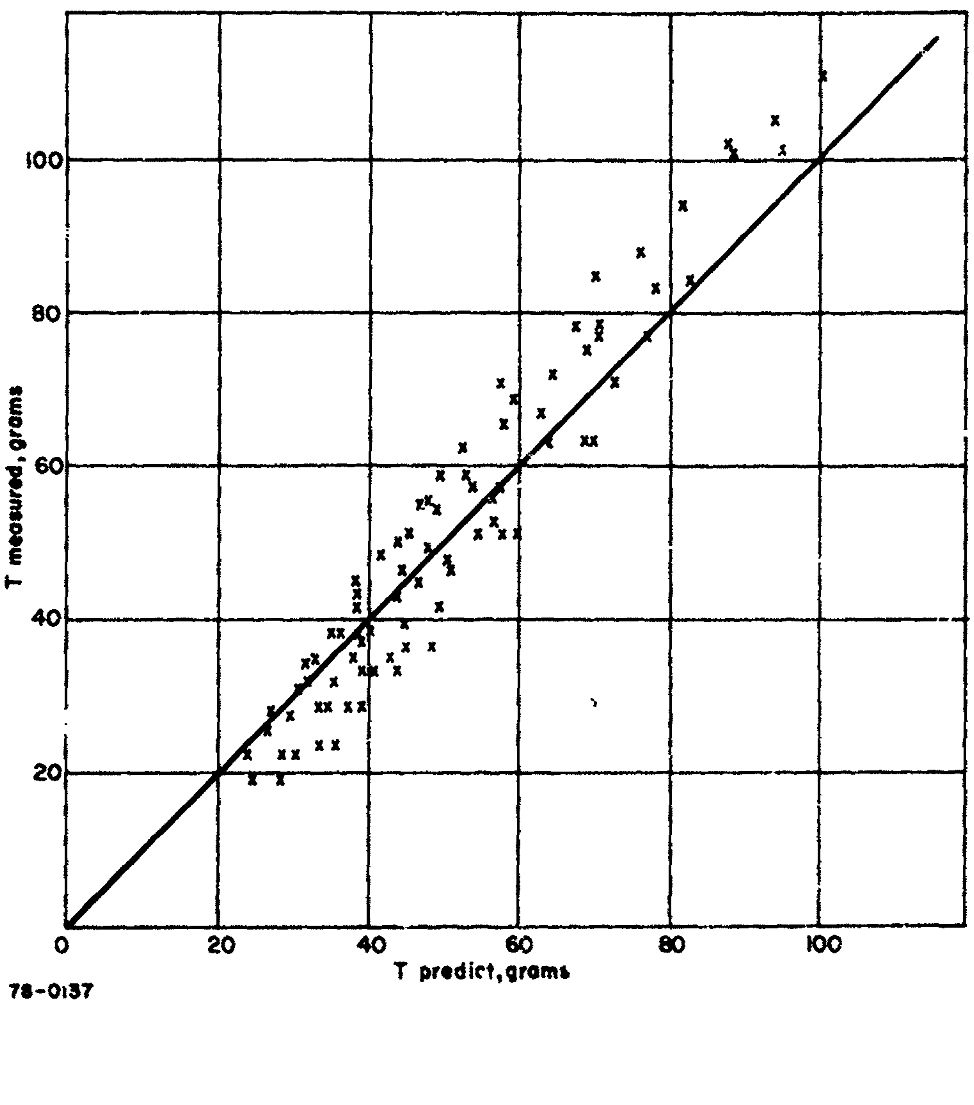

Figure 11 COMPARISON OF MEASURED WITH PREDICTED THRUST, X-7C-4

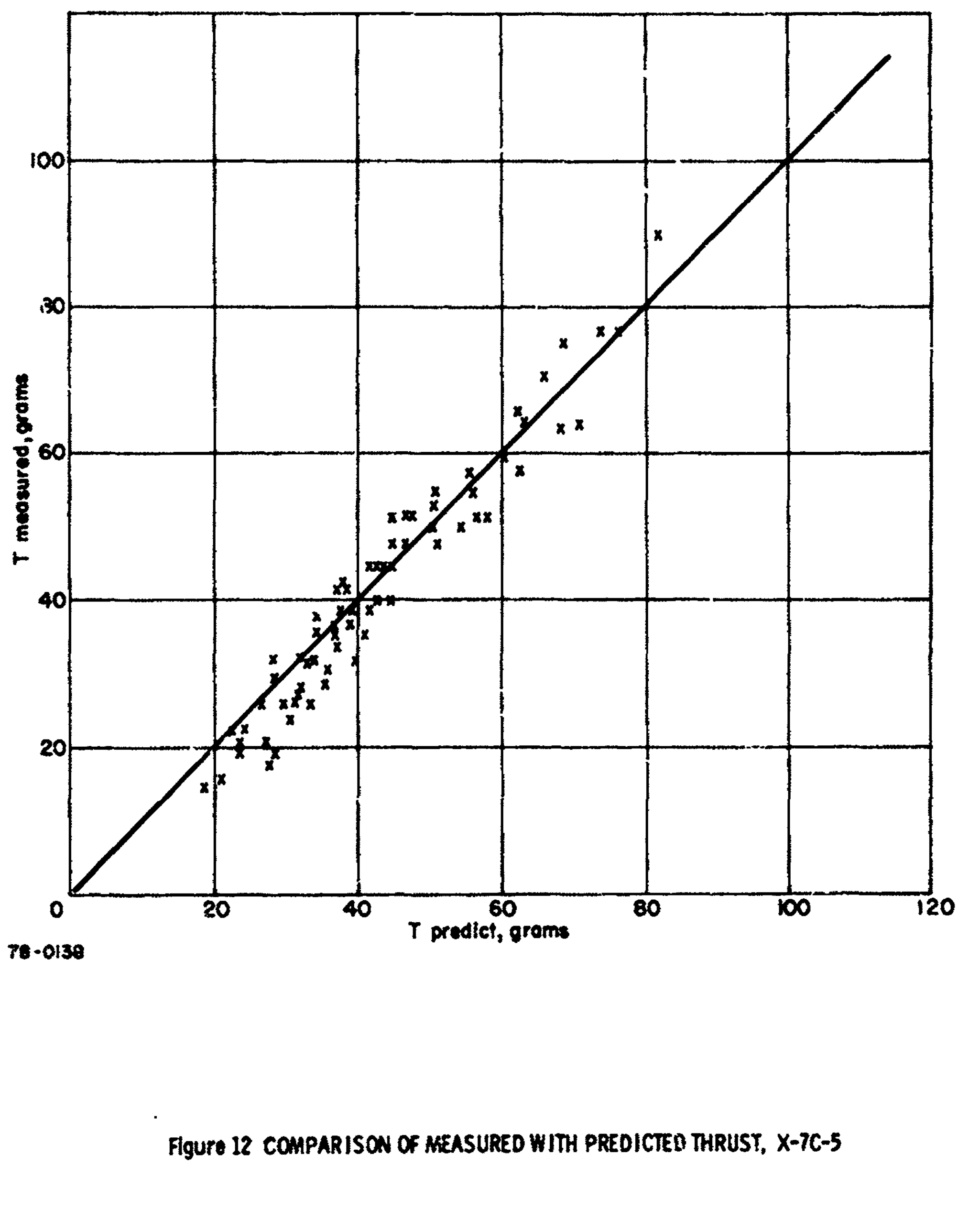

Figure 12 COMPARISON OF MEASURED WITH PREDICTED THRUST, X-7C-5

Figures 13 and 14 plot thrust as a function of measured ambient pressure for three currents, and both values of mass flow and applied magnetic field strength. Figure 13 includes data obtained at a magnetic field strength of 1.25 kilogauss, and Figure 14 includes data obtained at 2.50 kilogauss.

Referring to the figures, there is a general trend of thrust reduction with increasing back pressure over the range in which back pressure was varied. The regularity of the thrust decrease is especially marked at a magnetic field strength of 1.25 kilogauss, with indications at the higher field strength that there are other phenomena which occasionally mask this underlying effect.

We have compared this variation of thrust and back pressure with measurements reported by Jones[18] on an X-2C thrustor operated at the high vacuum facility at NASA Lewis. Figure 15 is plotted on a semi-logarithmic scale, and includes a portion of Jones' data (for $P > 1$ micron) and data taken from the 300 ampere curves at 1.25 kilogauss. Within the limited range of back pressures covered in both experiments, the same trends are observed. It is probably reasonable to conclude that the thrusts as reported here would be increased if a lower ambient pressure could be maintained in the test facility.

Referring to Figure 14, the data for a mass flow rate of 53 milligrams/second exhibit the same trends at the applied magnetic field of 2.50 kilogauss as at 1.25 kilogauss. This is not the case with the data for a mass flow rate of 23 milligrams/second, except at the lowest current. At 600 amperes there is a break in the thrust curve at a pressure of about 150 microns. Above this pressure the thrust is very close to that for 53 milligrams/second, while below it the thrust is much less. At 1000 amperes the thrust is always much less for the smaller mass flow rate, at all pressures tested.

The same tendencies are exhibited by the thrustor voltage. In Figure 16, voltage is plotted as a function of back pressure for a magnetic field strength of 2.5 kilogauss.

At that back pressure where the thrust at 23 milligrams/second shows a sudden change with back pressure, the voltage also exhibits a sudden change. At the same time, the appearance of the exhaust also changes. The central core narrows slightly and increases in brightness, and a second structure, coaxial with this core, horn shaped (opening downstream), and starting at the nozzle face, becomes visible. We have tentatively identified this outer structure with the anode jet, or a return path for electrons which flow downstream in the central core, cross field lines at a downstream location, and return to the anode along field lines. Measurements performed at this laboratory and reported elsewhere[19] indicate that the increase in voltage and the change in exhaust jet appearance are correlated with a higher percentage of the arc current flowing downstream, which supports the visual interpretation of jet appearance.

The sudden variations in voltage have been noted before by Patrick[20] and by Jones,[18] but their production, by varying only the ambient pressure, is thought to be a new observation. It suggests that the switch between high and low voltage is associated with a change in the current distribution and that the change involves the fraction of current which is carried downstream. It has been previously noted that the transition can be brought about by variation of the arc current and/or the applied magnetic field. The fact that it can also be brought about by changes in the ambient pressure is perhaps explainable on the basis that the electrical conductivity of the exhaust gases changes with the ambient pressure, so that, at the higher ambient pressures, current can flow more easily in the exhaust region. The increase in thrust is probably also associated with field-current interactions in the exhaust plume, but entrainment possibilities are enhanced by the extension of the interaction region downstream, and the resulting measured efficiencies are questionable.

Finally, referring to Figure 14, as the current is raised, the thrust obtained at a mass flow of 53 milligrams/second increases more rapidly than at 23 milligrams/second, with the exception of those points where the high voltage mode is evident at the lower mass flow rate. (This mode change was reproducible. Also, compared with Figure 16, it can be seen that the thrust jump was accompanied by a voltage jump, so that the thrust/power ratio varied little as the mode changed.) From Figure 13 this is seen not to be the case at a smaller magnetic field strength (or, at any rate, it is much less pronounced). It is quite likely that the expected difference in aerodynamic (thermal) acceleration can account for the variation of thrust with mass flow rate at the smaller field strength, but it is unlikely that this can explain the differences at the higher field strength. It is possible, although by no means demonstrated, that at the higher mass flow rate the pressure in the exhaust plume is high enough to permit some currents to flow downstream, augmenting the thrust. If this is the case, it would be expected that the thrust for the lower mass flow rate would rise as the ambient pressure is increased. This appears to be the case at a current of 600 amperes, but it is not the case at 1000 amperes at pressures up to 400 microns.

Further implications of this variation in thrust behavior with mass flow rate are discussed in the next section.

f. Efficiency

It is difficult to frame conclusions concerning the efficiency because of the uncertainties introduced by the test environment. The ambient pressure is of the order of 100 microns, and ample evidence exists that engine performance is sensitive to ambient pressure, at least at pressures in excess of 1 micron (and perhaps below). Thus, it is really not known what the true mass flow is, and whether or not the current distribution is representative of the current distribution at low pressure. For this reason, for most of the comparisons made above, the mass flow has been set at 0.036 grams/second so that the back pressure is not a variable. It is anticipated that the trends in voltage, thrust, etc., would be maintained at a lower back pressure, but probably with different absolute values of these quantities. It is believed permissible to treat the efficiency data in the same way; the mass flow rate is fixed, and it is understood that the absolute values of efficiency and I_{sp} may be in error owing to interaction with the test environment.

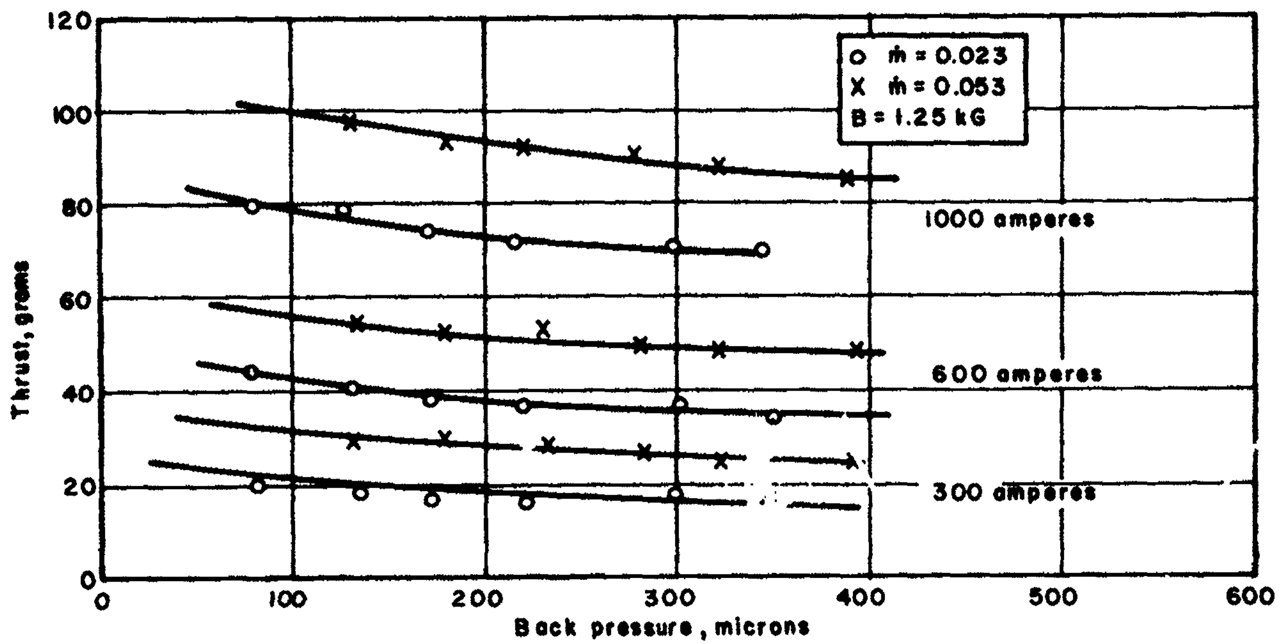

78-0139

Figure 13 THRUST DEPENDENCE ON TEST TANK PRESSURE, B = 1.25 KILOGAUSS

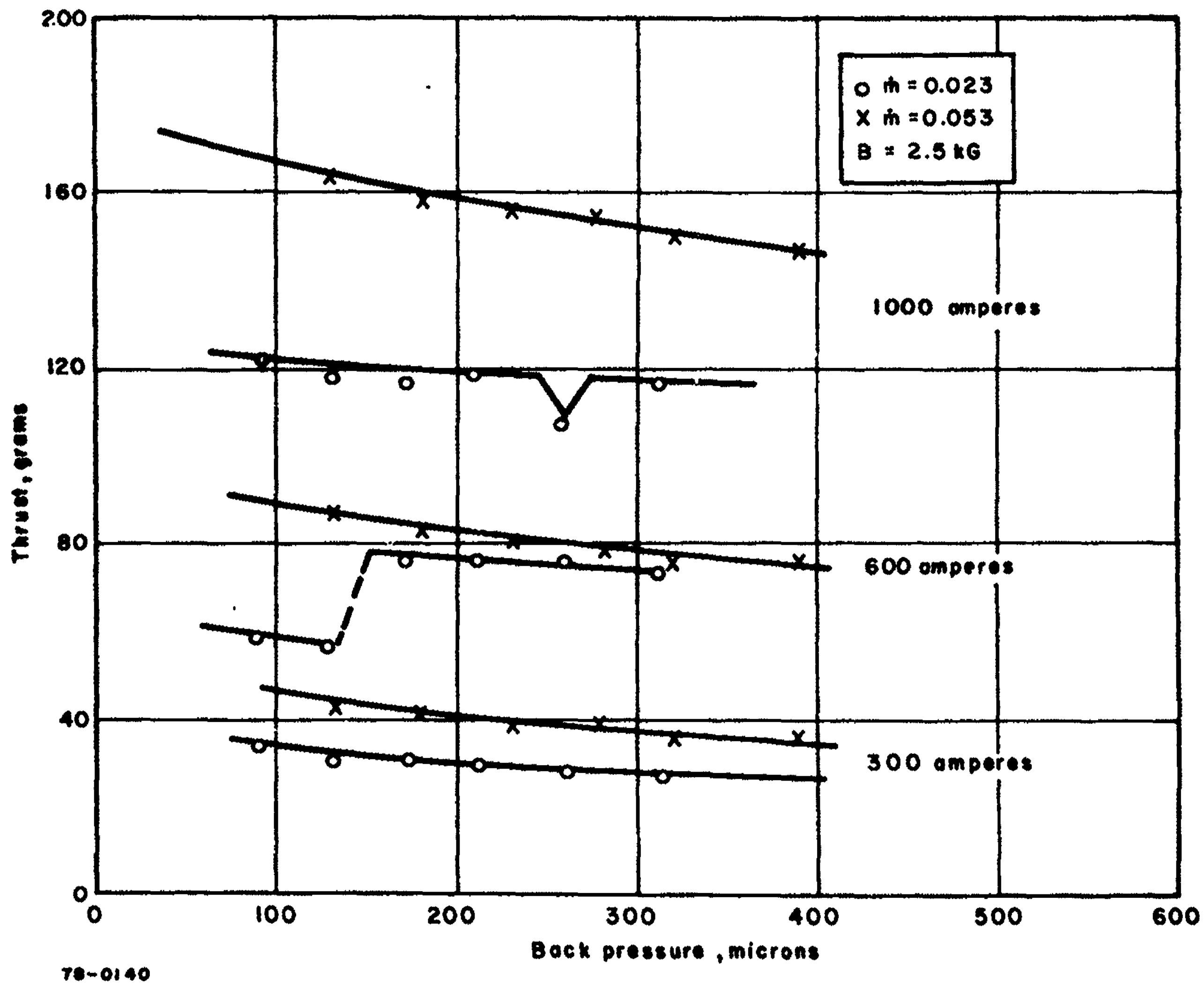

Figure 14 THRUST DEPENDENCE ON TEST TANK PRESSURE, B = 2.50 KILOGAUSS

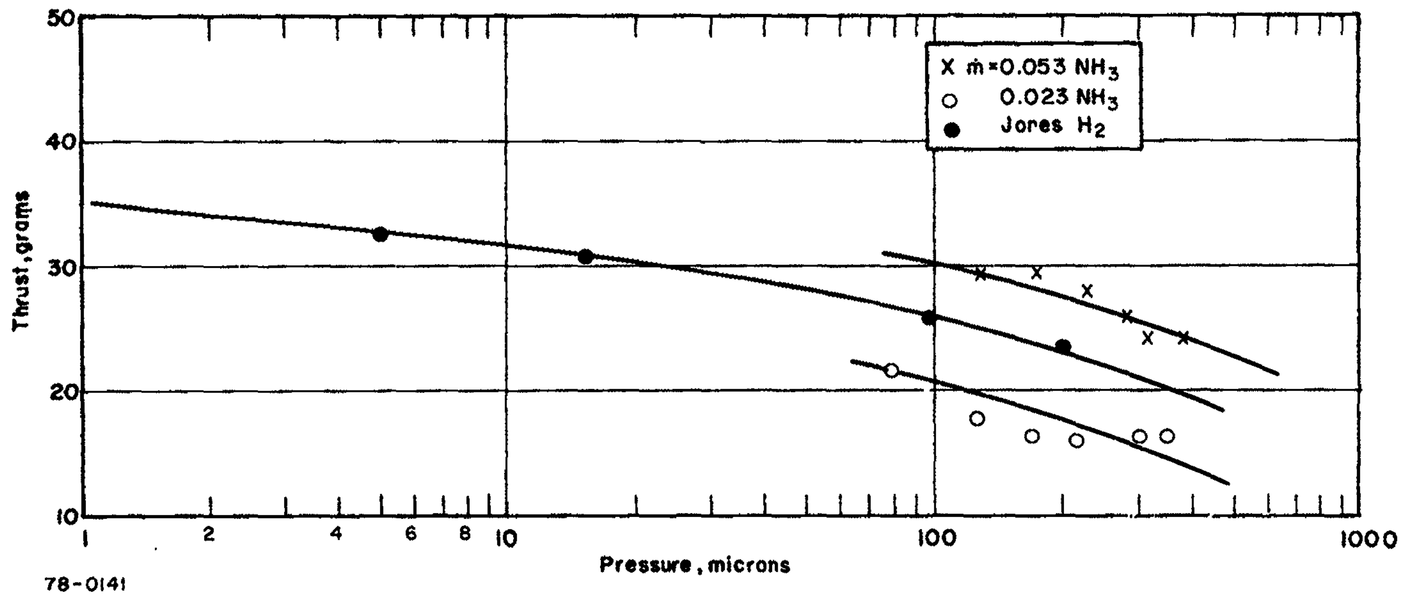

Figure 15 THRUST DEPENDENCE ON TEST TANK PRESSURE, COMPARED WITH DATA OF JONES

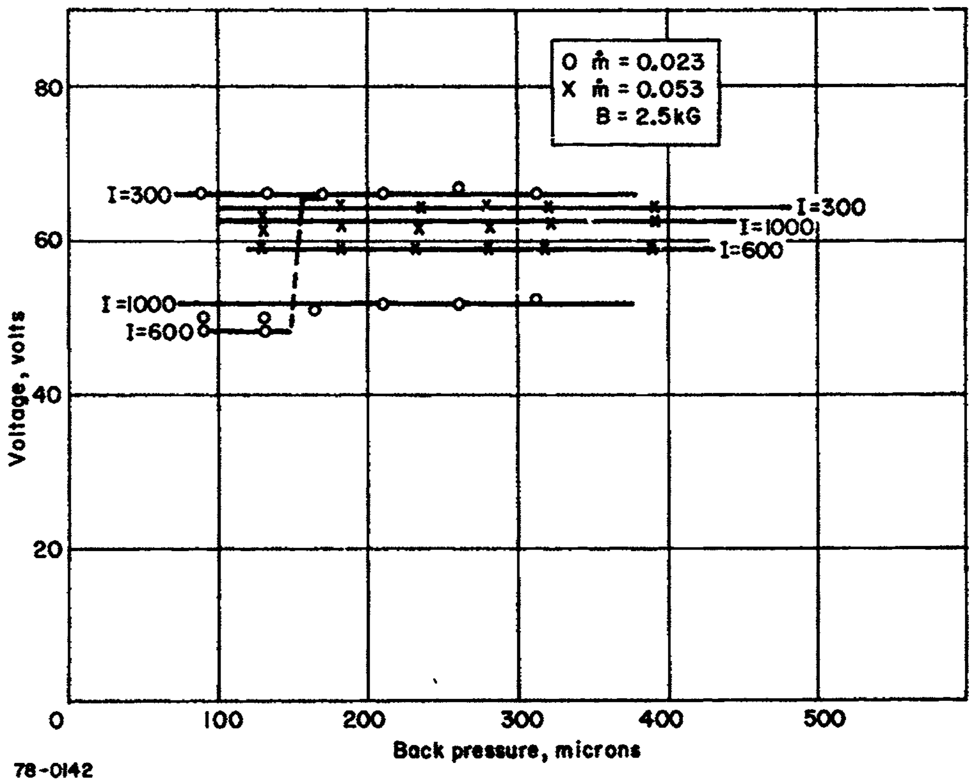

Figure 16 VOLTAGE DEPENDENCE ON TEST TANK PRESSURE

With these provisions, Figure 17 has been prepared, in which efficiency is plotted versus I_{sp} for the three test engines. Several factors are apparent from these data:

1. There are no large differences. The 0.6 inch engine is consistently more efficient than the other two, and it is interesting to note that this engine had consistently the smaller anode fall.

2. Higher I_{sp} values are achieved with the larger engines. The mass flows are fixed and the points plotted are for the same range of I and B. Since the thrust and voltage both increase with engine size, fixing I, B, and $\dot{m}$, and varying engine size has the effect of allowing larger thrusts (hence higher I_{sp}) and larger voltage (hence higher input power) for the larger engines. In principle this could be compensated for by reducing $\dot{m}$ for the smaller engines, but for this comparison we have tried to keep $\dot{m}$ fixed.

g. Effects of Mass Flow Rate

During the parametric variation reported above, it was possible to operate the engines at a wide range of ammonia flow rates. Interesting effects were found which had not been noted earlier in a more restricted range of ammonia flow rates.

Basically, it was observed that over a range of relatively high mass flow rates the engine performance was insensitive to flow rate and in agreement with performance measured earlier for the X-2C engine at flow rates in the same range (0.029 to 0.058 g/sec). However, it was also observed that at flow rates below 0.020 g/sec, the measured performance was not as good as at the higher flow rates.

Drawing on the data of Table IV (d = 0.6 inch), Figures 18 and 19 have been prepared. Figure 18 shows, for B = 2.5 kilogauss, efficiency as a function of specific impulse for ammonia flow rates in the range 4.8 to 68 x 10^{-3} g/sec. Data for the flow rates 36, 53, and 68 x 10^{-3} cluster together and agree with earlier measurements at 29 and 58 x 10^{-3} g/sec on an X-2C engine (d = 0.5 inch). However, for 4.8 to 16 x 10^{-3} g/sec, lower efficiencies are observed.

Figure 19 is similar to Figure 18, but is drawn for B = 0.83 kilogauss. Again, as the mass flow rate reaches low values, the performance falls off substantially.

The effect is an important one, although it should be stressed that, owing to our incomplete understanding of the interaction of the thrustor with the test environment, it may be unrepresentative of what would occur in a hard vacuum. The importance lies in the fact that if, as appears to be the case in our laboratory, there is a minimum mass flow for efficient MPD operation, then there is a minimum power which must be used. For

$$P_{min} = \frac{4.8 \times 10^{-2}\, \dot{m}_{min}\, I_{sp}^2}{\epsilon_o} \tag{8}$$

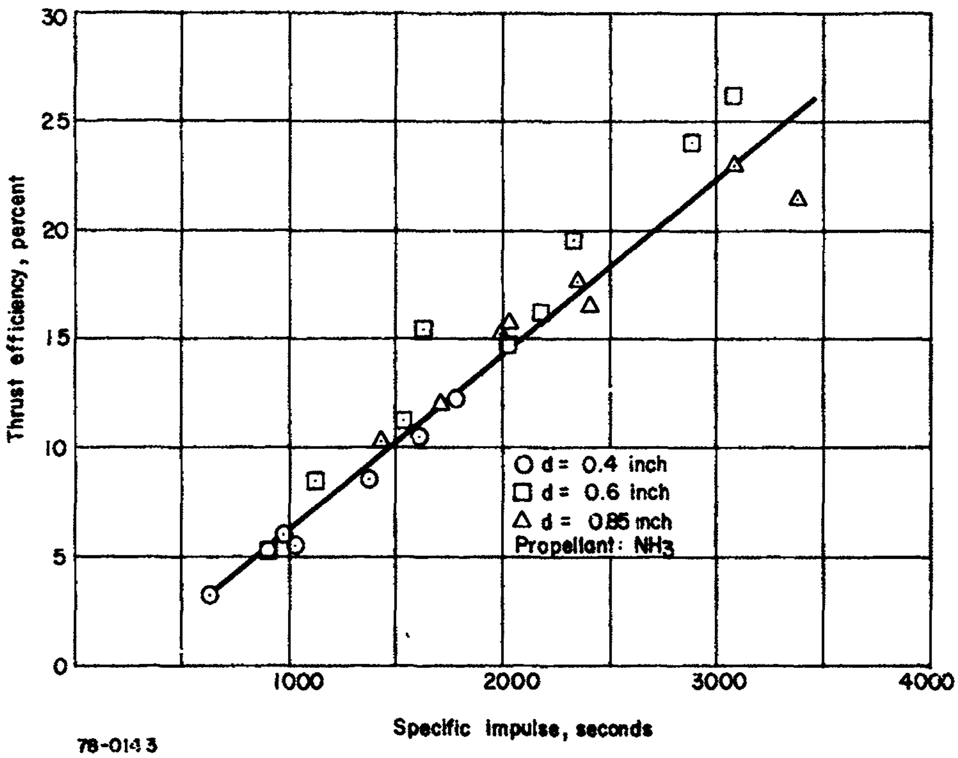

Figure 17 THRUST EFFICIENCY VERSUS SPECIFIC IMPULSE FOR X-7C ENGINES

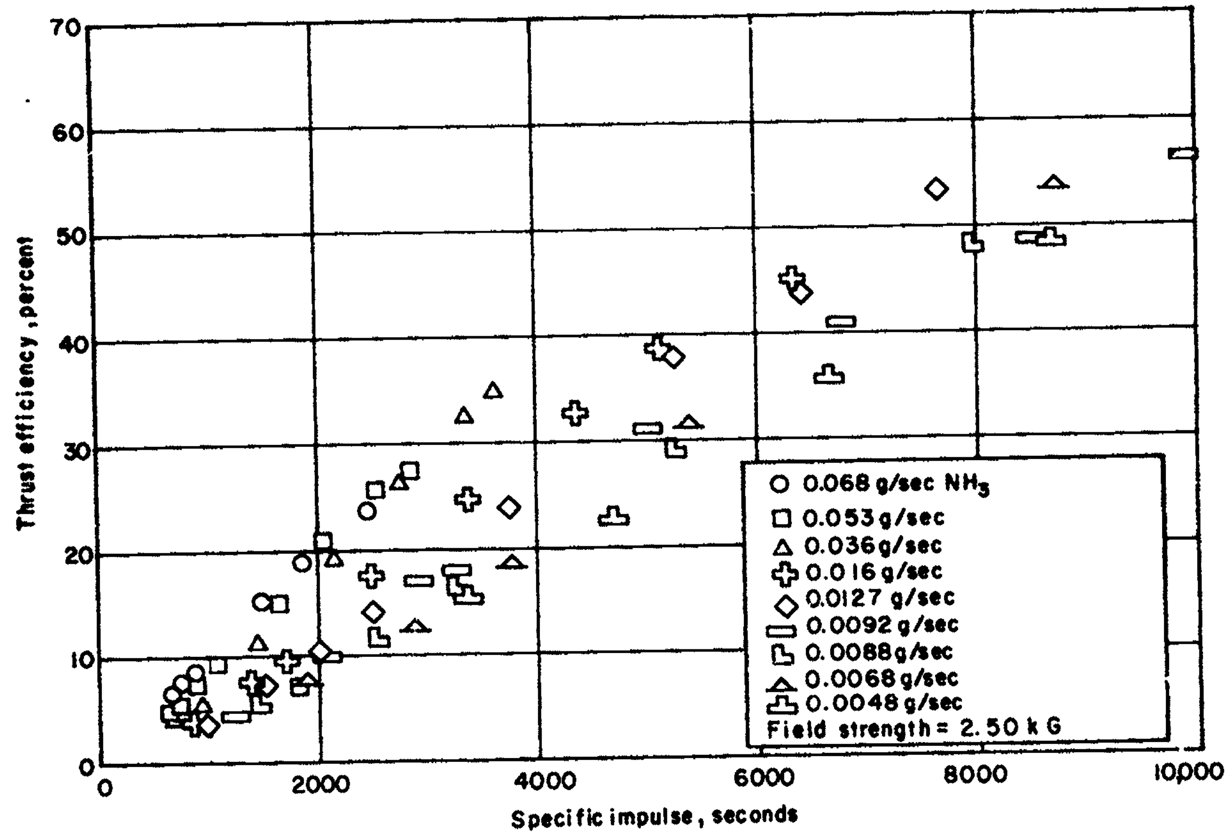

87-917

Figure 18 THRUST EFFICIENCY VERSUS SPECIFIC IMPULSE FOR X-7C-4 ENGINE, B = 2.50 KILOGAUSS

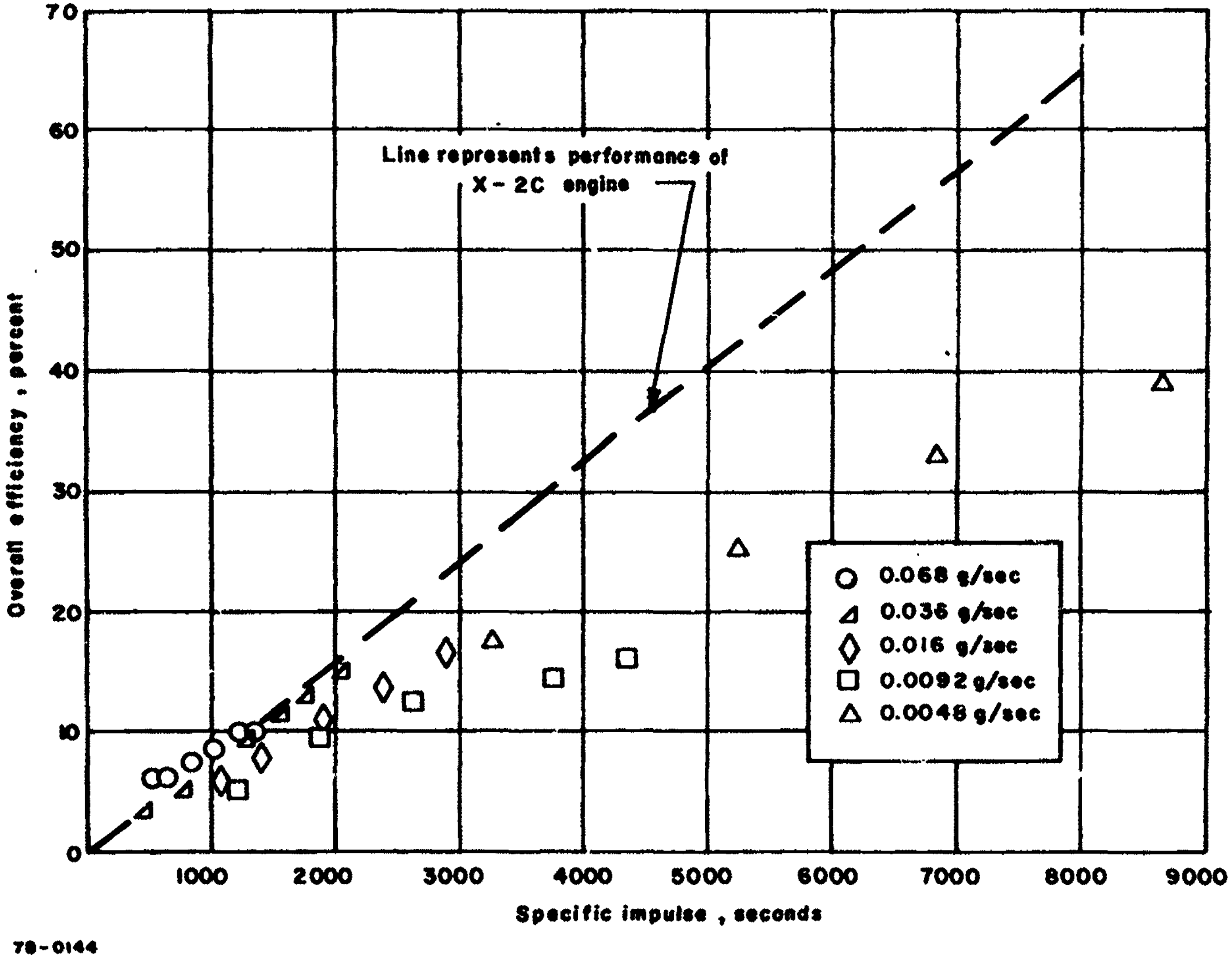

Figure 19 THRUST EFFICIENCY VERSUS SPECIFIC IMPULSE FOR X-7C-4 ENGINE, B - 0.83 KILOGAUSS

P_{min} is the minimum input power in watts and ϵ_o is the overall efficiency. If, for example, the minimum mass flow rate is 20 x 10^{-3} g/sec, and the desired I_{sp} is 4000 sec with a 40 percent overall efficiency, then P_{min} = 38.4 kW. To achieve the same I_{sp} and efficiency at lower power, the mass flow rate must be reduced.

Thus, there is a tendency for performance at low currents and low magnetic fields to be less attractive than that obtained at higher currents and magnetic fields, with the apparent conclusion that low power operation is unattractive. We point out that this is based on the mass flow rate effect, which may be environmentally produced.

The question arises as to the detailed manner in which the performance falls off at lower mass flow rates. That is, for fixed I, B, and engine size, as $\dot{m}$ is reduced, does the thrust fall off more rapidly below $\dot{m}$ = 20 x 10^{-3} g/sec than above, or does the voltage rise more rapidly? In the first case the input power would remain relatively unchanged but the thrust power would not rise with I_{sp} sufficiently rapidly to keep on the efficiency - I_{sp} curve for higher mass flow rates. In the second case the thrust power would rise, but the input power could rise at a great enough rate (with decreasing $\dot{m}$) to reduce efficiency.

Table X displays the behavior of the operating parameters as $\dot{m}$ is reduced at fixed I and B, for the 0.6-inch-diameter throat engine (X-7C-4).

TABLE X

VARIATION OF MASS FLOW RATE FOR X-7C-4 ENGINE
d = 0.6 INCH, I = 1000 amperes, B = 1.66 kilogauss

$\dot{m}$ g/sec	V volts	P_{in} kW	T grams	I_{sp} sec	ϵ_o percent
0.068	52	52	94.0	1,380	12.0
0.053	51	51	88.0	1,650	13.7
0.036	50	50	78.3	2,170	16.3
0.016	42	42	51.2	3,200	19.7
0.0127	53	53	67.1	5,280	32.1
0.0092	60	60	70.3	7,640	43.0
0.0088	58	58	68.7	7,800	43.3
0.0068*	50	50	70.3	10,300	70.0
0.0048*	64	64	78.2	16,200	95.5

* $\epsilon_o > \epsilon_t$, definitely indicating entrainment.

From Table X, for mass flows of 0.068 to 0.036 g/sec, the thrust falls slightly with mass flow decrease, and the input power is nearly constant. For mass flows of 0.0127 g/sec and below, the thrust and input power vary erratically with mass flow rate and show no marked trends, suggesting that the true mass flow rate is perhaps not being varied. At 0.016 g/sec both the thrust and voltage are minimum.

While it is dangerous to draw conclusions from data on imperfectly understood interactions, it is possible to hypothesize that at high mass flows the interaction with the environment is negligible, at low mass flows this interaction dominates completely, and in the range 0.010 to 0.020 g/sec both the input mass flow and the environment contribute to the measured performance. If this is true, then it is likely that the qualifying terms "low," "high," and "intermediate" take on different meanings depending upon the environment. Thus, we have attempted to draw conclusions from our data based on a flow rate of 0.036 g/sec, which seems a reasonable compromise between avoiding interaction with the environment and not requiring excessively high input powers. In a lower ambient pressure facility the "safe" mass flow may be substantially lower, permitting valid operation at much lower input power levels.

h. Propellant Composition

A series of experiments were performed with an X-7C-1 thrustor to examine the influence of ammonia dissociation upon thrustor performance. Specifically, two series of measurements were made. In the first series the procedure was essentially identical to that followed in the other experiments reported above. In the second series the ammonia propellant was replaced by a mixture of 14 parts nitrogen and 3 parts hydrogen (by weight). A large plenum was used to assure good mixing. The results are tabulated in Table XI below.

The principal result of these measurements has been to indicate that the differences between operation with ammonia and with the equivalent mixture of nitrogen and hydrogen are small and nonsystematic. That is, if operation with ammonia is taken as a baseline, then the values of thrust and voltage in operation with the nitrogen-hydrogen mixtures do not depart substantially from the baseline, and tend to scatter around the baseline rather than to be always above or below. Indeed, the quantity T/IV tends to the same average values for operation with either propellant.

At some operating conditions the thrustor has been in the high voltage mode for ammonia and the low voltage mode for the nitrogen-hydrogen mixture, and at other conditions the reverse is true. In these cases there are significant differences in the thrust and voltage, but these appear to be related more to the voltage mode than to the propellant type. There is no systematic variation of voltage mode with propellant (e.g., it is not the case that either propellant yields one mode preferentially), and even where the modes are different, the quantity T/IV tends to remain the same.

It is reasonable to conclude from this that ammonia is dissociated in the discharge. Since the thruster is water-cooled it is unlikely that there is appreciable dissociation resulting from contact between the gas and the thrustor body. At the same time the fact that there are no

TABLE XI

AMMONIA AND NITROGEN-HYDROGEN

amperes I	kG B	g/sec $\dot{m}_{NH_3}$	volts V	grams T	kW Power to Cooling	sec I_{sp}	g/sec $\dot{m}_{N_2,3H_2}$	volts V	grams T	kW Power to Cooling	sec I_{sp}
300	1.25	0.053	62	33.3	8.1	630	0.053	61	29.8	7.7	560
400			62	49.8	10.7	940		61	43.2	9.6	810
500			62.5	63.1	14.2	1190		60	51.4	11.5	970
600			62.5	74.8	16.2	1410		58	61.3	14.1	1160
800			62	98.0	20.9	1850		57	84.6	18.0	1600
1000			59	116.	26.2	2190		58	107.	23.5	2020
300	2.5	0.053	86	48.1	9.4	910	0.053	85	43.1	10.8	810
400			86	68.	12.2	1280		86	60.6	13.7	1140
500			85	91.2	15.0	1720		86	79.7	16.8	1500
600			80	101.	17.6	1910		86	102.	20.4	1920
800			73	126.	23.0	2380		90	140.	25.4	2640
1000			70	162.	29.8	3060					
300	1.25	0.036	65	25.6	8.6	710	0.036	61	31.4	8.2	875
400			65	39.0	10.9	1080		61	43.2	10.7	1200
500			65	53.1	13.8	1475		61	51.4	12.9	1430
600			65	64.7	15.7	1800		61	59.8	14.8	1670
800			60	86.4	20.2	2400		57	79.7	19.4	2220
1000			55	99.6	24.4	2770		55	99.3	21.8	2770
300	2.50	0.036	89	45.8	10.8	1270	0.036	86	43.2	12.0	1200
400			89	67.	14.4	1860		86	59.8	15.3	1660
500			90	88.2	18.0	2450		87	79.7	18.5	2220
600			92	111.	22.6	3080		75	38.0	20.8	2450
800			95	150.	26.9	4170		76	122.	27.3	3400
1000			70	119.	25.9	3310		70	139.	33.6	3870

systematic differences in operation with ammonia or the nitrogen-hydrogen mixture suggests that the ammonia does become dissociated. It should also be noted that qualitative spectroscopic observations on the MPD exhaust, at NASA Lewis, confirm the dissociation of ammonia.

The importance of this observation is that it is thus unlikely that the relative performance of water- and radiation-cooled thrustors would be affected by differences in propellant dissociation. Even if, in a radiation-cooled thrustor, the propellant is dissociated by contact with hot walls before it enters the discharge, it is unlikely that this will have any significant effect upon performance.

B. PERFORMANCE OF RADIATION-COOLED ENGINES

1. Comparison of Radiation- and Water-Cooled Engines

A radiation-cooled engine which shows considerable merit has been designated X-7C-R, as shown in Figures 20, 21 and 22.

The tungsten anode and cathode are self-cooling, and boron nitride insulators are used for interior insulation. On this model, the outside diameter was 4 inches and the throat diameter 0.8 inch. A water-cooled counterpart (X-7C-1) was tested separately to evaluate the effects of cooling mode.

On the basis of tests made on these engines, it has been concluded that there is no significant different in thrust performance due to the cooling mode. To illustrate this point, Figure 23 compares directly the efficiency versus I_{sp} for two engine configurations (one water-cooled and one radiation-cooled), both constructed with a 4-inch outside diameter and a 0.8-inch throat.

However, there is an apparent difference in operating parameters between the two engines, a difference which is not yet understood. At fixed I, B, and $\dot{m}$, there is a significant difference in voltage (V) and thrust, of such a nature that the ratio T/V is not greatly affected; thus, the efficiency versus I_{sp} curve is not much changed although the detailed operating points are.

Examining Table XII, it is clear that in general the water-cooled X-7C-1 ran at a higher voltage than did the radiation-cooled X-7C-R and, under some conditions, at a higher thrust. Indeed, the effect is as though the characteristic dimension of the X-7C-R is smaller than that of the water-cooled version. For comparison, we have included also in Table XII the data for the X-7C-4 engine with 0.6-inch throat. It can be seen that the voltage and, usually, the thrust for the X-7C-R thrustor are bracketed by the values for the X-7C-1 and X-7C-4 thrustors.

In summary, it appears that there are differences in operating point between radiation- and water-cooled engines, but no outstanding differences in overall propulsion performance. At low values of B the X-7C-R behaved like the X-7C-4 (0.6-inch throat) and at high values of B like the X-7C-1 (0.85-inch throat).

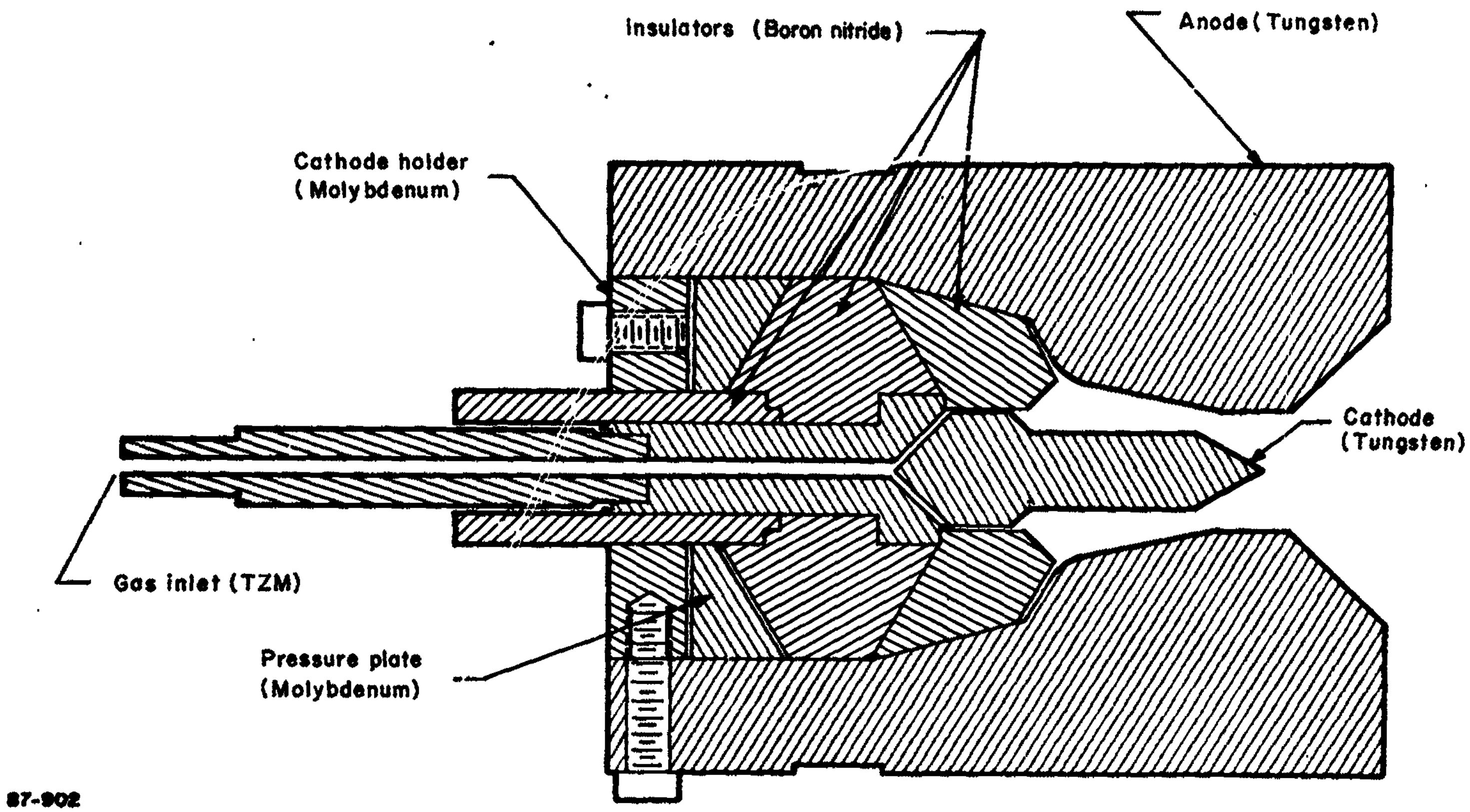

Figure 20 SCHEMATIC DRAWING OF X-7CR MPD RADIATION-COOLED THRUSTOR

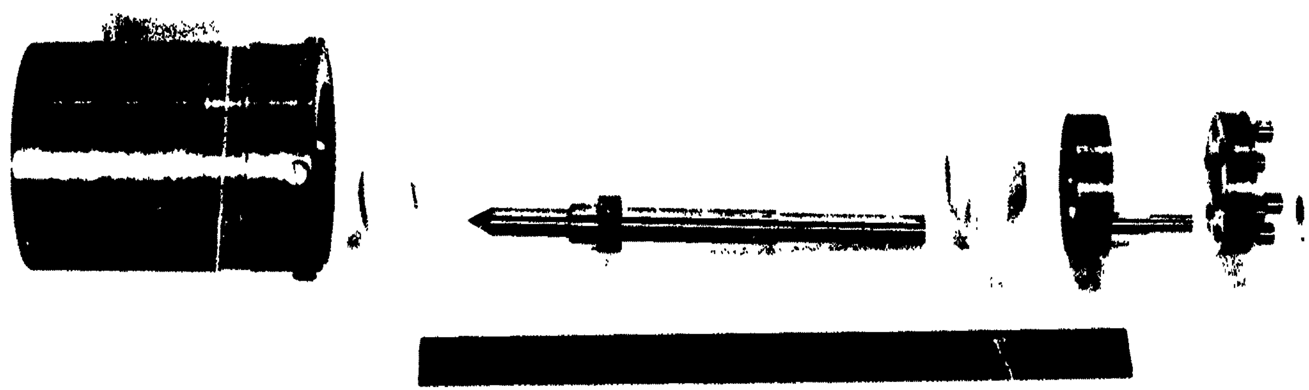

14999B

Figure 21 PHOTOGRAPH OF X-7CR MPD THRUSTOR DISASSEMBLED

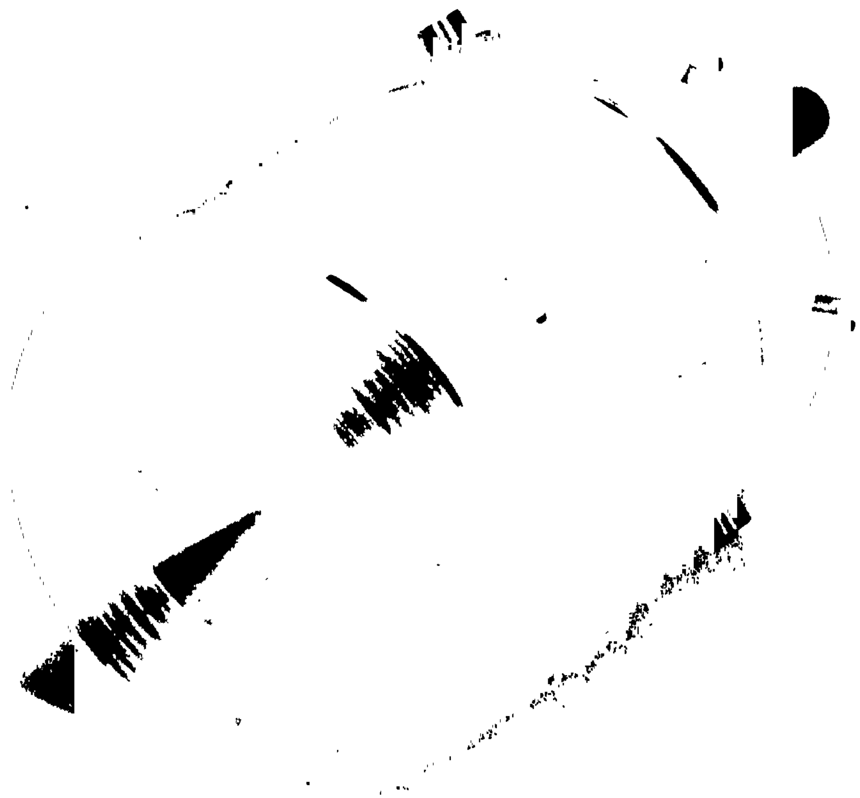

14999 A

Figure 22 X-7CR MPD THRUSTOR ASSEMBLED

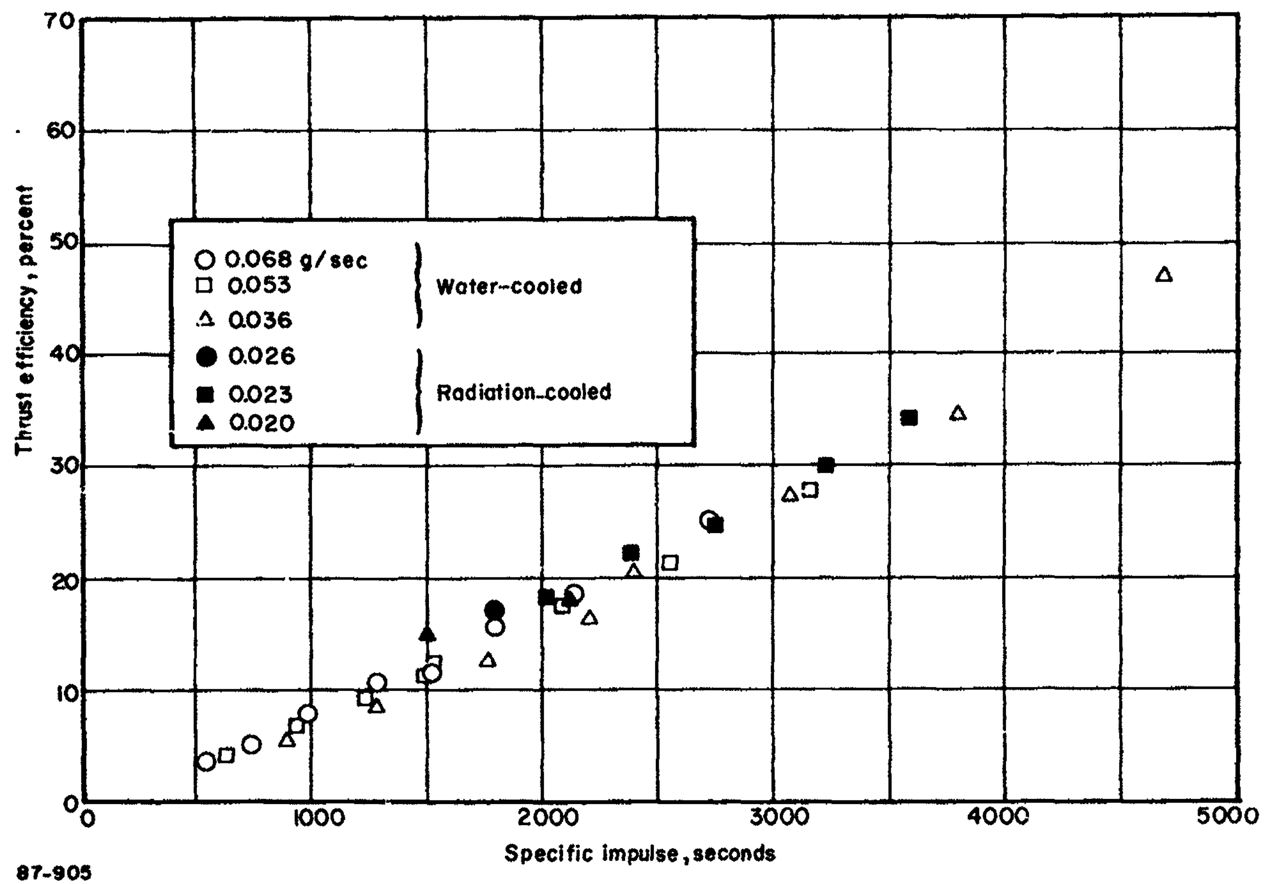

Figure 23 COMPARISON OF MEASURED EFFICIENCY OF 4-INCH-DIAMETER WATER-COOLED AND RADIATION-COOLED MPD THRUSTOR

TABLE XII

COMPARISON OF RADIATION-COOLED X-7CR AND
WATER-COOLED X-7C-1

I	$\dot{m}$	B	Voltage			Thrust		
			X-7C-R	X-7C-1	X-7C-4	X-7C-R	X-7C-1	X-7C-4
400	0.036	0.88	42	60	42	19.9	33.5	22.4
		1.25	50	57	46	28.6	31.9	22.3
		1.66	57	66	50	41.5	36.7	23.5
		2.08	76	75	52	44.7	39.3	41.5
		2.50	69	85	53	46.5	46.3	25.5
500		0.88	39	57	40	26.5	39.9	27.6
		1.25	50	54	44	39.8	38.3	28.7
		1.66	57	66	50	52.7	49.5	33.5
		2.08	64	76	50	54.2	55.8	51
		2.50	65	85	51	56.5	63.9	33.5
600		0.88	38	57	39	33.2	51.1	31.1
		1.25	49	52	43	51.1	43.2	35.1
		1.66	51	69	50	54.3	60.7	39.9
		2.08	57	76	50	63.8	72	59
		2.50	60	86.5	51	70	79.8	51.1

2. Effect of Scale-Down

A scaled-down version of the X-7C-R radiation-cooled engine was made to evaluate performance of a lighter version of the radiation-cooled design. A 3-inch-diameter MPD arcjet was tested over a range of mass flow, magnetic field strength, and currents to define the performance. Results of these tests are presented in Figures 24 and 25.

The overall efficiency and specific impulse compare in essence with previous data on a water-cooled version. However, the maximum attainable current and the minimum mass flow were more limited due to higher engine temperatures. At comparable conditions, the engine temperature was generally 200 to 300°C higher than on the larger 4-inch-diameter engine. The maximum specific impulse achieved with this engine is below the range of immediate interest.

The 3-inch engine was fabricated from a tungsten billet which was apparently defective, as evidenced by the development of a crack on the cathode end of the engine prior to test. This defect became worse during test and power cycling. Three different runs developed two other cracks through the throat of the engine. The condition of interior parts, insulation and cathode, was found to be generally good after test.

The problem of fractures developing on the anode, on both the 4-inch-diameter as well as the 3-inch-diameter engines during thermal cycling, suggests either an extension beyond the ultimate tensile strength of the tungsten or the development of a crystalline structure which degrades the tensile properties. The material used for the anode is sintered tungsten with a few percent thoria doping. No indication of recrystallization, which would lead to the development of failures in the tungsten, has been found.

It has been demonstrated on a previous program[21] that radiation-cooled thrustors can handle power levels of at least 30 kW for periods of at least 700 hours with proper design for cooling. On that program higher engine temperatures were reached without anode failures, though with smaller diameter engines. The larger dimension of the present engines may introduce a limitation by the internal stresses developed.

a. Operating Voltage

The voltage current characteristic of the 3-inch radiation-cooled engine parallels the performance of the water-cooled version as shown in Figure 25, but displays about a 10-volt decrement which is presently unexplained. The cathode employed on this test was barium-calcium-aluminate impregnated tungsten rather than the usual thoriated tungsten used on other tests. A combination of this fact and the hot anode may produce the observed voltage change.

b. Operating Temperature

The external surface temperature of the radiating engine was determined from readings with an optical pyrometer which were corrected for the tungsten emissivity and window absorption. The temperatures for the

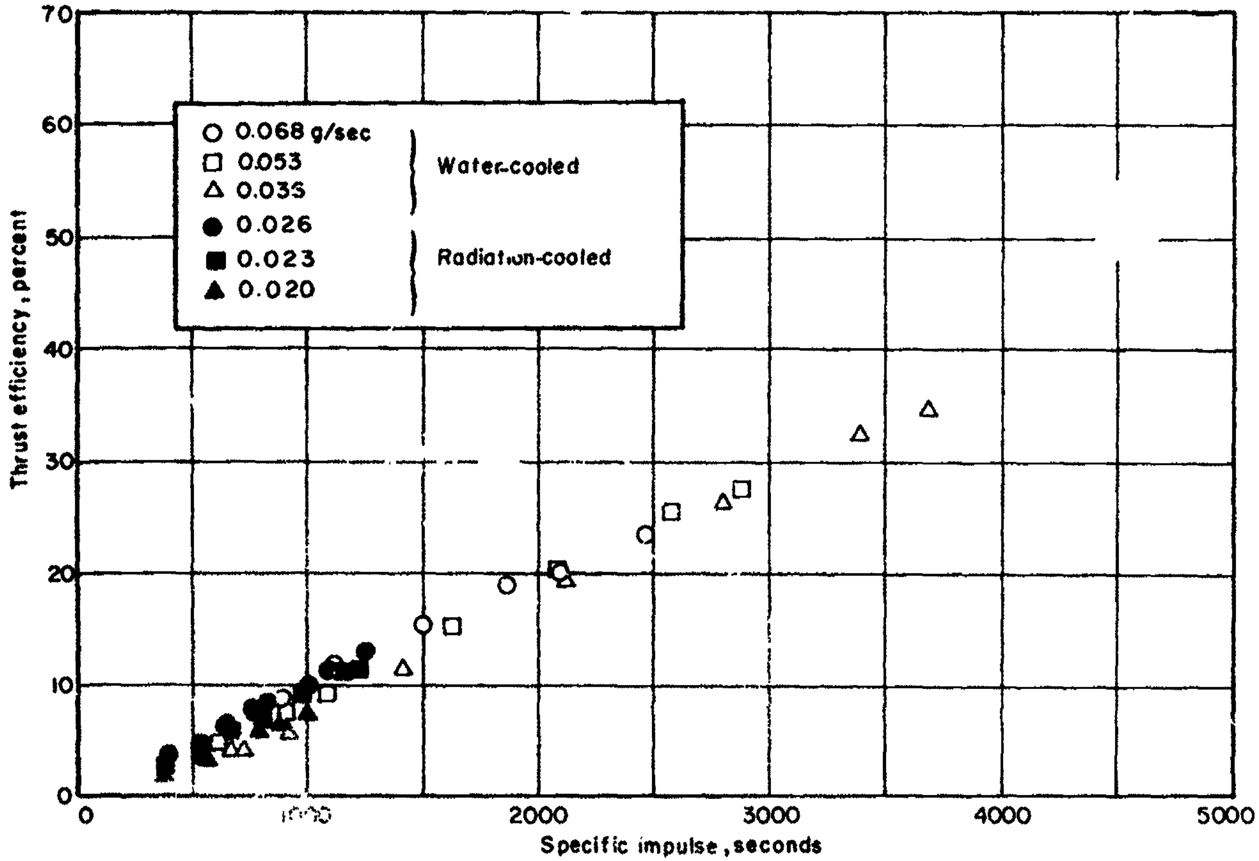

87-906

Figure 24 COMPARISON OF MEASURED EFFICIENCY OF 3-INCH-DIAMETER WATER-COOLED AND RADIATION-COOLED MPD THRUSTOR

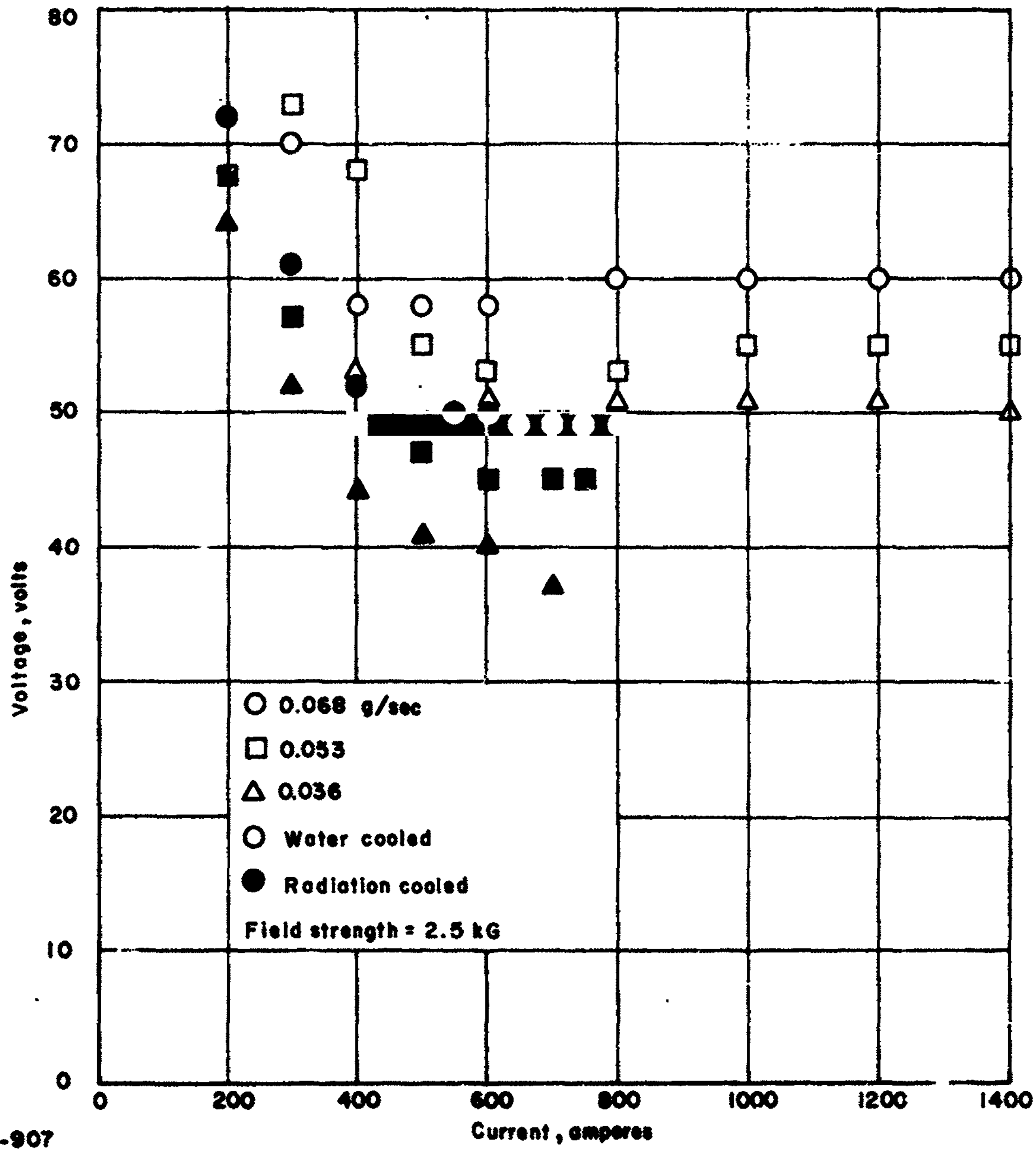

87-907

Figure 25 ARC VOLTAGE VERSUS CURRENT FOR THE 3-INCH-DIAMETER WATER-COOLED AND RADIATION-COOLED THRUSTOR

3- and 4-inch-diameter thrustors are plotted in Figure 26 versus arc power. While some hysteresis is noted in the increasing power values over those for decreasing power, the data generally follow the fourth power relation shown as expected. At lower mass flow values, a rise in temperature occurs.

c. Low-Power Engine Tests

A series of tests were conducted on the L-2 model engine which had primarily been utilized for alkali metal propellant tests. The engine had a 2-inch outside diameter and a 0.5-inch throat. A photo of the arcjet assembly and mounting bracket is shown in Figure 27. The construction details of the engine are given in Figure 28. It comprises a tungsten exhaust nozzle fitted and molybdenum-vanadium (2150°C) brazed to a molybdenum section which is held by the mounting bracket, as seen in Figure 27. The thoriated tungsten cathode and boron-nitride insulators extend beyond the water-cooled bracket and incorporate metallic C-ring seals.

This engine was installed on a thrust balance and mounted within an aluminum test tank. The magnetic field was produced by a water-cooled solenoid coil, and a water-cooled shield ring was mounted inside the coil so as to enclose the engine. The magnetic field had a maximum value of 2 kilogauss. Since this engine is a relatively low-power design, all tests were made at this peak value of magnetic field to keep the voltage high and, correspondingly, to reduce the engine current at a given power level. Data were obtained at various mass flow conditions at increasingly high current levels. The procedure followed in the tests was one of progressively raising the power on the engine until ultimately some indication of failure in the cathode-anode region was evident.

Tests of the engine were halted after erosion was observed when the power was increased to about 14 kW. However, the damage to the engine was found to be relatively superficial, occurring for the most part as a fracturing at the forward edge of the boron-nitride insulator separating the cathode and anode. This effect did not recur on the second test, when the changes in power were more gradual.

The performance of the engine was low, providing about 1800 seconds specific impulse at 10 percent overall efficiency for the lowest ammonia flow rate utilized. The overall thrust efficiency variation with the specific impulse is shown in Figure 29. The efficiencies are generally below 10 percent and show a lower trend with decreasing propellant mass flow at any given specific impulse. The results were generally lower than the best data on water-cooled MPD arcjets.

The integrity of the engine, while not extensively tested for endurance, seemed satisfactory below the maximum power input attained of 22.5 kW. During the tests a large temperature gradient was evident across the brazed joint separating the tungsten and molybdenum sections. The condition which limited further testing was local melting of molybdenum directly behind the tungsten throat. Some melting and attrition of the cathode and the C-rings was also found.

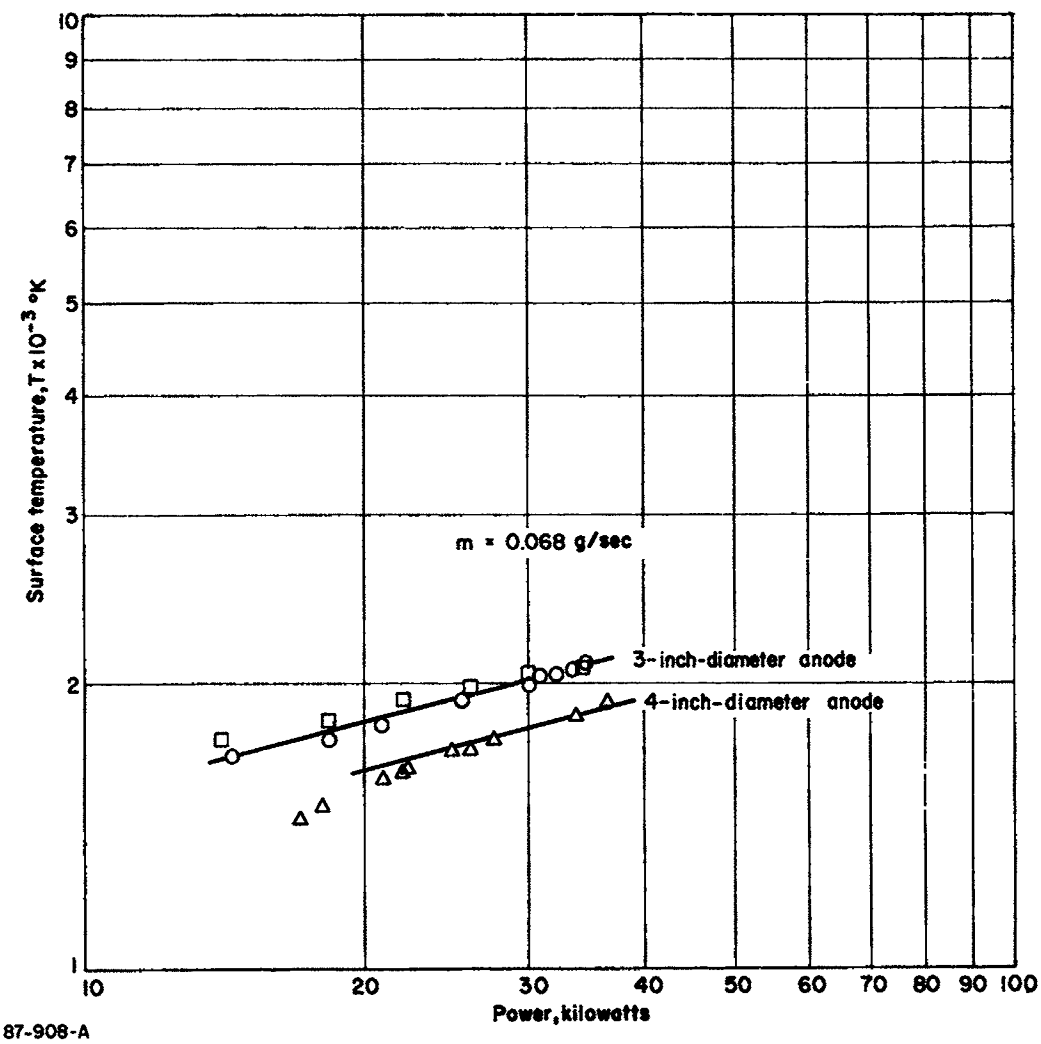

87-908-A

Figure 26 MEASURED SURFACE TEMPERATURE VERSUS POWER FOR RADIATION-COOLED THRUSTORS

87-909

Figure 27 PHOTOGRAPH OF RADIATION-COOLED ALKALI METAL MPD
ARCJET MODEL L-2

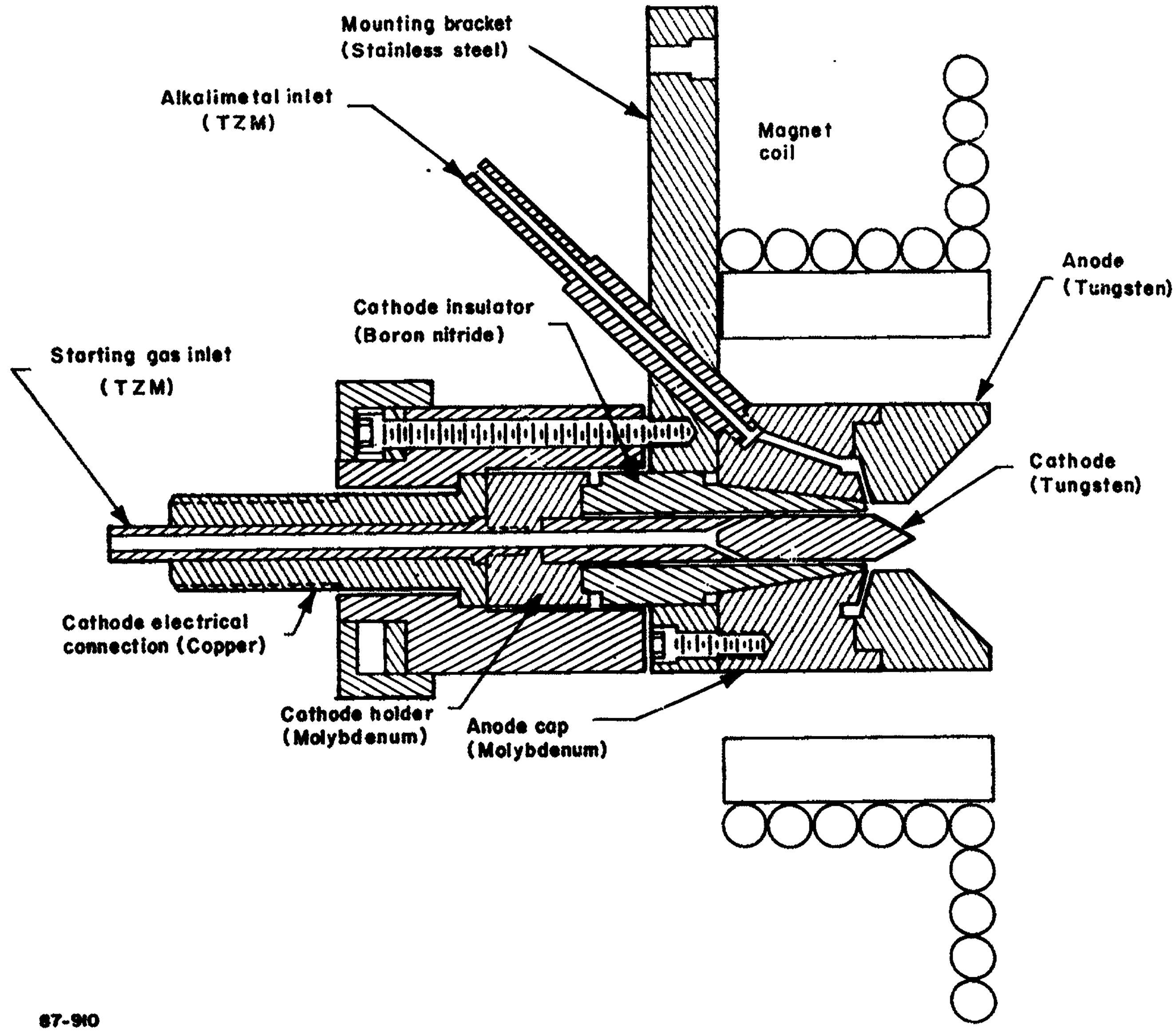

87-910

Figure 28 SCHEMATIC OF RADIATION-COOLED ALKALI METAL MPD ARCJET MODEL L-2

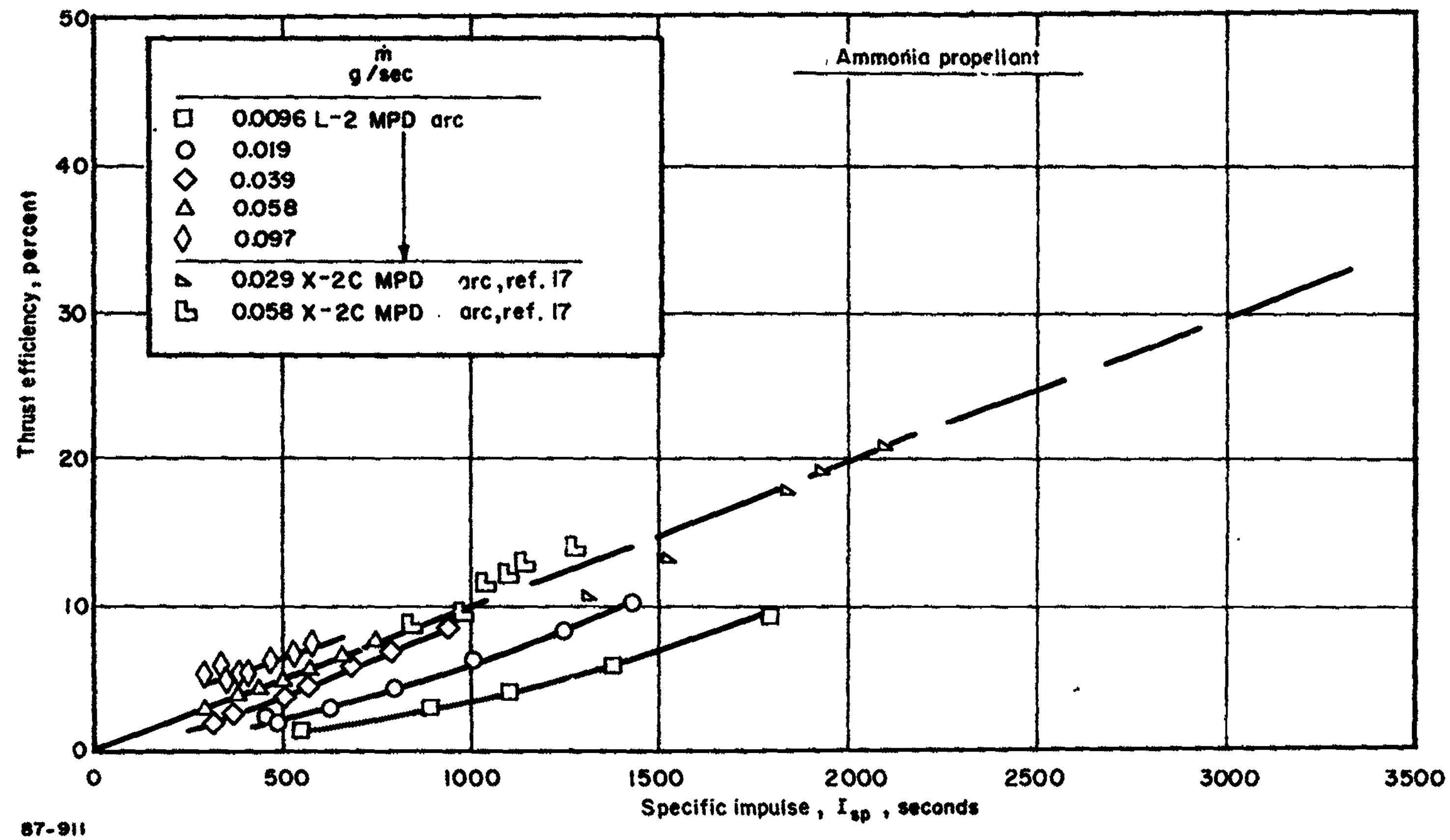

Figure 29 THRUST EFFICIENCY VERSUS SPECIFIC IMPULSE FOR THE MODEL L-2 THRUSTOR

d. Power Capability

The radiation engines which have been tested establish some bound to the maximum power input which can be achieved without material loss. The performance of the three radiation engines which have been tested define a size to maximum power behavior as shown in Figure 30. If the conduction process from the internal to external surface is considered bound by the onset of melting, then the maximum power will be approximately dependent on the scale dimension as observed.

C. ENGINE LIFE DEMONSTRATION

An endurance test on a radiation-cooled version of the MPD acjet was made using a 4-inch-diameter X-7CR engine (Figure 20) with ammonia propellant. The test involved only one power cycle from startup to shutdown. Initially, operation was conducted at progressively higher power values in steps of 100 amperes from 200 to the duration test value of 900 amperes. Operation at 1000 amperes was attempted but produced some material erosion. The endurance test was begun at a power level of 36 kW, specific impulse of 3600 seconds, and overall thrust efficiency of 34 percent. A mass flow of 0.023 g/sec and a magnetic field strength of 2.5 kilogauss were utilized. The background exhaust pressure was about 90 microns.

The maximum external engine temperature for the radiation engine was approximately 2000°K, shown operating in Figure 31.

The test was conducted for 75 hours (uninterrupted) at the power and mass flow condition set. However, certain malfunctions of support equipment occurred which affected the test results. Loss of the transducer signal, due to an overheated cable, after a few hours operation, did not allow a continuous monitoring of thrust. However, a more serious condition developed when an observation window developed a crack which could not be sealed efficiently. As a result, the background environment became air-contaminated to a extent which caused slow oxidation of the radiating engine parts, particularly the high-temperature nozzle end of the engine. This condition had not been observed on any previous tests on this program with a controlled background. In fact, former experience with tungsten body radiation cooled arcjet thrustors[21] which operated at higher temperatures and for prolonged periods of up to 30 days, did not display oxidation.

In spite of the short comings of the test, the 4-inch-diameter radiation engine shows considerable promise. The anode block did not exhibit any thermal structural cracks as had occurred on other tests at lower current levels with cycling. The power, specific impulse, and overall thrust efficiency values which had been achieved offer reasonable propulsion conditions. The operation of the engine at the stated conditions in an improved vacuum, where increased thrust has been demonstrated,[18] would project the performance close to the 5000-second, 50-percent overall efficiency figure.

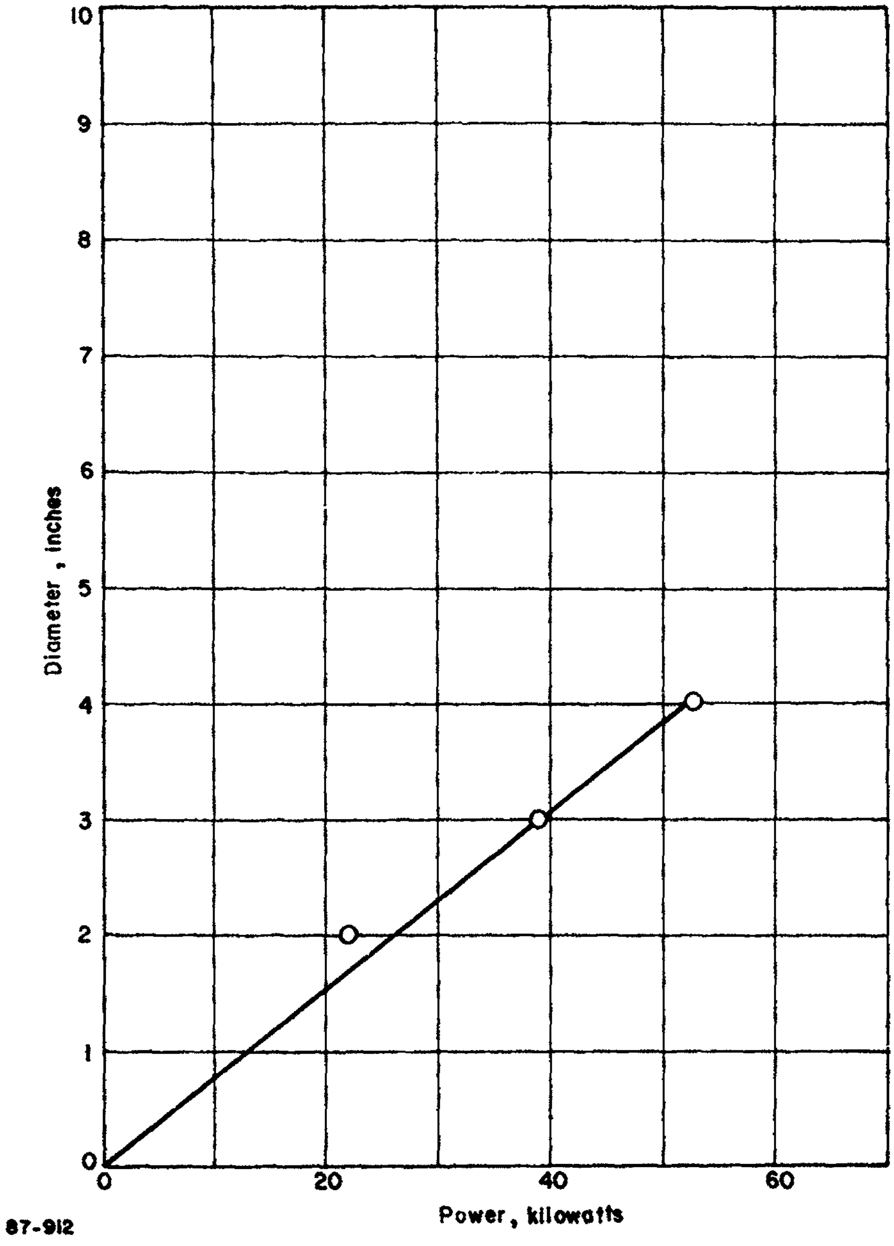

Figure 30 ANODE DIAMETER VERSUS MAXIMUM POWER FOR RADIATION-COOLED MPD THRUSTORS

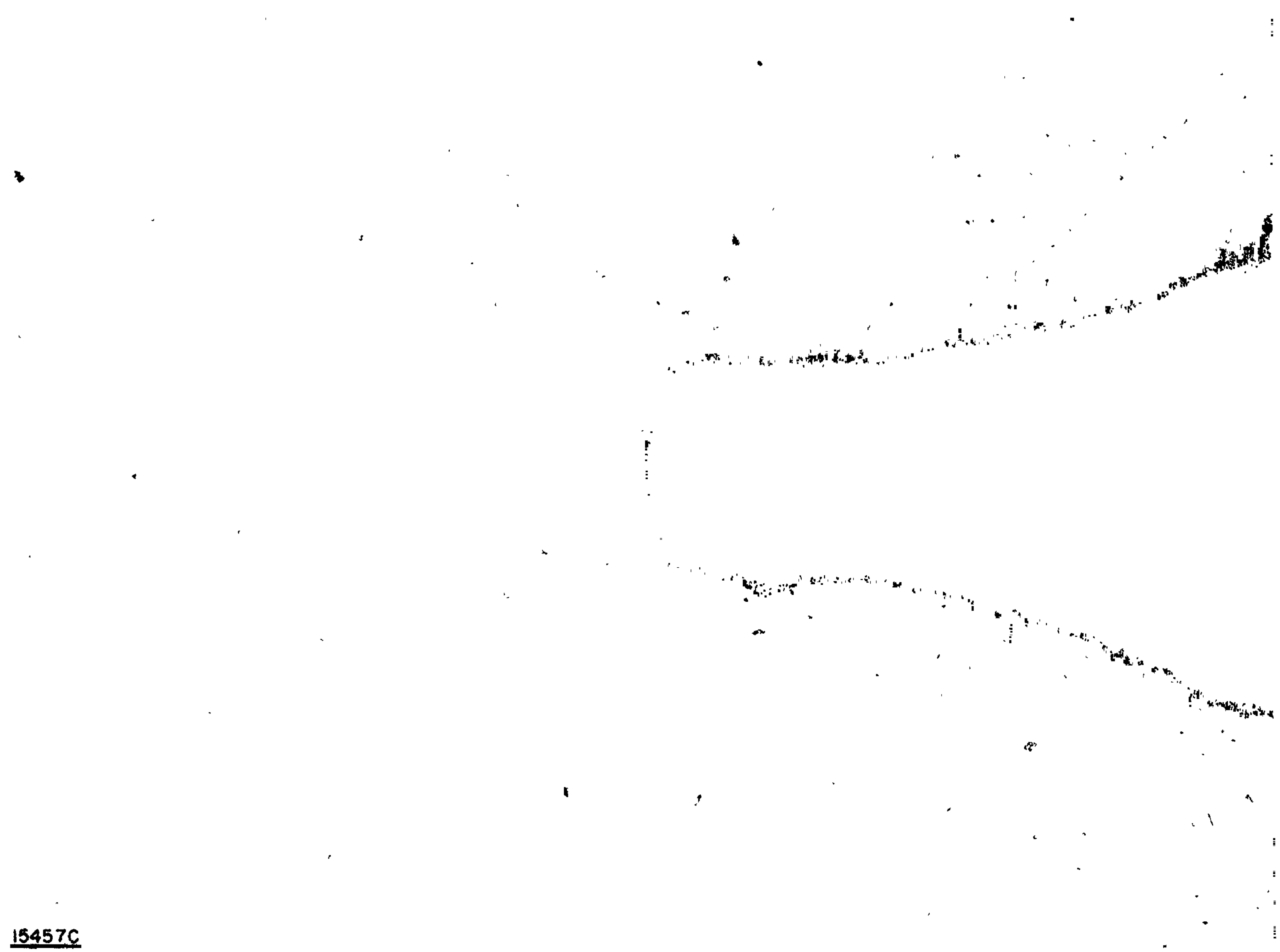

15457C

Figure 31 PHOTOGRAPH OF X-7CR MPD THRUSTOR DURING 75-HOUR LIFE TEST

III. MAGNET DESIGN CONSIDERATIONS

A. MAGNETS FOR ENGINE PERFORMANCE TESTS

The MPD arcjet thrustor has been under evaluation at Avco/SSD in configurations which utilized externally applied magnetic fields in the discharge region. The thrustors have been operated in the 10- to 50-kilowatt range; externally applied magnetic field strengths have ranged from 250 gauss up to 2.5 kilogauss.

To date, little effort has been expended in fabricating a magnetic field coil configuration for optimum magnet power utilization. Field coils have been made simply by winding copper tubing around a mandrel. Some of the more obvious advantages of this method for laboratory evaluation of magnetic field effects upon engine operation follow:

1. The coils may be water-cooled. This cooling permits the use of very high currents in the coils for achieving the high magnetic field strengths desired for evaluations.

2. Fabrication is extremely simple. New coil configurations may be fabricated in just a few hours.

3. Magnetic field strength distribution may be varied almost at will. Several magnet coils may be wrapped around the same mandrel and on top of previous coils. The several coils may be operated so that their fields are aiding or bucking each other, producing different ratios of the axial magnetic field strength, B_z, to the radial field strength, B_r.

4. Tubing is readily available, and no machining is required for the fabrication of coils.

5. Insulation of turns from each other is accomplished by sliding shrink-on tubing over the copper tubing.

The experimental results have indicated that engine operation is not appreciably affected by magnetic field strength distributions, and that the magnetic field produced by a solenoidal magnet coil is equally as effective as any other distribution tested. Insofar as field strength is concerned, our results have indicated that increases of magnetic field strength above approximately 2 kilogauss do not significantly improve either engine efficiency or specific impulse obtained.

The next section outlines some of the work which has been done at Avco/SSD to determine the weight penalties associated with a properly designated magnet subsystem. In view of the experimental results just mentioned, the following assumptions have been made for the purpose of the discussion:

1. The required magnetic field distribution can be obtained with a solenoidal magnet coil.

2. For reference purposes, the field strength at the core center may be taken as the basic design parameter.

3. The field strength at the core center will be of the order of 1 kilogauss.

4. The inner radius of the magnet coil will be of the order of 1 inch.

B. DESIGN OF RADIATION-COOLED MAGNETS

Approximate evaluations have been made of the weights of radiation-cooled magnet systems. Copper and aluminum have been considered as the solenoid materials. The following sections, although preliminary, form the basis for a complete evaluation of magnet subsystem weight requirements.

1. Solenoidal Electromagnets

The axial field strength at the center of the solenoid is given by the Fabry relation, which has the form[35]

$$B_z = G \left(\frac{P\lambda}{\rho r_i}\right)^{1/2} \qquad (29)$$

where B_z (kilogauss) is the magnetic field strength, G is a geometric factor which depends upon the coil geometry (i.e., ratio of outside to inside radii $r_o/r_i \equiv \alpha$, and length-to-diameter ratio, $l/2r_i \equiv \beta$), P(megawatts) is the power input, λ is the fraction of the coil occupied by the conductor, ρ (ohm-cm) is the resistivity of the coil material, and r_i (cm) is the inside radius of the coil.

The geometric factor, G, is a relatively weak function of the radii ratio, α, and the coil length-to-diameter ratio, β. Its maximum value is about 0.20 and corresponds to values of both α and β in the range 2 to 3. For the purposes of the following semiquantitative discussion, G will be assumed a constant equal to the maximum value of 0.20 and both α and β will be assumed to be of the order 2 to 3. From the viewpoint of the following analysis, these quantities have only a second-order effect on the calculated results, and by preselecting values of G, α, and β the problem of estimating magnet system weights is considerably simplified. In a later section, consideration will be given to two different coil designs and the effects of coil design upon the value of the geometric factor, G, and the magnet system weight.

Substituting $G = 0.20$ into Equation 29, the Fabry relation can be written

$$P = 6.25 \times 10^{-2}\, \rho r_i\, B_z^2/\lambda \qquad (30)$$

with dimensions: input power, P (kW), resistivity, ρ (10^{-6} ohm-cm), inner radius, r_i (inches), axial field strength, B_z (kilogauss), and the fraction of coil occupied by the conductor, λ (dimensionless). Equation 30, with the dimensional units as indicated, is used for the remainder of this discussion.

From the Fabry relation in the form of Equation 30, the solenoid power requirement is seen to be proportional to the square of the required axial field strength, directly proportional to the solenoid material resistivity and inner radius, and inversely proportional to the packing fraction, λ. The resistivity of the solenoid material is a function of temperature, increasing with an increase in coil temperature. For the purposes of the present discussion, it is assumed that the temperature within the entire coil is a constant, and in a later section it will be shown that a coil design for which this assumption is valid is also one for which the maximum value of the geometric factor, G, is obtained. Moreover, for a radiation-cooled magnet the same design will be shown to provide a packing fraction, λ, very close to unity; for the present, therefore, λ is assumed to be equal to one.

Figure 32 shows the resistivity of copper and aluminum as a function of temperature; therefore, as the temperature is increased, the resistivity of each material increases. Thus, for fixed magnetic field strength and inner solenoid radius, the required input power increases with increase in solenoid temperature (Equation 30). Figure 33 presents the magnet power input for a field strength of 1 kilogauss as a function of temperature, normalized to an inner radius of 1 inch. The power requirements for an aluminum solenoid are clearly seen to be greater than for a corresponding copper solenoid, but the total subsystem weight penalty will be seen to be somewhat smaller due to the reduced magnet coil weight obtained by the use of aluminum with its smaller mass density. In the next section the magnet weights associated with the two materials in a radiation-cooled configuration are considered.

2. Radiation-Cooled Magnet Subsystem

In this section, estimates of the weight of a radiation-cooled magnet subsystem are presented. The weight of a magnet is given by

$$W_{mag} = 2\pi r_i^3 \, W(a^2 - 1)\beta\lambda \tag{31}$$

where r_i is the inner solenoid radius, W is the density of the magnet material, and a, β, and λ have the same meanings as above. For the radiation-cooled magnet, λ is assumed to be equal to 1, and a and β are assumed to have values in the range 2 to 3. To a first approximation, then, the coil weight is given by

$$W_{mag} \approx 75\, r_i^3 \, W \tag{32}$$

For copper, $W \approx 550$ lb/ft^3, and the magnet weight is

$$W_{mag,\,cu} \approx 23.5\, r_i^3 \text{ pounds } (r_i \text{ in inches})$$

For aluminum, $W \approx 165$ lb/ft^3, and the magnet weight is

$$W_{mag,\,al} \approx 7.2\, r_i^3 \text{ pounds } (r_i \text{ in inches})$$

Figure 34 presents the total weight of the magnet subsystem, as a function of coil temperature, assuming a power supply weight of 50 lb/kW, a 1 kilogauss magnetic field strength at the coil core, and an inner radius of 1 inch. It is seen that for coil temperatures below 600°C, the smaller weight of an aluminum magnet coil compensates for the increased power input required and appears to be a somewhat more attractive system from the point of view of the weight penalty accruing to the use of the external magnetic field.

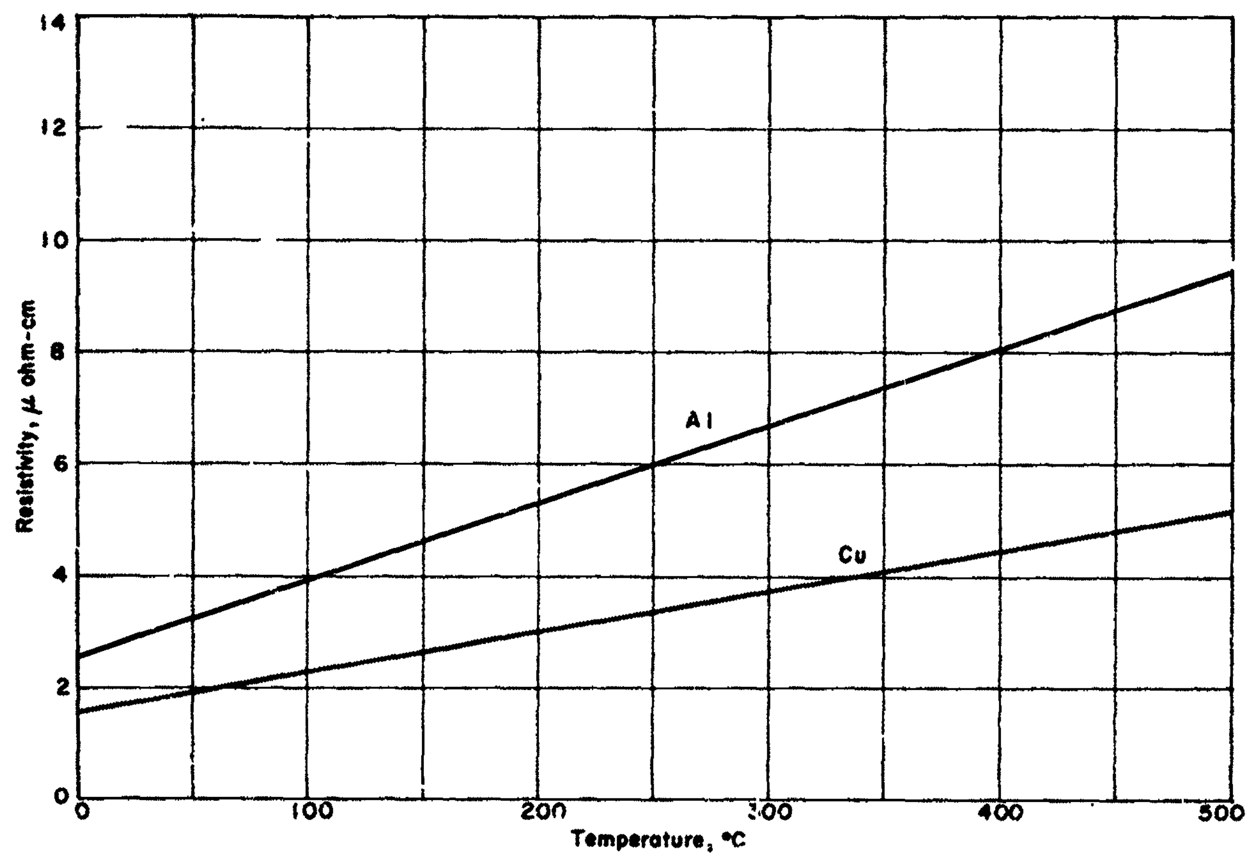

87-929

Figure 32 RESISTIVITY VERSUS TEMPERATURE FOR COPPER AND ALUMINUM

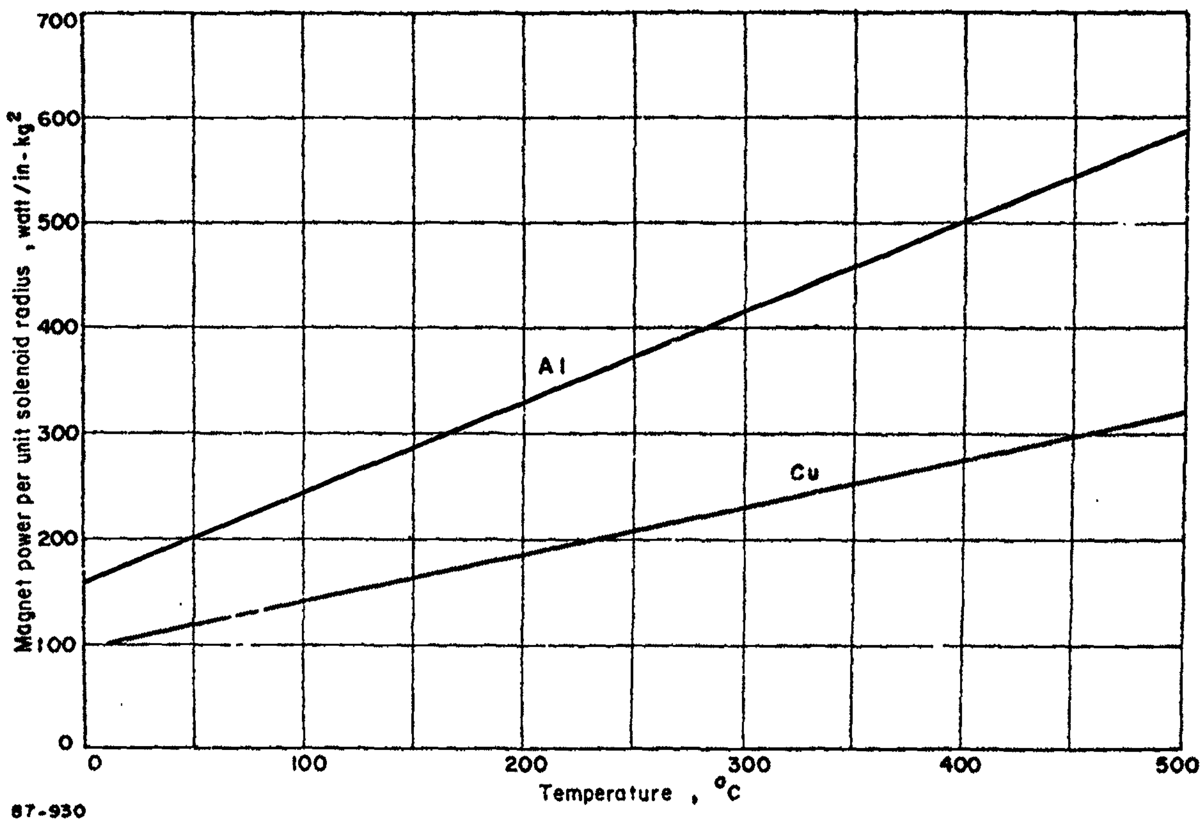

Figure 33 NORMALIZED MAGNET POWER VERSUS TEMPERATURE

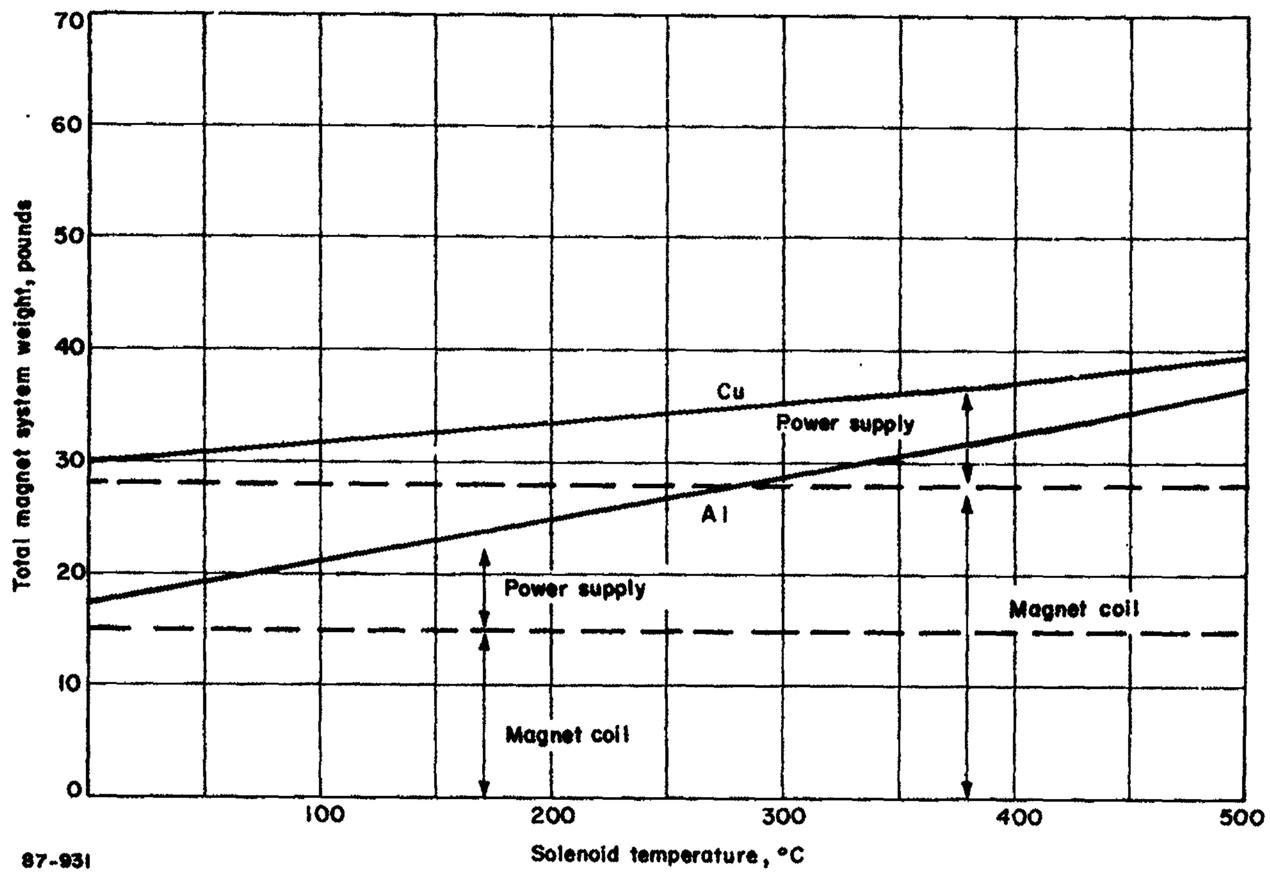

Figure 34 TOTAL MAGNET SYSTEM WEIGHT VERSUS SOLENOID TEMPERATURE

A major consequence from Figure 34 is that neither system imposes a weight penalty of as great as 50 pounds—provided the coil can be operated at temperatures below 600°C. The power requirement is less than 600 watts. For an engine operating in the 30- to 50-kilowatt range, the engine power supply weight is on the order of 1500 to 2500 pounds. The entire magnet subsystem then represents only about 2 to 3 percent of the engine power supply weight. Except for ease in fabrication, therefore, there is little reason to choose one of the materials considered over the other.

The one point which has not yet been determined is whether a radiation-cooled magnet can be operated at temperatures below 600°C. For a radiation-cooled magnet, all the input power must be radiated from the magnet exterior surface. The radiation area of the coil is given by

$$A = 2\pi r_i^2 (2\alpha\beta + \alpha^2 - 1) \tag{33}$$

and for the assumed values of α and β, the radiating area becomes

$$A \simeq 100 \; r_i^2 \; (cm^2) \tag{34}$$

For a 1-inch inner radius, the radiating area is thus of the order of 650 cm^2, and the total power which can be radiated is given by

$$P = 3.66 \times 10^{-9} \times \epsilon T^4 \text{ watts} \tag{35}$$

Figure 35 shows the power which can be radiated for both aluminum and copper as a function of temperature, superimposed upon a replot of the solenoid power versus temperature presented in Figure 33. The emissivity of copper has been taken as 0.6; that of aluminum has been taken as 0.11 to 0.19, in the temperature range of interest. The figure shows, in a rather dramatic fashion, that a copper magnet will operate at a temperature on the order of 300°C, will require approximately 225 watts of solenoid power, and will entail a total magnet power supply weight of the order of 35 pounds. An aluminum magnet, on the other hand, would melt, since it would be incapable of radiating all the input power unless its emissivity could be increased.

Several methods for increasing the emissivity suggest themselves. Probably the simplest consists of placing a plating (such as aluminum oxide) on the radiating surfaces of the aluminum magnet coil. At the temperatures of interest, no problems would be encountered with this plating process. The coating would increase the emissivity of the aluminum magnet coil, say, to 0.6, and the curve of power radiated shown in Figure 35 for copper would be equally valid for the aluminum magnet coil. For this configuration, then, an aluminum magnet would operate at 425°C, require an input power of 525 watts, and entail a total magnet and power supply weight of the order of 33 pounds. To within the approximations utilized for this discussion, the two materials impose the same weight penalty (approximately 35 pounds). This total weight includes provision for the power supply based on a specific power supply weight of 50 lb/kW.

Since the solenoid power is porportional to the square of the magnet field strength, the temperatures and power requirements associated with lower magnetic field strengths are greatly reduced. For lower magnetic field

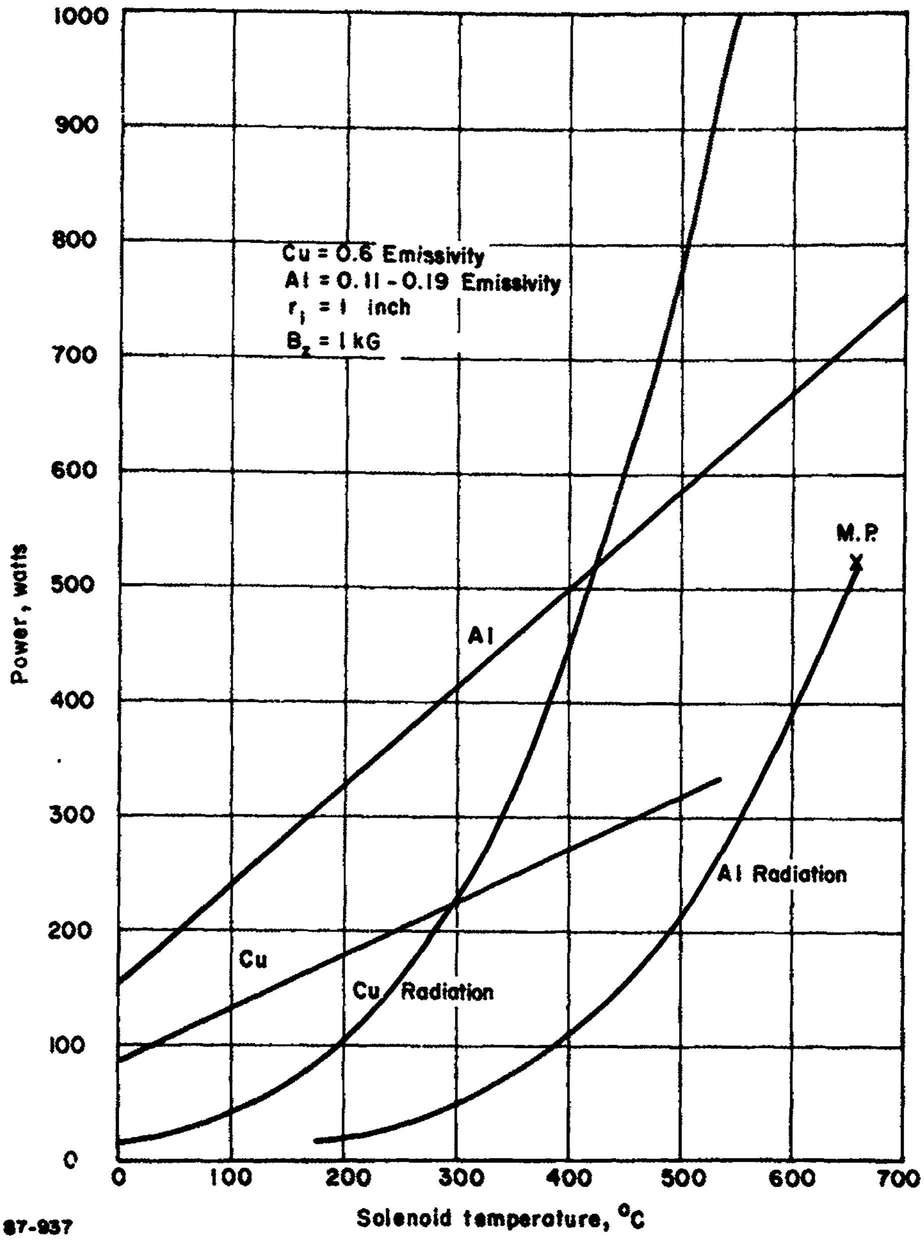

Figure 35 MAGNET POWER VERSUS TEMPERATURE

strengths, aluminum becomes a more attractive material than copper. Figure 36 presents the total magnet and power supply weight penalties incurred as a function of field strength for field strengths up to 1.4 kilogauss.

For field strengths below about 1 kilogauss, aluminum appears to be the more attractive magnet material. For field strengths above 1 kilogauss, the weight of the power supply for an aluminum magnet coil, as well as its operating temperature, rapidly increases. For field strengths of the order of 1 kilogauss, the absolute difference in system weight is entirely negligible, and either magnet coil could be utilized.

3. Magnet Coil Design

This section presents a brief outline of the differences between the normal "wire-wound" solenoid design, and a more efficient and compact design which was originally suggested by Bitter[36] and has most recently been improved by Johansen.[37]

The two geometries are most simply compared by considering the methods of fabrication and the resulting current distributions. The "normal" configuration is obtained by winding a square conductor into a solenoid, thereby achieving a uniform current density throughout the conducting coil. Each turn of the coil must be insulated from all other windings in both the radial and the axial directions, and the volume taken up by this insulation reduces the fraction of the coil volume which carries current, i.e., this design has a value of λ which is clearly less than 1. Moreover, radial heat conduction is inhibited by the insulation between the individual turns.

The axial magnetic field strength at the coil core and the input power may be related by the Fabry relation

$$B = G_1 \left(\frac{P\lambda}{\rho\, r_i} \right)^{1/2} \qquad (36)$$

where

$$G_1 = \frac{\mu_o}{\sqrt{2\pi}} \left(\frac{\beta}{a^2 - 1} \right)^{1/2} \ln \frac{a + \sqrt{a^2 + \beta^2}}{\sqrt{1 + 1 + \beta^2}} \quad ; \quad \mu_o \equiv \frac{4\pi}{10} \qquad (37)$$

a result first obtained by Fabry.[35] Values of G_1 have been tabulated by Cockcroft.[38] The maximum value which G_1 can attain is 0.18 and occurs for values of a and β in the vicinity of 2-3.

A more efficient design, generally attributed to Bitter,[36] is one in which the current density in the coil is inversely proportional to the radius and is fabricated by making pancake disks of conductor, which are cut through along a radius and joined to form a spiral-like surface. Figure 37 shows several disks; the coil is obtained by joining edges A to B and C to D in the illustration.

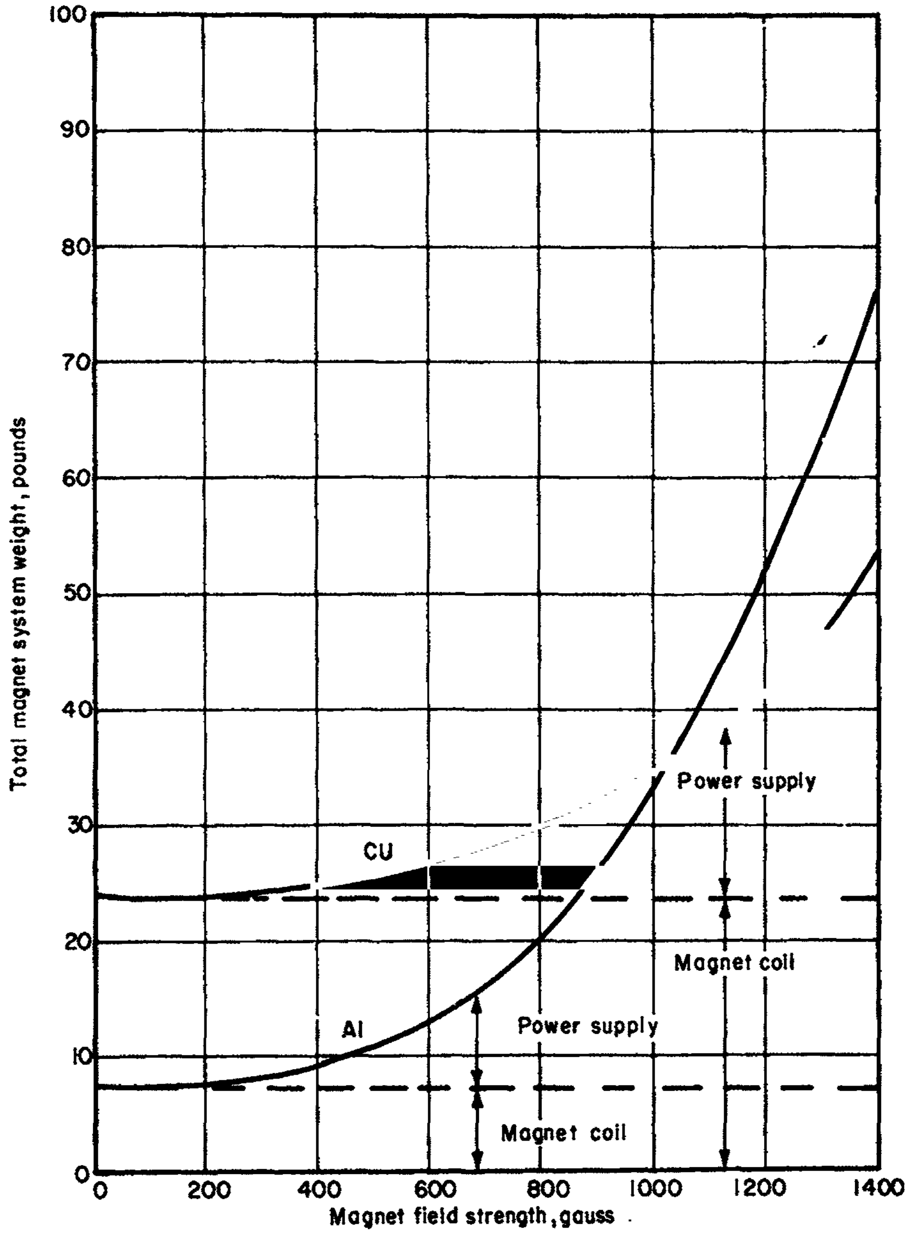

87-933

Figure 36 MAGNET SYSTEM WEIGHT VERSUS MAGNETIC FIELD STRENGTH

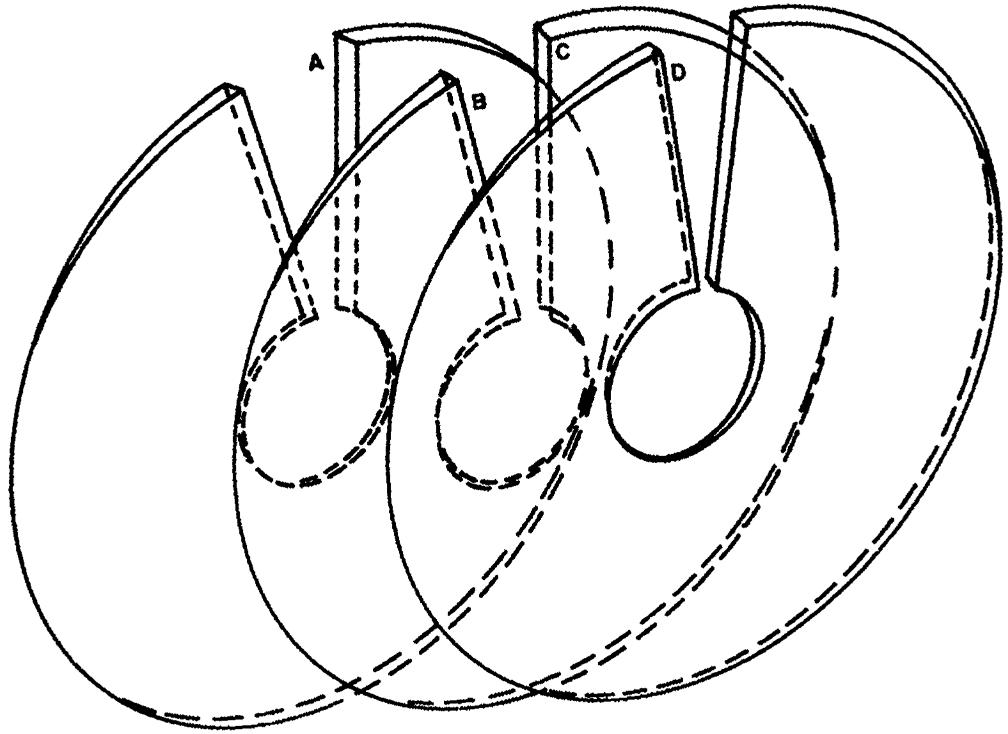

87-934

Figure 37 FABRICATION OF BITTER SOLENOID

The radial heat conduction in this configuration is not inhibited by insulating materials, since the only insulation required is between pancake sections. A further improvement suggested by Johansen,[37] is obtained if aluminum is used; each disk can be anodized and the insulation volume is then negligibly small. Thus, this design yields a value of λ very close to unity. Even if copper is used, the value of λ for this configuration is still much closer to unity than for the "normal" coil configuration.

For this configuration, the Fabry relation is given by

$$B = G_2 \left(\frac{P\lambda}{\rho r_i} \right)^{1/2} \tag{38}$$

where

$$G_2 = \frac{\mu_o}{2\sqrt{\pi}} \quad (\beta \ln a)^{-1/2} \quad \ln \left[a \quad \frac{\beta + \sqrt{1+\beta^2}}{\beta + \sqrt{a^2+\beta^2}} \right] \; ; \; \mu_o = \frac{4\pi}{10} \tag{39}$$

Values of G_2 are given in Reference 36. The maximum value attained by G_2 is 0.21 for a = 6 and β = 2. For a and β, in the vicinity of 2-3, G_2 is 0.2, the value which has been used in the sections above. If λ had the same value as the "normal" coil geometry, this configuration would still be about 10 percent more efficient. In practice, λ is greater for this design as well and the radial heat conduction is also improved. This magnet configuration, therefore, is more efficient from all considerations, and it forms the basis of the analysis above.

Finally, with the assumption that all the input power is radiated from the outer edge of the magnet coil, it is readily shown that the difference in temperature between the inner and outer coil surfaces is given by

$$\Delta T = \frac{P \;\; \ln \;\; a}{8\pi \; K\beta \;\; r} \tag{40}$$

For the situations considered above, this difference is of the order of only 1 to 10°C, and the previous assumption of constant coil temperature is completely valid.

C. TEST MAGNET CONFIGURATION

The calculated properties of the Bitter solenoid are sufficiently attractive to encourage experimental verification. For this reason a Bitter solenoid was constructed and operated, and data were obtained on magnet performance. Since this was an initial effort, the solenoid was not optimized and was constructed in the most straightforward fashion in order to provide experimental backing for the calculations.

The solenoid was fabricated of a stack of copper disks. A total of 64 disks, made from 1/32-inch copper sheeting, were used. Each disk had a 5.8-inch inner diameter and a 9.5-inch outer diameter. With the addition of insulating tape between the disks, the solenoid length was 3 inches, so that the packing fraction, λ , was 0.67. The magnet contained no cooling provisions except for that produced by natural convection and by radiation.

The geometrical factor, G_2, was calculated for this configuration and was found to be $G_2 = 0.095$. The value anticipated for an optimum design is about $G_2 = 0.20$, so the departures from optimum, produced largely by the relatively large inside diameter and the small length of this magnet, resulted in about a factor of 2 decrease from optimum in the constant, relating the field, B, to the square root of the input power. Thus, for a given B, four times the power required for an optimum geometry was needed.

The magnet was then tested on a laboratory bench. The measured quantities were current, voltage, temperature, and B_{max}, measured on the solenoid axis at about the midpoint of the solenoid length. The temperature was measured by a thermocouple embedded in the solenoid about 1/2 inch from the outer surface and midway between one solenoid face and a plane parallel to the face and passing through the solenoid center; thus, it was about 3/4 inch from one solenoid face and 2 1/4 inches from the other. The data are summarized in Table XIV below.

TABLE XIII

CALIBRATION OF RADIATION-COOLED BITTER SOLENOID

Current, amperes	128	160	200
Voltage, volts	4.9	8.25	12.8
Power in, kilowatts	0.63	1.32	2.56
B_{max}, gauss	430	530	660
T, °C	198	340	487

1. Data Correlation

The data of Table XIV have been examined for comparison with the relevant analytical expressions. First, the relation between field strength and input power was tested using handbook values of the resistivity of copper as a function of temperature. Therefore, since

$$B = 0.095 \left(\frac{P\lambda}{\rho\, r_i}\right)^{1/2} \qquad (41)$$

B can then be predicted as a function of input power, since λ and r_i are known constants and ρ is obtained from T. The predicted and measured values of B are given in Table XV below.

TABLE XIV

COMPARISON OF PREDICTED AND MEASURED FIELD STRENGTH, BITTER SOLENOID

Power in, kilowatts	0.63	1.32	2.56
B, predicted, kilogauss	0.42	0.52	0.635
B, measured, kilogauss	0.43	0.53	0.66

The agreement is excellent. One can check also that the power balance on the magnet is correct; that is, it can be determined whether the resistivity values determined by the temperature are in accord with the measured voltage and current. To do this, it is first necessary to write the solenoid resistance in terms of the geometry and resistivity. It can easily be shown, if the solenoid is isothermal, that resistance R of one disk is given by

$$R = \frac{2\pi\rho}{\delta \ \ln \ r_o/r_i} \tag{42}$$

where δ is the disk thickness. With the modification that there are 64 disks in series, this relation can be used to predict the solenoid resistance as a function of temperature. Table XVI below compares the predicted solenoid resistance with the measured resistance (V/I) for the calibration tests.

TABLE XV

COMPARISON OF MEASURED AND PREDICTED SOLENOID RESISTANCE

Solenoid Temperature, ^{o}C	198	340	487
ρ, microhm-centimeters	3	4	5.2
R, measured, ohms	3.82×10^{-2}	5.15×10^{-2}	6.41×10^{-2}
R, predicted, ohms	3.06×10^{-2}	4.08×10^{-2}	5.33×10^{-2}

Thus, the measured resistance exceeds the predicted resistance in each case by about 10 milliohms, which is the correct order of magnitude for the various contact resistances.

Finally, the magnet thermal balance may be examined. In steady state all the power input to the magnet is thermalized, then removed by radiation and convection. It is assumed that conduction is small. Again, with the assumption that the magnet is isothermal, the radiative term can be computed as $\epsilon\sigma A \ T^4$, with T in ^oK. Taking $\epsilon = 0.8$,

$$P_{rad} = 0.8 \times 5.67 \times 10^{-12} \times 1.2 \times 10^3 \times T^4 \tag{43}$$

$$= 5.45 \times 10^{-9} \cdot T^4$$

where the radiating surface area of the solenoid is estimated at 1200 cm^2.

For the cooling owing to natural convection, standard formulae yield

$$q/A \sim 1.5 \, \Delta T \tag{44}$$

where q is the heat transfer in Btu/hr, A is the area in square feet, ΔT is the temperature difference in ^{o}F, and the heat transfer coefficient is taken as 1.5. In cgs units, the same relation is written as

$$q/A \sim 8 \times 10^{-4} \Delta T \qquad (45)$$

with q in watts.

Thus, with $A \sim 1200$ cm^2,

$$q \sim \Delta T \qquad (46)$$

The heat transfer from the solenoid is then given by

$$\dot{Q}\,(watts) = 5.45 \times 10^{-9}\ T^4 + \Delta T \qquad (47)$$

This predicted heat transfer is compared with input power in Table XVII below.

TABLE XVI

COMPARISON OF PREDICTED SOLENOID HEAT TRANSFER WITH INPUT POWER

Temperature, °C	198	340	487
Predicted Radiative Transfer, Watts	262	770	1820
Predicted Convective Transfer, Watts	170	308	459
Predicted Total Transfer, Watts	432	1078	2279
Input Power, Watts	630	1320	2560

The difference between predicted heat transfer and input power is about 30 percent at the low input power and falls to about 12 percent at the high input power. Some of the difference is almost certainly associated with conductive cooling, which has been neglected.

2. Conclusions

The rather good correlation of magnet performance with the analytical predictions suggests that a fairly high order of accuracy can be obtained in the design of a Bitter solenoid and that, further, the magnet system analyses are probably reliable predictors of optimum magnet performance.

Magnet construction is not unduly complex or difficult. The substitution of a cohesive insulator (such as an oxide layer) for the separate insulators used here would make construction even simpler and improve the packing friction, λ .

Most important, the magnet temperature is a key determinant of required input power: the higher the temperature the more power is required for a given B, and the higher the input power the higher the temperature for a fixed geometry. Thus, the radiation-cooled solenoid is much less attractive for high field strengths, with the power required probably increasing more rapidly than B^2 even for an optimum design. Further, a critical element in the design is the rejection of thrustor heat by some technique (such as reflection), since increases in magnet temperature are to be avoided where possible.

IV. DIRECTIONS FOR FUTURE RESEARCH

At this time the MPD arcjet has emerged from the early laboratory stage to a more advanced stage of development. While many questions remain with regard to the detailed mechanism of thrust production and, more importantly, with regard to the interaction of the thrustor with the test environment, it is still possible to assert with some confidence that

1. propulsive efficiency levels of 40 to 50 percent at the 4000 second impulse level are achievable with ammonia,

2. magnet system designs appear favorable, and

3. radiation-cooled thrustors for long mission flight times can be developed.

For this reason it is suggested that future research and development might be more properly oriented toward hardware. Tasks of interest include:

1. development and life test of a radiation-cooled thrustor with an optimum design radiation-cooled magnet

2. consideration of power conditioning requirements and development of breadboard power conditioning systems

3. laboratory tests designed for the express purpose of minimizing interaction with the environment, rather than optimization of measured performance

4. preliminary planning for flight tests to resolve the question of tank interaction is appropriate.

APPENDIX

MPD ARCJET THRUSTOR ANALYSIS

BY J. B. WORKMAN

A. INTRODUCTION

This appendix describes the analysis of an arc structure in a flowing gas which is ionized and heated by a coaxial electric discharge in a magnetic field. The geometry consists of an axial steady flow, a magnetic field parallel to the flow, and an applied electric field which is radial between the two cylinders forming the annulus. This type of discharge, known as the magnetic annular arc (MAARC), has been the subject of many experimental investigations in recent years and forms the basis for a family of magnetoplasmadynamic (MPD) accelerators.[40-44] The early interest in this class of plasma device was generated by the desire to achieve a useful plasma accelerator which would convert electrical energy into mechanical thrust suitable for space propulsion. Recently, a new interest in these MAARC discharges has developed because of their use as high energy plasma sources for laboratory simulation of solar wind phenomena[45] and collisionless plasma flow studies.

The distinguishing feature of this type of coaxial electrical arc is the presence of the axial magnetic field in the discharge region. A number of related plasma experiments[46-48] have been carried out in this configuration. The common characteristic is that the electrons undergo complete orbits between collisions, thereby creating Hall currents that circulate around the center electrode in the annulus. This type of arc has been used for a wide spectrum of plasma devices ranging from space thrusters with power levels of 10^4 watts up to plasma accelerators for flow studies of 10^7 watts, all with channel cross sections of a few centimeters. Because this discharge is useful for both plasma physics studies and applications with the capability of creating a highly ionized steady flow of plasma, the present analysis will possibly be of interest to more investigators than just those involved in the development of magnetic annular arcs and magnetoplasmadynamic arcs.

In the course of interpreting experimental results, various authors have developed integral or average property analyses for examining particular devices. For example, in the earliest work of this sort, Hess[49] has estimated the various mean free paths and collision frequencies for his device in order to predict the Hall parameters. With this information he was able to discuss the direction and magnitude of ion and electron currents. Later, Cann and Marlotte[50] greatly extended this approach by considering integrated conservation relations for the gas. The results of their analysis permit experimental measurements to be correlated in such a way that overall conservation of mass, momentum, and energy can be satisfied. Recently, Hugel, Kruelle, and Peters[51] have summarized this approach in their paper and indicated its usefulness in discussing their experiments. In a current paper, Rosciszewski[52] has used this approach to analyze a low density model suggested by Lovberg.[53]

Unfortunately, the apparent complexity of the flow in these devices has provided little incentive for a more detailed theoretical treatment. In particular, the geometry seems two- or possibly three-dimensional in nature, the ratio of electron cyclotron to collision frequency is of order unity, and complex ionization and dissociation reactions occur. Recently, however, several investigations have indicated that the majority of the current flows in a narrow region near the throat of these devices.[54-55] This implies that the important part of the arc structure itself may be confined to a thin zone that is both geometrically simple and with gas densities sufficiently high that collisional processes dominate over collective plasma effects.

The objective of the present research is twofold: 1) to carry out a detailed numerical analysis of the non-equilibrium chemistry and flow in this throat region, using a quasi-one-dimensional geometry, and 2) to derive from the numerical results a simple physical model which is useful for visualizing the important processes and studying parametric behavior. The numerical analysis is capable of determining various constants for the simple model that would otherwise have to be supplied in an ad hoc manner. The goal is to demonstrate that a self-consistent model can be constructed which shows a large current zone near the throat, producing levels of ionization, dissociation, and gas enthalpy that are consistent with experimental results. By limiting the investigation to the throat and the upstream subsonic portion of the arc, it is possible to delve quite deeply into the structure of the discharge without getting entangled in the complexities of the flow-magnetic field interaction which must occur further downstream.

Multicomponent conservation equations, together with the appropriate Maxwell relations, are solved for a discharge in hydrogen for a subsonic, steady flow. Rate equations for ionization and dissociation, along with appropriate relations for the various transport processes, are employed as constitutive equations. To the writer's knowledge this is the first attempt to analyze the structure of an arc by integrating this set of equations through the discharge.

The analytic results indicate that the flow through the discharge has properties similar to compressible flow in a constant area pipe with heat addition. The familiar increase in the Mach number with heating is obtained with a condition that sonic flow must be reached at the downstream edge of the channel. In this case, the heat source is the joule dissipation due to arc currents. Certain criteria which determine the power required to bring the Mach number to unity at the throat location, together with the requirement that the solution pass through the sonic point smoothly, establish effective boundary conditions downstream of the throat. These results can be used as a basis for the theoretical treatment of the supersonic exhaust downstream of the throat, but a detailed description of this portion of the plasma flow is beyond the scope of this paper.

The simple flow model which is developed in Subsection G provides a series of elementary relations which are useful for estimating discharge length, fraction ionized, and the connection between pressure, mass flow, and current.

B. PHYSICAL MODEL

A typical arrangement of cathode and anode in a magnetic annular arc is that used in the experiments conducted at this laboratory.[56] The geometry (Figure A-1) consists of a constant area annulus joined at a throat to an expanding area region with an external magnetic field which is applied parallel to the flow direction. While a wide variety of shapes have been used to form magnetic arcs, they all appear, in general, to have a discharge zone that roughly approximates this device.

By assuming axial symmetry and time invariance and by neglecting radial variations, this flow geometry can be described by quasi-one-dimensional, steady hydrodynamics. With one exception to be noted, the azimuthal magnetic field induced by the radial current can be ignored. The analysis will be confined to the vicinity of the throat where the calculation can be compared to experimental flow properties at a mean annular radius. By simplifying the geometrical considerations, one can investigate the chemistry and flow in great detail while still retaining a tractable computation scheme.

Computations have been carried out for hydrogen by considering the four components: H_2, H, H^+, and e. The species H_2^+ created by electron impact is assumed to dissociate rapidly into H and not form an important constituent of the flow.

In the axial or flow direction, the two neutral species are assigned a common velocity U_n, different from that of the ionized species U_i. Electrons and ions have the same axial velocity by virtue of assuming equal sources and charge neutrality. Microscopically, the charged species are tied together by an axial electric field as in ambipolar diffusion.

In the azimuthal direction all of the heavy species are assigned a common velocity, U_s, different from that of the electron gas, U_e (Hall current). If the flow is steady with no azimuthal variations, there is no azimuthal electric field to couple electrons to ions, and the only interaction is through collisions.

The heavy species are taken as having a Boltzmann energy distribution at a common temperature T_H, while the electrons are assigned a different temperature T_e. A Boltzmann distribution also pertains to the electrons, except that a modification to the high energy tail is introduced in calculating the various electron-neutral excitation losses. This is necessary in those regions of the flow where the electron-electron collision frequency is so low that a Druyvesteyn cutoff of the high energy spectrum is expected.

The Druyvesteyn distribution in a partially ionized gas is obtained when the energy communication between electrons ceases to exist. The significant parameter that distinguishes the limit is $m_{H_2} \nu_{ee} / m_e \nu_{en}$, where m_e and m_{H_2} are electron and neutral masses and ν_{en} and ν_{ee} are electron-neutral and electron-electron collision frequencies. A simple attenuation factor α which ranges from zero to unity, depending on this parameter, may be defined as

$$\alpha = \frac{1}{1 + \dfrac{m_e \nu_{en}}{m_{H_2} \nu_{ee}}} \qquad \text{(A-1)}$$

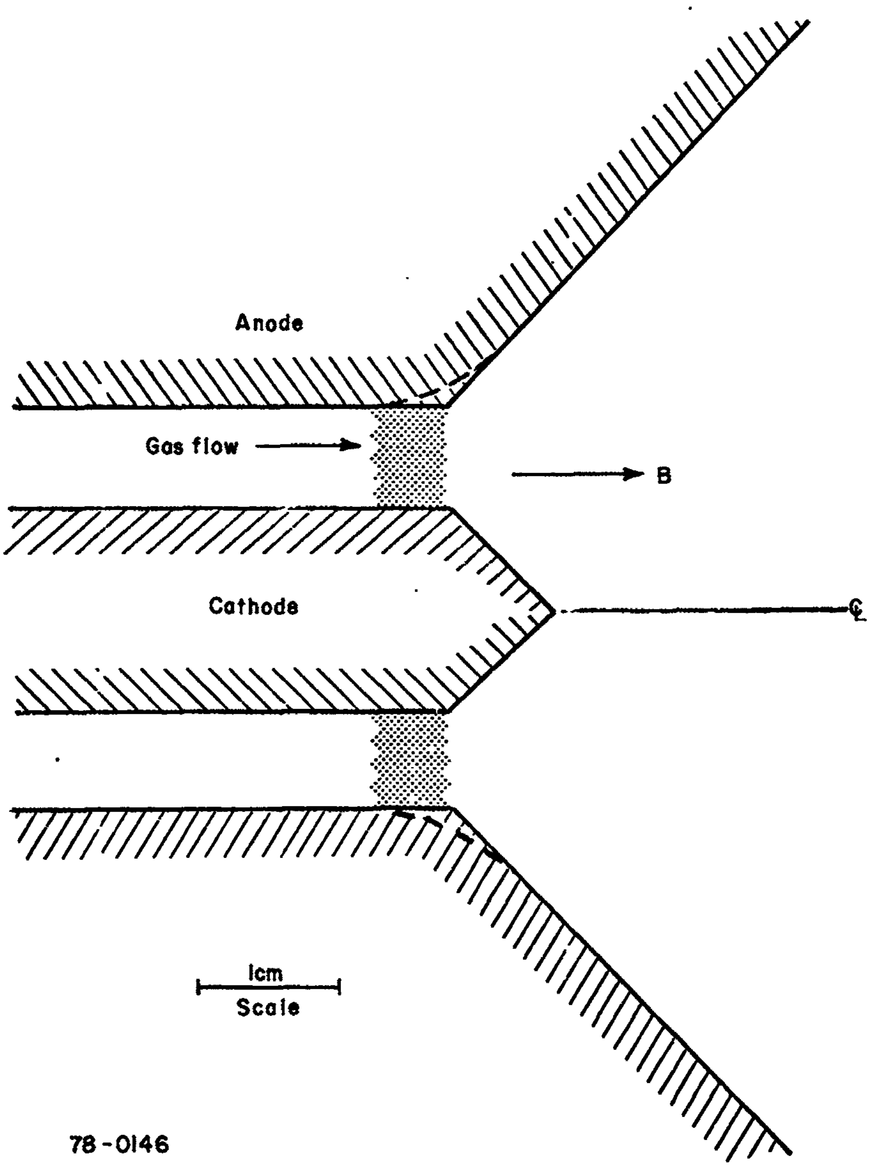

Figure A-1 MAGNETIC ANNULAR ARC

Scale diagram of experimental arrangement for Reference 54. The dotted region is the high current density zone. The analysis assumes a sharp corner anode; the experimental one is slightly rounded as shown by dashed lines.

By multiplying the rates obtained for a Boltzmann distribution by this factor, one can correct the results to allow for the effect. In practice this factor is close to unity over most of the discharge; thus this refinement has little influence on the solution.

In the transverse or radial direction, only the motion of electrons will be considered. Since this flux constitutes the external current to the arc, it will be denoted as j , and the corresponding simple momentum equation will be written as an electrical conductivity.

The concentration of each species will be found by calculating the appropriate dissociation and ionization rates. Recombination is neglected as an unimportant process at the temperatures to be considered. The ionization rates of hydrogen molecules and atoms denoted by g_M and g_A are found as a function of electron temperature by integrating a Boltzmann distribution against experimental cross sections. All of the cross sections to be used in this work have been taken from the data book of Brown.[57]

The dissociation of hydrogen by electron impact follows the model of Poole's work given by Massey and Burhop,[58] with the first excited level rate denoted by g_{D_1} and the second by g_{D_2}. This excitation results in significant inelastic energy transfer from electrons to heavies denoted by G_{eH} and radiative loss G_R. The latter is assumed to escape from the gas. In addition to these inelastic processes, the usual elastic energy transfer from electrons to heavies, H_{eH}, is taken into account.

Heat conduction, q , by electrons in the flow direction is treated by using the thermal conductivity, λ , for a partially ionized gas. This is proportional to the product of electrical conductivity, σ , and electron temperature. The constant of proportionality is chosen so as to give the result of Spitzer[59] when the gas is fully ionized. The electrical conductivity itself employs experimental cross sections for the neutrals and a Coulomb cross section that gives the Spitzer result for full ionization. Heavy particle heat conduction is neglected, as is any thermal conductivity across magnetic field lines to the walls.

C. COMPUTATIONAL PROGRAM DETAILS

1. Collision Cross-Section Data

For simplicity, the elastic cross sections of electrons and ions with neutral particles were chosen to be equivalent hard spheres referenced to mean particle energies appropriate to the problem. Considering that the absolute value of these quantities is somewhat uncertain at low energies, this is felt to be a reasonable approximation. Fortunately, the data that is available indicates only a relatively weak dependence on energy in the regime of primary interest.

Using the data in Brown[57] and referencing the electron energy to 4 e.v., the electron-neutral cross sections were deduced from Figures 1.4 and 1.5 to be $Q_eH_2 = 1.4 \times 10^{-15}$ cm^2 and $QeH = 2.8 \times 10^{-16}$ cm^2 corresponding to $P_c = 48$ and $P_c = 10$ respectively.

The equivalent hard sphere data for ion-neutral cross sections was obtained from mobility data. For H_2, the value of μ = 13 cm/sec - cm/v, given by Figure 3.48, gives an effective cross section for $H^+ - H_2$ of $QiH_2 = 7.1 \times 10^{-15}$ cm^2. This compares well with the low energy limit that would be obtained by extrapolating the direct information of Figure 1.50 (P_c = 250). For the collision $H^+ - H$, there is, of course, no direct information on mobility at low energies and the usual approximation of scaling the $H_e^+ - H_e$ collision was used. Using the value of μ = 11 cm/sec - cm/v given by either Figure 3.25 or Figure 3.39 results in $QiH = 4.85 \times 10^{-15}$ cm^2. This is in agreement with an extrapolation to low energies of the direct atomic hydrogen data of Dalgarno and Yadov.[60]

The electron-neutral ionization rates have been computed as a function of electron temperature by integrating a Boltzmann distribution against a linear curve fitted to the low energy portion of experimental cross-section data in Brown. For H_2, the curve of Figure 4.4 was used; and for H, the curve of Figure 4.18. This results in the following expressions (MKS units):

$$g_M = 2.365 \times 10^{-12} \sqrt{T_e}\,(26.15 + 2.76 \times 10^{-4}\, T_e)\, e^{-\frac{18.9 \times 10^4}{T_e}} \qquad \text{(A-2)}$$

$$g_A = 3.03 \times 10^{-13} \sqrt{T_e}\,(21.6 + 2.76 \times 10^{-4}\, T_e)\, e^{-\frac{15.65 \times 10^{-4}}{T_e}} \qquad \text{(A-3)}$$

The treatment of the electron-molecule excitation and dissociation processes follows the theory of Massey and Burhop[58] for the experimental results of Poole. Using the cross sections given on page 237 and integrating with a Boltzmann distribution gives the following results (MKS units):

$$g_{D_1} = 2.46 \times 10^{-17} \sqrt{T_e} \left[\left(e^{-\frac{11.00 \times 10^4}{T_e}} \right) \left(\frac{11.00 \times 10^4}{T_e} + 1 \right) - \left(e^{-\frac{44.00 \times 10^4}{T_e}} \right) \left(\frac{44.00 \times 10^4}{T_e} + 1 \right) \right] \qquad \text{(A-4)}$$

$$g_{D_2} = 8.20 \times 10^{-18} \sqrt{T_e} \left[\left(e^{-\frac{13.9 \times 10^4}{T_e}} \right) \left(\frac{13.9 \times 10^4}{T_e} + 1 \right) - \left(e^{-\frac{55.6 \times 10^4}{T_e}} \right) \left(\frac{55.6 \times 10^4}{T_e} + 1 \right) \right] \qquad \text{(A-5)}$$

The Coulomb cross section is chosen to match the expressions for electrical conductivity given by Spitzer.[59] Fitting to Equation 5-37 (MKS units), there results

$$Q_{ei} = 2.96 \times 10^{-10} \frac{\ln \Lambda}{T_e^2} \tag{A-6}$$

where

$$\Lambda = 1.25 \times 10^7 \left(\frac{T_e^3}{n_e}\right)^{1/2}$$

Thence the usual expression for conductivity in a partially ionized gas becomes

$$\frac{1}{\sigma} = \frac{\gamma M_e C_e}{n_e e^2} \sum_j n_j Q_{ej} \tag{A-7}$$

where γ is Spitzer's correction for a strong transverse magnetic field. Likewise an expression for thermal conductivity is obtained by fitting to Equation 5-45 as

$$\gamma = 5.68 \times 10^{-8} T_e \sigma \tag{A-8}$$

2. Linearized Equations

In order to start the computation in a systematic and rational way, the basic equations are linearized about the upstream conditions. This is done merely to obtain initial conditions on the ionized gas species in the flow regime where they are negligibly small compared to the background gas. The electron density is taken as a small quantity $n_e = n_e'$ and the electron temperature is taken as a small perturbation about the usual elevated value, T_{e_o}, in an electric field $T_e = T_{e_o} + T_e'$.

Substituting into the electron energy equation and rataining only first order terms, one obtains an expression which, when coupled to the transport property relations, permits a solution for T_{e_o} and U_{e_o} .

$$0 = \frac{J^2}{\sigma} + M_{es} U_e - H_{eH} \tag{A-9}$$

where

$$JB = M_{es}$$

$$J = \sigma (E - U_e B)$$

$$\sigma = \frac{n_e' e^2}{\gamma M_e c_e n_o Q_{eH_2}}$$

$$H_{eH} = \frac{2 n_e' M_e c_e k Q_{eH_2}}{M_{H_2}} (T_e - T_o)$$

Solving these relations simultaneously, the quantity n_e' completely drops out of the formulation (as it should), and one obtains unique values for T_{e_o} and U_{e_o}.

Now, substituting into the axial electon/ion momentum equation and again retaining only first order terms gives an expression for n_e'

$$\frac{dP_e}{dx} + \frac{dP_i}{dx} = - M_{in} + JB_\theta \qquad \text{(A-10)}$$

or

$$\frac{dn_e'}{dx} = \xi_1 n_e' \qquad \text{(A-11)}$$

where ξ_1 is only a function of upstream flow parameters:

$$\xi_1 = \frac{4/3\, M_i U_o c_{iH_2} n_o Q_{iH_2} + \dfrac{e^2 (B - U_{e_o} B) B_{\theta_o}}{\gamma M_e c_e n_o Q_{eH_2}}}{k(T_{e_o} + T_o)} \qquad \text{(A-12)}$$

Integrating, one obtains

$$n_e' = e^{\xi_1 (x - x_o)} \qquad \text{(A-13)}$$

where x_o is an arbitrary constant. The quantity $1/\xi_1$ is, of course, the characteristic diffusion length for the ionized gas.

Note that the quantity, U_i, has been taken to be small throughout. This can be justified by a substitution of the solution for n_e' directly into the continuity equation which shows $\Gamma_e' = n_e' U_i$ to be a second order quantity. This assumes, of course, that there is no constant T_{e_o} term or upstream source of ionization.

Returning to the energy equation, the solution for n_e' is substituted into the full equation, and terms up to second order are retained. The result is a second order equation for T_e' .

$$\frac{d^2 T_e'}{dx^2} + \xi_1 \frac{dT_e'}{dx} + K_1 T_e' = K_2 e^{\xi_1 (x - x_o)} \tag{A-14}$$

where K_1 and K_2 are functions of the upstream parameters as shown below.

Let

$$K_3 = \frac{c_e M_e n_o Q_{eH_2}}{\sqrt{T_e}} \tag{A-15}$$

$$K_4 = \frac{\sqrt{T_e}\ e^2}{\gamma M_e c_e n_o Q_{eH_2}} \tag{A-16}$$

$$K_5 = \frac{2 M_e c_e k Q_{eH_2}}{\sqrt{T_e}\ M_{H_2}} \tag{A-17}$$

Then define the following coefficients by evaluating λ , a , and the g's for n_o , T_{e_o} :

$$K_6 = \frac{\lambda}{n_e} \tag{A-18}$$

$$K_7 = \frac{a\, n_o}{n_e} \Big[g_M \left(1/2\, k\, T_{e_o} + \xi_M\right) + g_{D_1} \left(G_{eH} + \xi_D\right)$$

$$+\; g_{D_2} \left(G_{eH} + G_R + \xi_D\right) \Big] \qquad \text{(A-19)}$$

Then let

$$K_8 = \left(\frac{K_3}{K_4}\right)^2 T_{e_o}^2 + 2 \left(\frac{K_3}{K_4}\right) T_{e_o} + B^4 \qquad \text{(A-20)}$$

$$K_9 = \left[\left(\frac{K_3^2}{K_4}\right) E^2\, T_{e_o} + K_3\, E^2 B^2 \right] \left[2 \left(\frac{K_3}{K_4}\right)^2 T_{e_o} + 2 \left(\frac{K_3}{K_4}\right) \right] \qquad \text{(A-21)}$$

Now

$$K_1 = \frac{\sqrt{T_{e_o}}}{K_6} \left[\frac{\left(\frac{K_3^2}{K_4}\right) E^2 K_8 - K_9}{K_8^2} - K_5 \right] \qquad \text{(A-22)}$$

$$K_2 = \frac{K_7}{K_6} \qquad \text{(A-23)}$$

There is only one admissible solution to the equation (the other root goes to infinity at large upstream distances).

$$T_e' = A\, e^{\xi_2 (x - x_o)} + K_{10}\, e^{\xi_1 (x - x_o)} \qquad \text{(A-24)}$$

where A is an arbitrary constant and K_{10} , ξ_2 are given as functions of the upstream parameters.

$$\xi_2 \quad \sqrt{\left(\xi_{1/2}\right)^2 - K_1} - \xi_{1/2} \tag{A-25}$$

$$K_{10} \quad \frac{K_2}{2\xi_1^2 \cdot K_1}$$

In practice, one discovers that the last term is typically unimportant and one can write

$$T_e' = A\, e^{\xi_2 (x - x_o)} \tag{A-26}$$

The whole purpose of this linearization exercise is to connect all of the small quantities associated with the ionized species in a convenient manner prior to starting the numerical integration of the full non-linear equations. The parameter A specifies which grouping one is working with, while x_o merely sets a reference value for the distance scale. To start the actual computer solution, one chooses a value of x sufficiently far upstream that the ionized gas represents only a negligible perturbation on the background neutral species.

This mathematical procedure assures that the numerical integration will start without oscillations and produce a smooth solution. In practice, one can start from any collection of arbitrarily small quantities and generate solutions similar to the present results. However, in general this approach leads to large fluctuation in the early steps of the integration. In addition, it provides for no systematic way of locating the particular set which will traverse the sonic point properly.

3. Computer Solution

The actual numerical integration of the full non-linear equations is carried out in a straightforward manner. There are nine basic physical quantities and associated derivatives. At each step one knows the value of each quantity and can solve the conservation equations simultaneously to get the derivatives. This is merely an algebraic reduction of linear equations. Thence, with the derivatives in hand, one moves a small distance in x and recomputes the new values for each quantity. A Runge-Kutta procedure is used to correct the value of the derivatives after each step to assure the best possible fit. The step size itself is adjusted downwards until the overall error is within approximately 1 percent. The computations were carried out on an IBM 7090.

a Start

1) Use initial quantities from the incoming cold flow:

$$n_{H_2}, T_H, U_n$$

2) Start with no dissociation, $n_H = 0$

3) Start the computer solution with an initial value of n_e that is small enough that the background flow is not initially disturbed, but large enough that computer running time is not excessive. A good choice is probably 10^{-4} of cold flow density. The reference value for the distance scale, x_o , can be set equal to zero for simplicity.

4) Arbitrarily pick a range of values for the parameter, A. Thence, from the linearized equations, all of the other initial quantities for the electron/ion gas are specified.

5) Once all of the initial thermodynamic properties of each of the species has been specified in this manner, the starting point is the same as any other station in the calculation.

b. Typical Step-by-Step Procedure

1) Given all of the thermodynamic quantities for each species, compute corresponding electrical and thermal conductivities, all transfer terms, and all of the coefficients of the differential equations.

2) Taking the derivatives in finite difference form: $\Delta n_e/\Delta x$, $\Delta n_{H_2}/\Delta x$, etc., the differential equations yield a set of linear algebraic equations, which are readily solved for these derivatives.

3) Pick a Δx that permits no quantity to change by more than the accuracy desired, and compute the differentials in each of the thermodynamic properties.

4) Add all of the Δ's and proceed to the next station in x with all of the new thermodynamic quantities in hand.

5) To improve the accuracy, perform the calculation backwards from the new station; and using a Runge-Kutta procedure, take an appropriate average for each of the λ's at each station.

6) Proceed step-by-step in this manner until a sonic singularity appears in either momentum equation.

c. Sonic Points

1) The sonic points are treated by a combination of computer solutions and hand calculations. The arrival of the step-by-step calculation at a sonic point is indicated in the solution by a change in sign of the velocity derivative of either species. These derivatives are monitored by the computer solution, and the program is automatically stopped to permit inspection by the operator when reversal occurs.

2) If the singularity has occurred in the background neutral gas, one places the throat at this station in x and programs the appropriate area versus distance formula or table to be used in the computations from here on. Ideally, once one has programmed the throat location in this manner, the computer will now pass this station without the velocity derivative reversing sign. In practice, it is simpler to stop the computer solution just short of the sonic point, extrapolate the velocity across the sonic point by hand, and start the computer solution again in the supersonic regime. Otherwise, the neutral velocity solution will oscillate at this point because of the finite step size. These oscillations would have no physical meaning and can complicate the ion velocity solution as shown below.

3) Ideally, if the ion velocity derivative reverses sign, the conclusion is that the wrong initial condition has been employed, i.e., the parameter, A, was improperly chosen. The overall calculational scheme is to try a range of values for A until one is found that works. In practice, the finite step size makes this an impossible procedure. Instead, one terminates the computer solution just short of the singularity, extrapolates the velocity a short way by hand and starts the computer solution again. For all but a tiny range of A, the solutions will show that the derivative will still reverse, and these solutions can be thrown out immediately. The remainder will oscillate and then proceed downstream without reversal; i.e., the velocity continues to increase. One then chooses among these remaining solutions by picking the one with the least oscillation. It should be clear by now why it is undesirable to have any computer generated oscillation in the background flow solutions when one is finding the ion solutions.

Typically, the ion and neutral momentum equations are strongly coupled in the vicinity of either's sonic point, and thus the hand calculation to bridge these gaps is necessary to reduce unnecessary "fishing" for the correct pair of solutions on the computer. Presumably, one could program these logic steps and automate the whole procedure. This would be desirable if a large number of cases were to be investigated.

4) Once the sonic points for each species are established by this iterative procedure, the supersonic flow can be calculated in a straightforward way by the step-by-step procedure shown before.

D. BASIC EQUATIONS

The basic equations of quasi-one-dimensional, steady flow in hydrogen for the model outlined in Subsection B may be written using the following additional symbols:

n_j = number density of species j

Γ_j = particle flux

A = cross-sectional area per unit length

P_j = pressure

m_j = particle mass

k = Boltzmann's constant

M_{jk} = momentum transfer between j and k

ξ_A = atomic ionization energy

ξ_m = molecular ionization energy

ξ_D = dissociation energy

c_j = thermal velocity

Q_{jk} = momentum transfer cross section

B = applied axial magnetic field

B_θ = induced azimuthal magnetic field

μ = magnetic permeability

E = applied radial electric field

1. Continuity

ions/electrons

$$\frac{d\Gamma_e}{dx} = n_e n_H \alpha \mathcal{g}_A + n_e n_{H_2} \alpha \mathcal{g}_M - \frac{\Gamma_e}{A} \frac{dA}{dx} \quad \text{(A-27)}$$

atoms

$$\frac{d\Gamma_H}{dx} = n_e n_{H_2} \alpha \mathcal{g}_M + 2 n_e n_{H_2} \alpha (\mathcal{g}_{D_1} + \mathcal{g}_{D_2}) - n_e n_H \alpha \mathcal{g}_A - \frac{\Gamma_H}{A} \frac{dA}{dx} \quad \text{(A-28)}$$

molecules

$$\frac{d\Gamma_{H_2}}{dx} = -n_e\, n_{H_2}\, \alpha(g_M + g_{D_2}) - \frac{\Gamma_{H_2}}{A}\frac{dA}{dx} \qquad \text{(A-29)}$$

These equations show how the particle flux of each species is modified by reactions and area change.

2. Momentum

axial ion/electron

$$\frac{d}{dx}(m_i\,\Gamma_e\,U_i) + \frac{dP_e}{dx} + \frac{dP_i}{dx} = -M_{in} + j\,B_\theta \qquad \text{(A-30)}$$

$$+(n_e\, n_H\, \alpha\, g_A + n_e n_{H_2}\, \alpha\, g_M)\, m_i\, U_n - \frac{m_i\,\Gamma_e\,U_i}{A}\frac{dA}{dx}$$

The term M_{in} includes the charge exchange effects, while the term with g's accounts for the ionizatio: reactions in the presence of a velocity difference between species. The Lorentz force term will only be used in one case to be noted. This is likewise true of the Ampere Law to be given below.

axial neutral

$$(m_{H_2}\,\Gamma_{H_2} + m_H\,\Gamma_H)\,\frac{dU_n}{dx} + \frac{dP_H}{dx} + \frac{dP_{H_2}}{dx} = M_{in} \qquad \text{(A-31)}$$

azimuthal heavy

$$(m_{H_2}\,\Gamma_{H_2} + m_H\,\Gamma_H + m_i\,\Gamma_e)\,\frac{dU_s}{dx} = M_{es} \qquad \text{(A-32)}$$

azimuthal electron

$$jB = M_{es} \qquad \text{(A-33)}$$

The two relations above for azimuthal velocities are equivalent to conductivity formulas for the Hall currents. In treating the velocity components of each species separately, it is not necessary to explicitly compute Hall parameters. The term M_{es} is essentially a measure of the azimuthal conductivity and appears in the energy equation below as joule heating due to Hall currents.

3. Energy

electrons

$$3/2\,k \frac{d}{dx}(\Gamma_e T_e) + P_e \frac{dU_i}{dx} = -\frac{dq}{dx} + \frac{j^2}{\sigma} + M_{es}(U_e - U_s)$$

$$- n_e n_H \alpha g_A \xi_A - n_e n_{H_2} \alpha \left[g_M \xi_M + g_{D_1}(G_{eH} + \xi_D) + g_{D_2}(G_{eH} + G_R + \xi_D) \right] \tag{A-34}$$

$$- H_{eH} - \left[3/2\,k \Gamma_e T_e + P_e U_i + q \right] \frac{1}{A} \frac{dA}{dx}$$

heavy particle

$$\frac{d}{dx}\left[3/2\,k \Gamma_H T_H + 5/2\,k \Gamma_{H_2} T_H + 3/2\,k \Gamma_e T_H \right] + (P_H + P_{H_2}) \frac{dU_n}{dx}$$

$$+ P_i \frac{dU_i}{dx} = H_{eH} + M_{in}(U_i - U_n) \tag{A-35}$$

$$+ \frac{m_i}{2}(n_e n_H \alpha g_A + n_e n_{H_2} \alpha g_M)(U_n - U_i)^2$$

$$+ n_e n_{H_2} \alpha G_{eH}(g_{D_1} + g_{D_2})$$

$$- \left[3/2\,k \Gamma_H T_H + 5/2\,k \Gamma_{H_2} T_H + 3/2\,k \Gamma_e T_H + P_H U_n + P_{H_2} U_n + P_i U_i \right] \frac{1}{A} \frac{dA}{dx}$$

4. State

$$P_j = n_j k T_j \tag{A-36}$$

5. Ohm

$$j = \sigma(E - U_e B) \tag{A-37}$$

6. Ampere

$$\frac{dB_\theta}{dx} = -\mu j \tag{A-38}$$

7. Heat Flux

$$q = -\lambda \frac{dT_e}{dx} \tag{A-39}$$

8. Momentum Transfer

$$M_{es} = n_e c_e m_e (U_e - U_s) \sum_j n_j Q_{e_j} \tag{A-40}$$

$$M_{in} = n_e m_i (U_i - U_n) \sum_j \left[(4/3\ c_{ij})^2 + (U_i - U_n)^2 \right]^{1/2} n_j Q_{i_j} \tag{A-41}$$

The applied radial voltage in a magnetic annular arc has been found experimentally to obey the following characteristic[61]

$$V = V_o + U_c B l \tag{A-42}$$

where V_o is a constant that has been correlated with an electrode loss, and l is the gap distance from anode to cathode. This provides an applied radial electric field in the body of the gas equal to

$$E = U_c B \tag{A-43}$$

where the constant U_c has been found experimentally to be equal to the velocity that an ion must have for its kinetic energy to equal the ionization potential.

$$U_c = \left(\frac{2 \xi_I}{m_i} \right)^{1/2} \tag{A-44}$$

The physical significance of this result has been the subject of much discussion in the literature, and several theories have been advanced as an explanation.[62-65] It is not the purpose of the present paper to answer the interesting questions raised by the nature of this peculiar voltage, although the results of the analysis should be interesting to workers who are involved with the problem.

For purposes of the computation, the voltage will be taken as a boundary condition given by the experiment. That is, the applied radial electric field will be treated as a known parameter similar to applied magnetic field, gas pressure, etc. In Subsection H, some additional discussion on the relationship of the voltage to other boundary conditions will be given.

E. BOUNDARY CONDITIONS

The set of first order differential equations requires the specification of nine boundary conditions. Seven of these may be written down immediately as conditions on the flow upstream of the discharge

$$n_e \to 0;\ n_H \to 0;\ n_{H_2} \to n_o;\ T_H \to T_o \qquad \text{(A-45)}$$

$$q \to 0;\ U_s \to 0;\ U_n \to U_o$$

The two additional conditions can be found by linearizing the basic equations in the limit specified by the above requirements.

The result is an exponentially increasing solution for the electron density and another for the electron temperature

$$n_e = A_1\, e^{\xi_1 x} \qquad \text{(A-46)}$$

$$T_e = T_{eo} + A_2\, e^{\xi_2 x} \qquad \text{(A-47)}$$

$$\xi_1, \xi_2 = f(n_o, U_o, T_{eo}, T_o, E, B) \qquad \text{(A-48)}$$

$$A_1, A_2 = \textit{arbitrary constants} \qquad \text{(A-49)}$$

These results may be rewritten in the form

$$n_e = e^{\xi_1 (x - x_o)} \qquad \text{(A-50)}$$

$$T_e = T_{eo} + A\, e^{\xi_2 (x - x_o)} \qquad \text{(A-51)}$$

The reference val" of x is fixed by x_o and has no physical significance. However, the quantity A is important to the result and will be fixed by a sonic point condition to be discussed below.

A substitution of the density solution shows that the initial value for U_i must be zero if the incoming flow is not ionized. The initial value for T_e, T_{eo}, goes to the familiar value for the elevated electron temperature in a glow discharge. The latter corresponds to a single electron gaining energy from the electric field at the same rate that it loses energy by collisions with the background neutrals and is approximately proportional to E/P_o.

The two axial momentum equations possess sonic point singularities which impose a constraint on the solution similar to the initial value conditions. As in conventional nozzle calculations, certain terms in the momentum equation drive the flow towards the singularity while others drive it away. In order for a solution to traverse the singularity, these terms must exactly balance at the sonic point.

The dominant effect in the background neutral gas is a strong heating by the hot electrons. This is a force driving the flow towards the sonic point. The only term that is opposite in sign and large enough to balance the heating is the diverging area change in the nozzle. One then concludes something which is already intuitively obvious, that the neutral sonic point must be located at the throat. In practice the solution is carried out by assuming a constant area up to the singular point in the neutral equation; thence the known area divergence as a function of axial location is programmed, and the neutral solution automatically passes through the sonic point smoothly. For the ion/electron gas, the important term to consider is the momentum transfer due to slip between ions and neutrals. The only admissible solutions turn out to be those where this term is small at the sonic point. Essentially, one finds a diffusion solution in the subsonic regime with the ions pushing upstream against the incoming neutral gas. Near the sonic point the momentum transfer reverses sign, and the expansion of the hot electron gas in the area divergence forces the ions to pull the neutrals downstream. The particular ion/electron solution which has this behavior and thus properly traverses the sonic singularity defines the quantity A .

A complete solution is effected by an iteration procedure. The basic equations are integrated on a digital computer using a standard Runge-Kutta procedure for a range of values for A . The particular value which traverses the sonic singularity is the correct one.

F. RESULTS

The purpose of this section is to display the results of the numerical analysis in a manner that demonstrates consistency with the initial assumptions and reasonable connections with experimental data. The important physical processes will be identified which will be used in Subsection G to construct a simple flow model. Various constants that are required by the elementary model can then be found by matching to the numerical results in the present section. A gas pressure limitation on the analysis will be indicated, and some results that show the influence of insulators will also be indicated.

A typical solution for parameters corresponding to experiment[56] is shown in Figures A-2 through A-5. In Figure A-2, the radial electron current density and axial velocity of ions and neutrals is plotted as a function of distance. The relationship of the axial scale to the geometric throat is indicated above the curves. In Figure A-3, the electron and heavy species temperature is shown, while in Figure A-4, the flux of each species is given.

The important thing to note is that the major current carrying region is centered about the throat region. On the upstream side it is terminated by a decreasing electron density in an ambipolar diffusion regime. Downstream it is attenuated by the large Hall effect in the electron gas. The latter point is shown in Figure A-5, where tangential electron velocity as a percentage of the E/B speed is plotted.

The transition of the flow from an upstream regime of small Hall effect to one of large Hall effect at the throat is produced by heating. The resulting acceleration and decrease in background gas density yields a much reduced electron collision frequency. If the flow were to follow exactly the nozzle walls (as is shown for a distance of several millimeters in the plotted results), the enormous expansion would terminate the downstream currents in a very short distance.

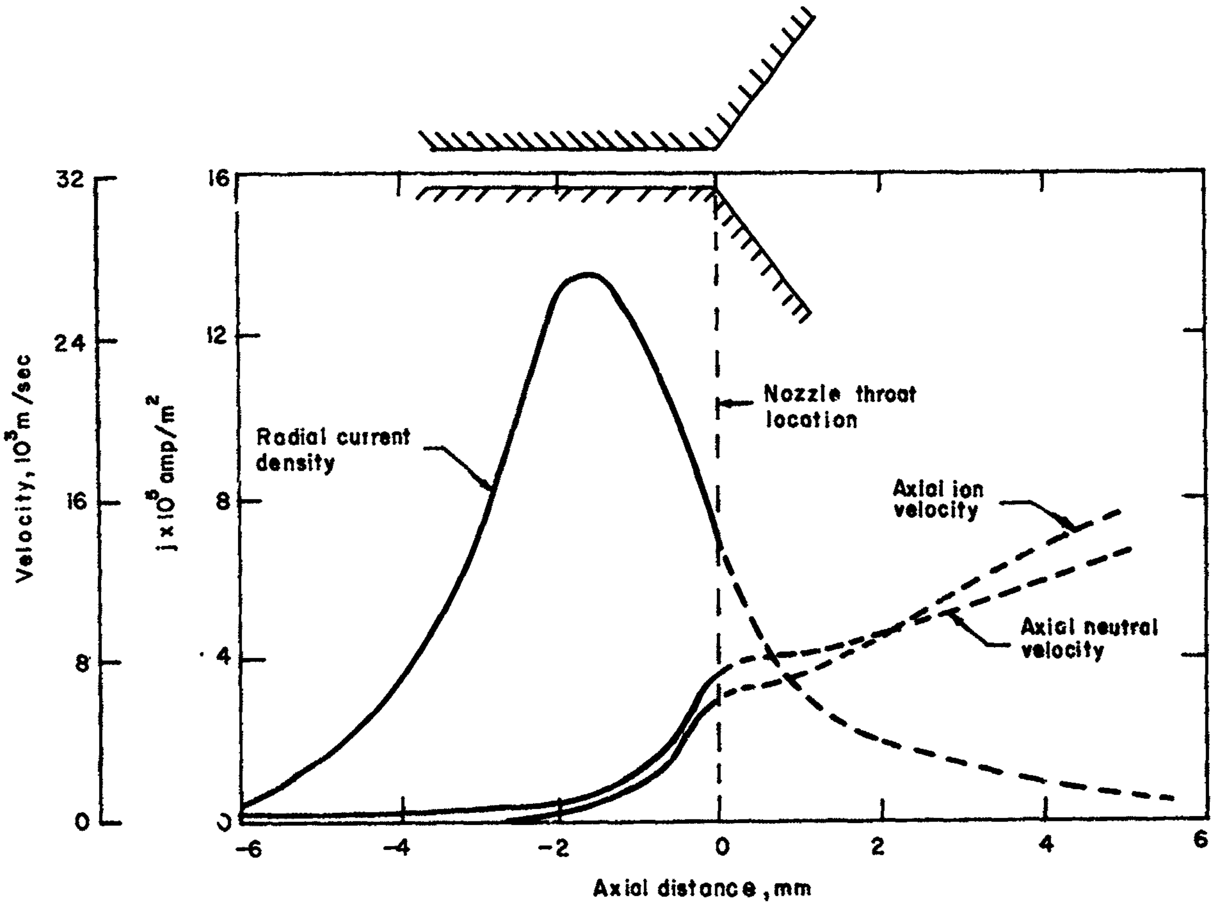

78-0147

Figure A-2 CURRENT DENSITY AND AXIAL VELOCITY DISTRIBUTION

Calculation for Reference 54 experiment, 0.05 g/sec. H_2, 1250 gauss, 230 amperes, 30 mm Hg. The supersonic region is shown dashed.

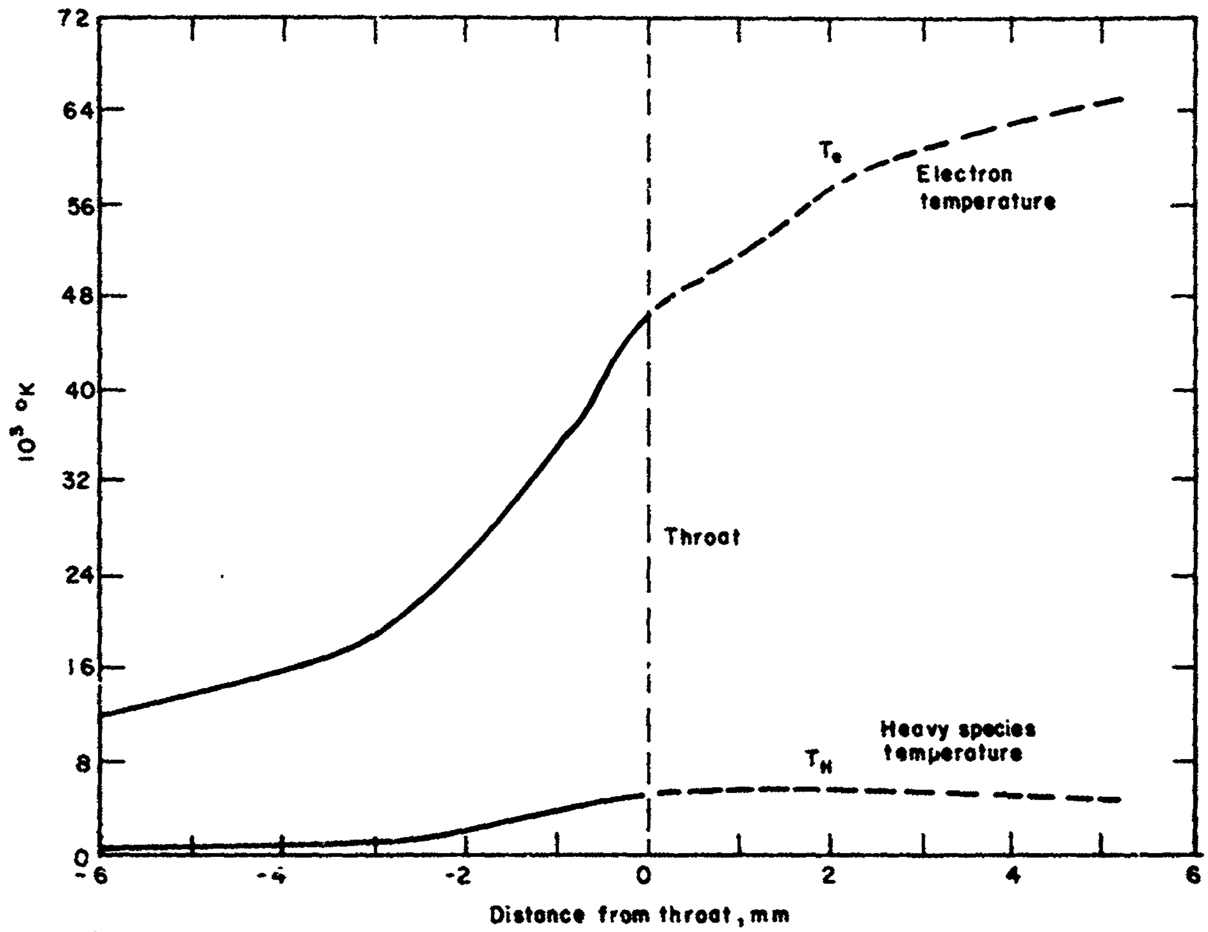

78-0148

Figure A-3 TEMPERATURE DISTRIBUTION

Calculation for Reference 54 experiment, 0.05 g/sec H_2, 1250 gauss, 230 amperes, 30 mm Hg. The supersonic region is shown dashed.

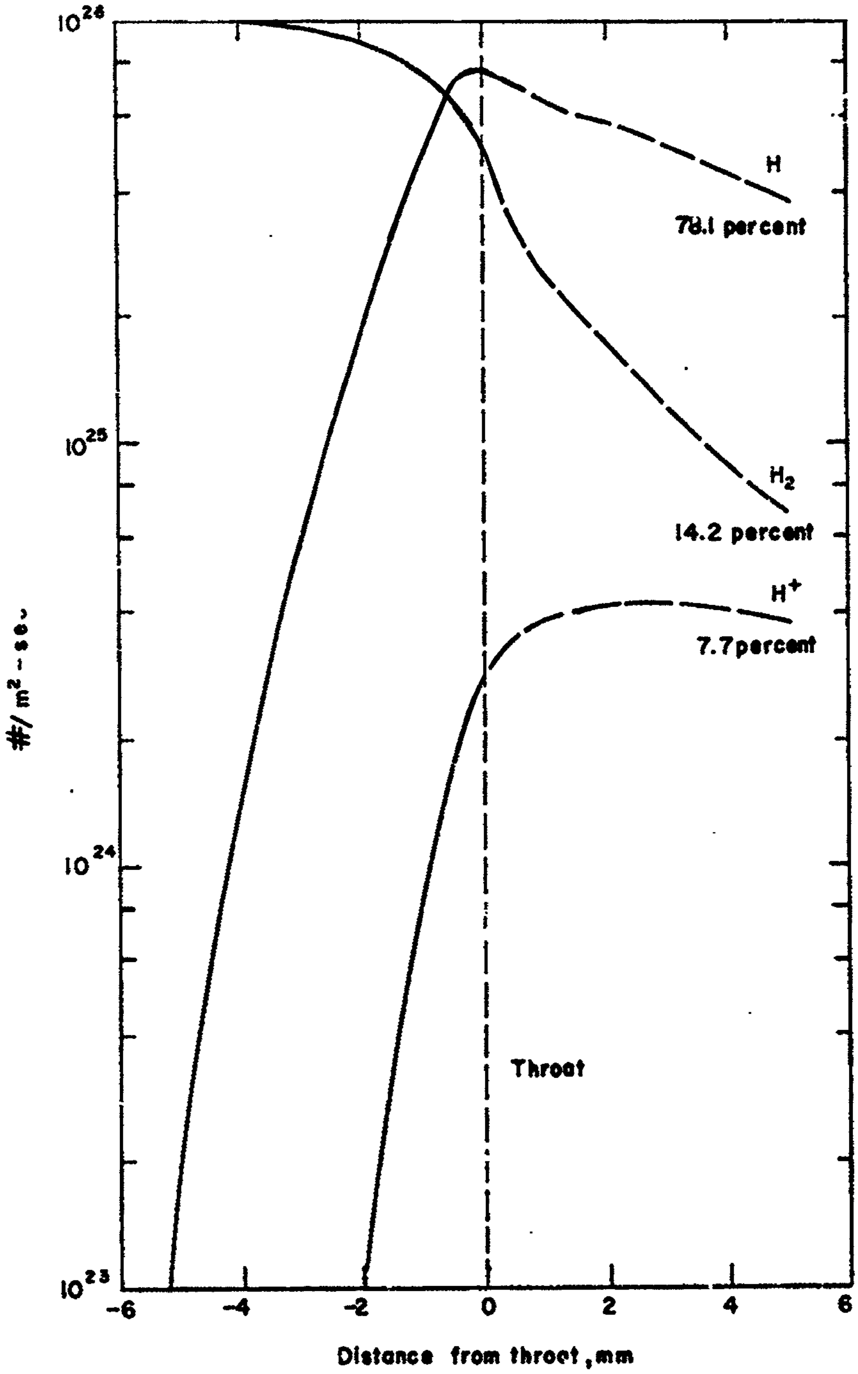

78-0149

Figure A-4 PARTICLE FLUX DISTRIBUTION

Calculation for Reference 54 experiment, 0.05 g/sec H_2, 1250 gauss, 230 amperes, 30 mm Hg. The supersonic region is shown dashed.

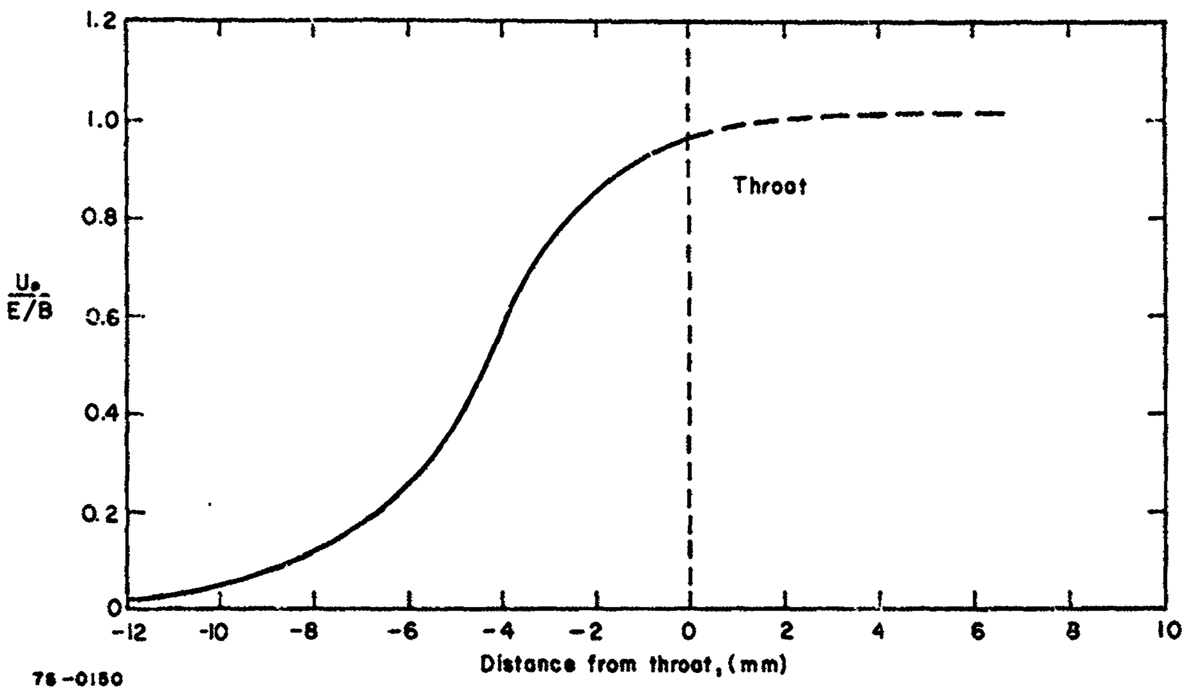

Figure A-5 HALL EFFECT, RATIO OF AZIMUTHAL ELECTRON VELOCITY TO E/B SPEED

Calculation for Reference 54 experiment, 0.05 g/sec H_2, 1250 gauss, 230 amperes, 30 mm Hg. The supersonic region is shown dashed.

Actually, the flow will probably be tied to a considerable extent to the magnetic field lines and will expand much less rapidly. This implies that while the current density itself will be considerably reduced from its maximum near the throat, the total current carried downstream (integrated over many centimeters) could be quite large. As stated before, it is not the purpose of this analysis to treat the complicated interactions between such currents, flow containment, and magnetic field geometry.

The interesting result of the present analysis is that a high current density structure has been found near the throat on a scale of millimeters, whereas the scale of the experiment is centimeters. Thus it appears that a solution consistent with the initial assumptions has been found.

Figure A-4 indicates that, even at the downstream end of the calculation, the fraction of ionized material is quite low (7.7 percent) which explains the relatively high efficiency of these arcs when used as thrust devices. The purpose of Table A-I is to show that approximately 50 percent of the electrical power into the gas at the sonic point is in the form of available thermal energy. This can be used to expand the gas to high velocities in an expansion nozzle. This value compares well with reported efficiencies of order 50 percent.[56] The axial velocities of the gas shown in Figure A-2, before complete expansion, are above 10^4 m/sec. This implies specific impulses in excess of 1000 seconds when the device is used for propulsion -- also in agreement with experiment.[56]

TABLE A-I

ENERGY DISTRIBUTION AT THE SONIC POINT

	Low Power Arc	
	0.05 g/sec Hydrogen	B=1250 gauss (axial)
Initial Pressure	30 mm Hg	60 mm Hg
Subsonic Current	170 amps	650 amps
Heating		
atom enthalpy	16.52 percent	24.5 percent
atom kinetic energy (axial)	5.15	8.22
molecule enthalpy	18.22	0.67
molecule kinetic energy (axial)	8.15	0.32
ion enthalpy	0.48	2.33
ion kinetic energy (axial)	0.085	1.21
electron enthalpy	4.64	13.4
	Σ = 53.24	Σ = 50.65
Swirl Kinetic Energy	0.52	1.99
Energy Losses		
dissociation	34.3	26.5
ionization	7.2	17.8
radiation	4.74	3.06
	Σ = 100.0 percent	Σ = 100.0 percent

While an arc solution is obtainable over a wide range of flow parameters, there does appear to be a low pressure cutoff. Attempts to carry out a calculation below this pressure result in a solution with orders of magnitude less current, producing a negligible effect on the background gas. The result is a structure that resembles a glow discharge. The difference between the two types of solution arises in the momentum relation for ions and electrons. It was pointed out in the discussion of boundary conditions that the momentum exchange between ions and neutrals is the important interaction which permits the growth of a diffusion region. As the ionization proceeds downstream, the diffusion layer acts as a containing wall for the ion/electron pressure in the major current carrying zone. However, as the initial pressure is lowered, the diffusion containment decreases while the rate of ionization increases. This is primarily because the initial electron temperature rises with decreasing pressure (being approximately proportional to E/P_o as noted earlier). The result is that below some pressure the ionization overwhelms the diffusion, and there is no steady solution resembling an arc discharge.

For the present calculations, the cutoff developed at an E/P_o of 5 to 10 v/cm-mm Hg. This happends to correspond to the value for diffusion controlled breakdown in hydrogen.[57] However, this point has not been pursued and may have no physical signficance. In the usual experiment, the mass flow and current are fixed instead of discharge pressure. Thus, the cutoff would be observed as a lower limit on the current. For example, experimentalists[66] have observed erratic behavior of the arc in a field of 1250 gauss at a mass flow of 0.05 g/sec for currents less than 100 amps. This is in agreement with the calculated E/P_o cutoff.

The geometric model for the analyses has assumed that the electrodes extend infinitely far upstream, whereas in experiments there may be insulators at some location. While the analytic result does show that electron density, current, etc. decay exponentially upstream from the throat on a scale of millimeters, it is interesting to see if this assumption has affected the result. This has been investigated by carrying out a solution for zero electric field, corresponding to an insulator region, and patching it to the usual solution in the vicinity of the throat. It was observed that there is a negligible effect on the earlier result as long as the patching is done upstream of the scale length for the major current carrying region. This is shown in Figure A-6 where the upstream current density with an insulator 5.7 mm from the throat is compared to the previous result from Figure A-2 with infinite electrodes. This conclusion is in agreement with the experimental observation* that the existence or location of an insulator is unimportant unless it is placed right at the throat. In the latter case, it burns back a few millimeters during initial arc operation, thence producing no subsequent effect on performance.

G. SIMPLE MODEL FOR ARC

A simple flow model can now be constructed for the subsonic region in the arc by emphasizing the important physical processes identified in the last

*A. M. Schneiderman, private communication.

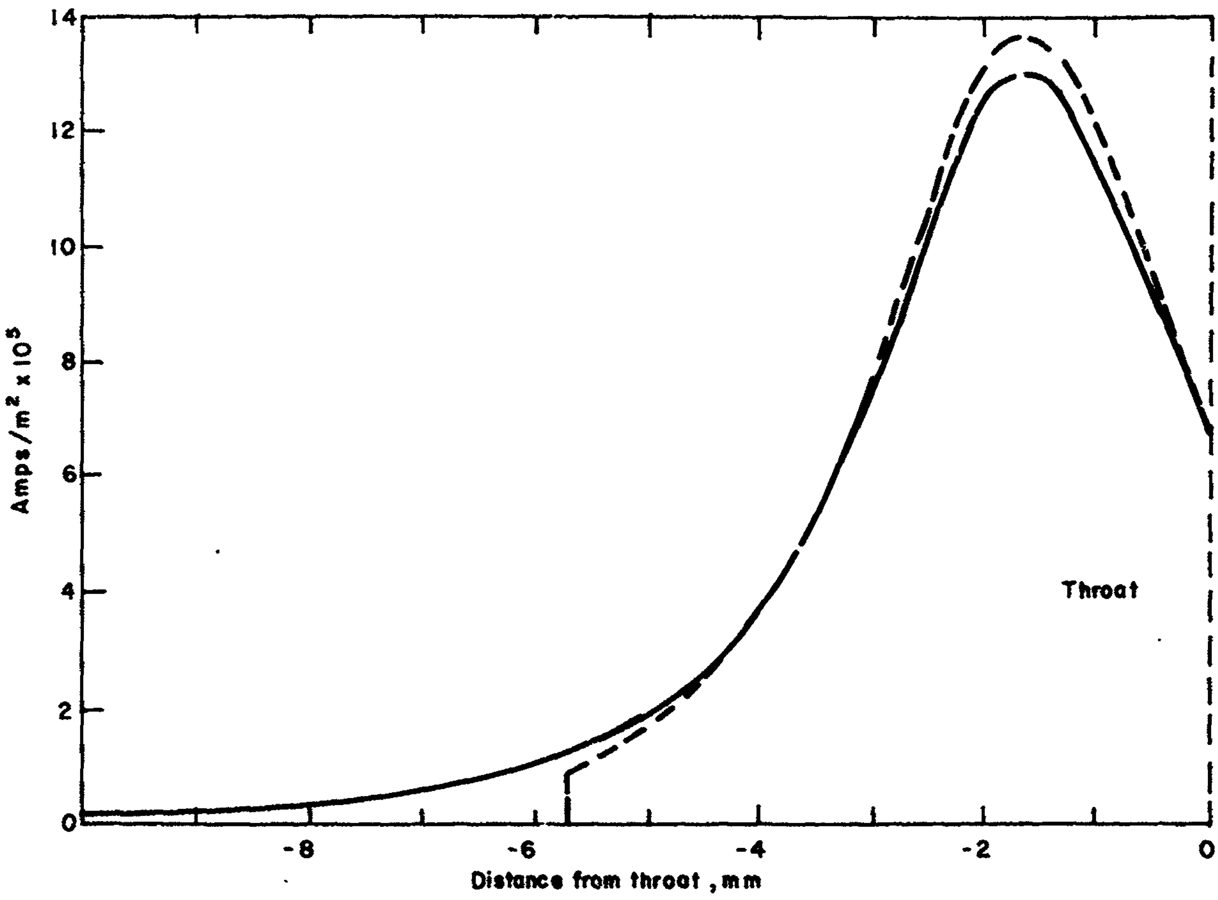

Figure A-6 EFFECT OF FINITE ELECTRODE LENGTH, RADIAL CURRENT DENSITY DISTRIBUTION

Calculation for Reference 54 experiment, 0.05 g/sec H_2, 1250 gauss, 30 mm Hg. Equal Integrated Subsonic Current of 170 amperes.

——————— infinite electrode

- - - - - - - - finite electrode

section. This flow region appears to be where the important ionization, current, and heating effects take place. Relationships will be developed which are useful in estimating the extent of the high current density zone and in predicting the fraction of gas ionized. Furthermore, an analogy to the familiar process of heat addition in a constant area duct permits the derivation of an important relationship between current and flow parameters. In each case, the numerical analysis can be used to provide certain parameters which would otherwise have to be ad hoc assumptions.

The arc structure itself is formed by the hot electron/ion gas diffusing relative to the background neutral flow. In steady state, the axial motion of the current carrying species is essentially stationary in laboratory coordinates with a diffusion velocity relative to the neutrals equal to the incoming flow velocity. This simple picture provides a characteristic diffusion length equivalent in scale to the size of the current carrying region. The length can be estimated by

$$L \approx \frac{D_a}{U_o} \qquad \text{(A-52)}$$

where D_a is the usual ambipolar diffusion coefficient and U_o is the incoming gas velocity. The formula can be fitted to give a length identical to the numerical results by choosing an electron temperature of 40,000°K and data from Brown.[57] Actually this value of temperature is quite reasonable when compared to either the numerical results for temperature or the available experimental data.[66] While there may be some ambiguity for a given case in choosing the exact values to compute the length, it should in any event provide better than an order of magnitude estimate.

This type of model can be used to even better advantage in estimating the relationship between current and flow parameters. The dominant energy process is the heating of the background gas by the electrons which in turn are heated by the passage of current. The amount of heating is proportional to the product of electron and neutral density. The current density is also proportional to the same product. The latter is the result of Hall current which makes the effective electrical conductivity directly proportional to collision frequency instead of the inverse, as in arcs with no magnetic field. This fortuitous proportionality permits a general relationship between the arc current and upstream flow parameters. The heating to bring the gas from some specified upstream mass flow and pressure (or Mach number) to sonic conditions is easily calculated from well known pipe flow tables (e.g., Shapiro[67]).

For a low Mach number gas flow into the arc, a simple relationship may be derived that includes the effect of magnetic pressure.

Conservation of axial mementum

$$P_o + \Delta P_m = P_* + \dot{m} U_* \qquad \text{(A-53)}$$

Conservation of energy

$$Q_o = \dot{m} C_p T_* + 1/2\, \dot{m} U_*^2 \qquad \text{(A-54)}$$

where Q_o is the subsonic heating, P_o is initial gas pressure, ΔP_m is the change in axial magnetic pressure, $\dot{m}$ is the mass flow, C_p is specific heat at constant pressure, and P_* , T_* , U_* are pressure, temperature, velocity at the sonic point. Noting that

$$P_* = \frac{\dot{m}}{U_*} RT_* \qquad \text{(A-55)}$$

$$U_*^2 = \gamma RT_* \qquad \text{(A-56)}$$

where R is the perfect gas constant and γ is the specific heat ratio, the equations can be combined to give

$$Q_o = \frac{k}{\dot{m}} (P_o + \Delta P_m)^2 \qquad \text{(A-57)}$$

with

$$k = \frac{\gamma^2}{2(\gamma^2 - 1)} \qquad \text{(A-58)}$$

Now, if the fraction of electrical energy that goes into heating is known and some reasonable γ corresponding to the reacting flow is assigned, a unique relationship exists between current, mass flow, and upstream pressure.

For the range of currents considered in the numerical analysis corresponding to the MAARC experiments[56] (where induced magnetic effects are unimportant and have been neglected), the heating fraction turns out to be approximately 50 percent. Table A-I indicates the energy accountability for two cases at the same mass flow and magnetic field, but different currents. Knowing the fraction of energy that goes into heating, it is possible to pick a value for γ that permits the simple formula to match exactly the numerical results. This value turns out to be 1.13. If one recalls that, whereas the γ for hydrogen is 1.4 at room conditions, it reduces to approximately 1.05 during ionization in thermodynamic equilibrium,[68] the effective value of 1.13 for the non-equilibrium process in the arc is perfectly reasonable. Note in Table A-I that doubling the initial pressure essentially quadruples the current carried as predicted by these elementary considerations.

To test the range of applicability of the model, a calculation was carried out for the solar wind tunnel arc source.[47] This is a much higher power device which relies on strong induced magnetic fields to propel the gas. In addition, the exhaust is almost fully ionized (compared to the usual small degree of ionization). The analytical procedure had to be modified to include the axial Lorentz force or magnetic pressure change shown in Equation A-5).

The important differences between the results of this calculation and previous results are shown in Figure A-7 and Table A-II. The gas is fully ionized at the sonic point, and the energy per particle as indicated by the electron temperature is much higher than in the low power devices. One should note that, while the fraction of energy lost to ionization and dissociation is down from the earlier calculations, much of the difference has been absorbed in swirl energy.

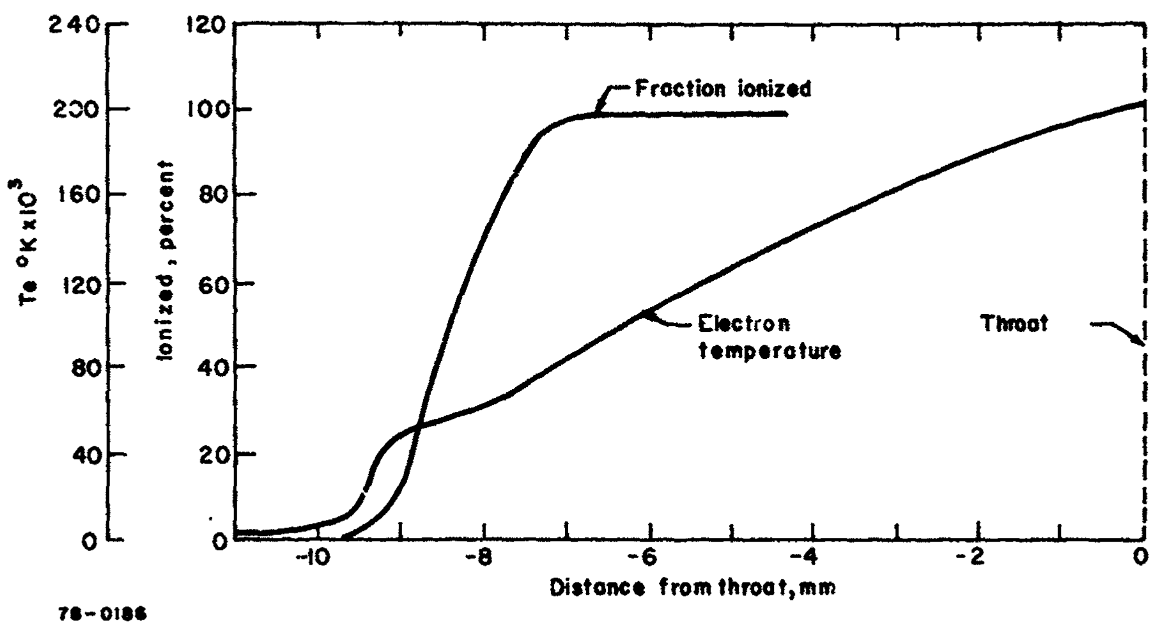

Figure A-7 ELECTRON TEMPERATURE AND FRACTION IONIZED DISTRIBUTION, HIGH POWER MAGNETIC ANNULAR ARC (SOLAR WIND TUNNEL)

Calculation for Reference 45 experiment, 1.0 g/sec H_2, 4000 gauss (axial), 6000 gauss (azimuthal), 660 mm Hg, 20,200 amperes (subsonic current)

TABLE A-II

ENERGY DISTRIBUTION AT THE SONIC POINT

High Power Arc

1.0 g/sec Hydrogen   B = 4000 gauss (axial)

B_θ = 6000 gauss (tangential)

Initial Pressure	660 mm Hg
Subsonic Magnetic Pressure	1040 mm Hg
Subsonic Current	20,200 amps
Heating	
ion enthalpy	16.4 percent
ion kinetic energy (axial)	10.6
electron enthalpy	36.2
	Σ = 63.2
Swirl Kinetic Energy	23.8
Energy Losses	
dissociation	1.8
ionization	10.8
radiation	0.4
	Σ = 100.0 percent

At this point it is interesting to compare the computer calculations for pressure, mass flow, and current with the simple scaling relationship developed for the low power arc. Compared to the 60 mm Hg calculation for the smaller device, the mass flow per unit area in the solar wind tunnel is 6.82 times higher, and the subsonic power is 141 times higher.

The simple scaling then would estimate the initial pressure to be 31 times higher or 1860 mm Hg. In the actual computer result, it was found that this power and mass flow in wind tunnel correspond to an initial gas pressure of 660 mm Hg and a change in axial magnetic pressure of 1040 mm Hg for a total of 1700 mm Hg. Thus the simple estimate comes within 10 percent of the detailed calculation even for this large extrapolation.

The flow model for the magnetic annular arc that has emerged from these calculations demonstrates the interconnections between mass flow, pressure, and electrical heating. Unfortunately, to date, experimental information is not available to confirm these relationships. While current, voltage, and mass flow are frequently well known, the pressure at the leading edge of the discharge has not been monitored to the author's knowledge. Typically, the gas pressure is known only at some upstream station separated by orfices and frictionally choked passages from the discharge itself. It is hoped that this paper will inspire future experiments to correct this omission.

For many experiments, where the magnetic annular arc is used as a plasma source to perform flow studies, it is desirable to know the fraction of gas that has been ionized. One can derive an approximate relationship from the present results that can be useful in making such an estimate. If half of the electrical power, W, goes into processes not related to heating and if the gas is taken to be fully dissociated, an energy equation can be written

$$1/2\, W = m(\xi_D + a\, \xi_I + \frac{1}{2}\, U_s^2) \qquad \text{(A-59)}$$

where m is mass flow, ξ_D is dissociation energy, a is ionization fraction, ξ_I is ionization energy, and U_s is swirl velocity. The swirl velocity can be obtained from the azimuthal momentum balance as

$$IBl = m U_s \qquad \text{(A-60)}$$

where I is total current, B is the applied axial magnetic field, and l is the electrode gap. Substituting one obtains

$$c = \frac{1}{\xi_I} \left[\frac{W}{2\dot{m}} - \xi_D - \frac{1}{2} \left(\frac{IBl}{\dot{m}},\right)^2\right] \qquad \text{(A-61)}$$

This formula is probably not useful for cases where the ionized fraction is less than 5 percent because of various neglected effects such as partial dissociation and radiation. It should in all cases, however, provide a guideline for evaluating the parametric behavior of this quanity where none now presently exists.

H. SUPERSONIC REGIME

Downstream of the throat, the simplest picture of the flow that emerges from the results is an expansion and acceleration of hot gas in a nozzle. Part of the acceleration is produced by the electron pressure gradient in the manner suggested by Bowditch[69] for low density plasma accelerators. This picture of the flow eliminates the need to consider the "excess" ion velocities that have been discussed in the literature (e.g., Burlock, et al.[66]). These anomalous velocities result from analyzing the device as an ion particle accelerator and thus trying to connect the exit plane ion energy with the voltage across the electrodes. In fact, since the high velocites can be generated by a hot gas expansion where the energy has been supplied by electron current, the acceleration need have nothing to do with individual ions falling through an applied potential.

While the qualitative features of the supersonic flow are clear, the details of the expansion still appear quite complicated. The gas possesses both swirl and axial velocity and will in some sense follow magnetic field lines instead of nozzle walls. With the electrons bound to the field by strong Hall currents, one can anticipate a complicated diffusion pattern in the radial direction. As the flow approaches the cathode tip, there should be an inward pinching of the electron species which is opposed by the swirling heavy species trying to diffuse outward. Momentum measurements[56] in the discharge plasma plume clearly indicate such processes take place. In addition, there may be collective plasma effects which produce anomalous electron currents in this regime. Clearly, the treatment of all these processes would require a two- or three-dimensional flow analysis and is definitely outside the scope of the present work.

In not carrying the solution through the supersonic regime, the question arises whether any downstream boundary conditions are being neglected which affect the overall solution. Actually, however, there is only one such condition that is free. This is the temperature or heat flux for the electron gas which might be assigned some particular value at a specified to downstream location. The remaining variables which are tied to the heavy species are separated from the downstream conditions by the sonic singularities as in conventional aerodynamics.

The heat flux boundary condition can be associated with the arc voltage. Indeally, a complete analysis should result in this voltage being an eigenvalue. This would be determined from the particular solution which satisfies all of the boundary conditions on the problem -- including the downstream heat flux. The tacit assumption is being made in the present work that specifying the voltage with the experimental value is equivalent to properly imposing the heat flux boundary condition. The most reasonable criterion to establish is that the heat flux tends to zero at large distances downstream. This implies that the electron gas will be locally satisfying some form of energy balance. Thus, if one could demonstrate that in the low density part of the discharge (electron cyclotron frequency large compared to collision frequency) an energy balance demands this particular voltage, the circle would be closed and the entire calculation scheme would be self-consistent. In fact, the various theories of the voltage characteristic[62-65] present such a balance as the explanation. Future work might be able to integrate the results of such a theory directly into the analysis.

I. SUMMARY

The structure of an arc in a magnetic annular discharge in hydrogen has been computed numerically using non-equilibrium, quasi-one-dimensional multicomponent hydrodynamics. The analysis substantiates recent experimental observations of a narrow current and ionization zone near the throat that is distinct from the complicated flow in the supersonic expansion. The numerical results suggest a simple diffusion and heating model for the subsonic portion of the arc. This model gives the important physical processes and permits the development of elementary relations which are useful for estimating parametric behavior. Specifically, formulas are derived giving the scale length of the discharge, fraction ionized, and the relationship between electrical power and flow parameters. Certain constants that are needed by the simple model are deduced by matching the results to the numerical analysis.

Using the present work as a boundary condition, future analytic work should be able to concentrate on the geometrical treatment of the interaction of plasma and magnetic field in the supersonic expansion. An outline of the relationship of the various electron energy balance theories of the voltage characteristic to these numerical hydrodynamic calculations has been presented.

REFERENCES

1. Finger, and Shulman, in Space Power Systems, Academic Press, p. 616 (1961).

2. Lazar, J., and J. P. Mullin, "A Review of the Role of Electric Propulsion," Paper 66-1025, AIAA Third Annual Meeting (1966).

3. Ritchie, D., P. Toms, and W. Menetrey, "Potentials of Solar Power for Electric Propulsion," Paper 66-210, AIAA Fifth Electric Propulsion Conference (March 1966).

4. Ramirez, P., and D. Tollefson, "Design and Analysis of Power Conditioning for Ion Propulsion Systems," Paper 66-215, AIAA Fifth Electric Propulsion Conference (March 1966).

5. Molitor, J. H., D. Berman, R. L. Selizer, and R. N. Olson, "Design of a Solar-Electric Propulsion System for Interplanetary Spacecraft," Paper 66-215, AIAA Fifth Electric Propulsion Conference (March 1966).

6. Ducati, A., C. M. Giannini, and E. Muehlberger, "Experimental Results in High Specific Impulse Thermo-Ionic Acceleration," AIAA J. 2, 1452-54 (1964).

7. Cann, G. L., "Annular Magnetic Hall Current Accelerator," Paper 64-670, Fourth Electric Propulsion Conference, Philadelphia, Penn. (August 1964).

8. Kelly, A. J., N. M. Nerheim, and J. A. Gardner, "Electron Density and Temperature Measurements in the Exhaust of an MPD Source," AIAA Fifth Electric Propulsion Conference, San Diego (March 1966).

9. Grossman, W., H. A. Hassan, R. V. Hess, and G. Oertel, "Experiments with a Coaxial Hall Current Plasma Accelerator," Paper 64-697, Fourth Electric Propulsion Conference, Philadelphia, Penn. (August 1964).

10. Hess, R. V., "Fundamentals of Plasma Interaction with Electric and Magnetic Fields," Paper 59, Vol. 2, Proceedings of the NASA University Conference on the Science and Technology of Space Exploration (November 1963).

11. Seikel, G. R., and E. Reshotoko, "Hall Current Ion Accelerator," Bul. Am. Phys. Soc., 7, No. 6 (1962).

12. Powers, W. E., and R. M. Patrick, A Magnetic Annular Arc, Avco Everett Research Laboratory Report RR-129 (May 1962).

13. John, R. R., Bennett, S., and Connors, J. F., "Experimental Performance of a High Specific Impulse Arcjet Engine," Astronautica Acta, 11, 97 (1965).

14. Bennett, S., R. R. John, G. Enos, and A. Tuchman, "Experimental Investigation of the MPD Arcjet," Paper No. 66-239, AIAA Fifth Electric Propulsion Conference, San Diego (March 1966).

15. W. E. Moeckel, "Promises and Potentialities of Electric Propulsion Status of Thrustor Performance," Paper 66-1024, AIAA Third Annual Meeting (December 1966).

16. Ducati, A. C., G. M. Giannini, and E. Muehlberger, "Recent Progress in High Specific Impulse Thermoionic Acceleration," Paper 65-96, AIAA Second Aerospace Sciences Meeting (January 1965).

17. Avco/RAD Arcjet Technology Research and Development, Final Report, NASA CR-54687, RAD-TR-65-37, Contract NAS 3-5900 (December 1965).

18. Jones, R. E., and E. L. Walker, "Status of Large Vacuum Facility Tests of MPD Arc Thrustor," Paper 66-117, AIAA Third Aerospace Sciences Meeting (January 1966).

19. Malliaris, A. C., Interaction of a High Current Electrical Discharge with its Self-Induced Magnetic Field in the Pressure of Gas Flow, Final Report, AVMSD-0085-67-RR, Contract AF33(657)-11310 (March 1967).

20. Schneiderman, A. M., and R. M. Patrick, "Optimization of the Thermal Efficiency of the Magnetic Annular Arc," AIAA J. 4, 1836 (1966).

21. Avco/RAD Thirty Kilowatt Plasmajet Rocket Engine Development, Third Year Development Program Summary Report, NASA-CR-54079, RAD-TR-64-42, Contract NAS 3-2593 (July 1964).

22. Schneiderman, A. M. and R. M. Patrick, "Axial Current Distribution in the Exhaust of the Magnetic Annular Arc," AIAA J. 5, 249 (1967).

23. Powers, W. E., "Measurements of the Current Density Distribution in the Exhaust of an MPD Arcjet," AIAA J. 5, 545 (1967).

24. Brown, S. C., Basic Data of Plasma Physics, MIT Press (1959).

25. Massey, H., and E. Burhap, Electronic and Ionic Impact Phenomena, Oxford Press (1952).

26. Spitzer, L., Physics of Fully Ionized Gases, Interscience, New York (1956).

27. Powers, W. E., "Measurements of the Current Density Distribution in the Exhaust of an MPD Arcjet," Paper 66-116, AIAA Third Aerospace Sciences Meeting (January 1966).

28. Patrick, R. M., and A. M. Schneiderman, "Performanc Characteristics of a Magnetic Annular Arc," AIAA J. 4, 283 (1966).

29. Shapiro, A. H., The Dynamics and Thermodynamics of Compressible Fluid Flow, Ronald Press (1954).

30. Bowditch, D. N., "Investigation of the Discharge and Exhaust Beam of a Small Arc Plasma Thrustor," NASA Report TMX 52175 (1966).

31. Burlock, J., P. Brockman, R. V. Hess, and D. R. Brooks, "Measurement of Velocities and Acceleration Mechanism for Coaxial Hall Accelerators," AIAA J. 5, 558 (1967).

32. Petschek, H. E., Rev. Mod. Phys. 32, 712 (1960).

33. Lin, S. C., Phys. Fl. 4, 1277 (1961).

34. Dobryshevskii, E. M. (English Translation), Soviet Phys. - Tech. Phys. 8, 903 (1964).

35. Fabry, Eclairage Electrique 17, 133 (1898).

36. Bitter, Rev. Sci. Instr. 7, 482 (1936).

37. Johansen, presented at AIAA 5th Aerospace Sciences Meeting (1967).

38. Cockcroft, Phil. Trans. Roy Soc. 227, 235 (1928).

39. Bennett, S, W. Huss, R. R. John, and A. Tuchman, "Experimental Propulsion Performance of a Low Power Pulsed Resistojet," Paper 65-97, AIAA Second Aerospace Sciences Meeting (January 1965).

40. Powers, W. E., and R. M. Patrick, Phys. Fluids 5, 1196 (1962).

41. Patrick, R. M., and W. E. Powers, "Plasma Flow in a Magnetic Annular Arc Nozzle, Advanced Propulsion Concepts," Proceedings of the Third Symposium, Vol. 1, 115 (Gordon and Breach, N. Y., 1963).

42. Brockman, P., R. V. Hess, F. W. Bowen, and O. Jarrett, AIAA J. 4, 1209 (1966).

43. Cann, G. L., AIAA Paper 64-670 (1964).

44. Ducati, A. C., G. M. Giannini, and E. Muehlberger, AIAA Paper 64-668 (1964).

45. Patrick, R. M., and E. R. Pugh, Avco Everett Research Laboratory Research Report 268 (1967).

46. Fahleson, U. V., Phys. Fluids 4, 123 (1961).

47. Baker, D. A., J. E. Hammel, and F. L. Ribe, Phys. Fluids 4, 1534 (1961).

48. Heywood, J. B., Phys. Fluids 9, 1150 (1966).

49. Hess, R. V., "Experiments and Theory for Continuous Steady Acceleration of Low Density Plasma," Proc. of XI International Astronautical Congress, Vol. 1, pp. 404 to 411 (Stockholm, 1960).

50. Cann, G. L., and G. L. Marlotte, AIAA J. 2, 1234 (1964).

51. Hugel, H., G. Kruelle, and T. Peters, AIAA J. 5, 551 (1967).

52. Rosciszewski, J., Phys. Fluids 10, 1095 (1967).

53. Lovberg, R. H., "Proceedings of the Sixth International Conference on Ionization Phenomena in Gases," P. Hubert, E. Cremieu-Alcan, Vol. IV, 235 (Paris, 1963).

54. Schneiderman, A. M., and R. M. Patrick, AIAA J., 5, 249 (1967).

55. Powers, W. E., AIAA J., 5, 545 (1967).

56. Patrick, R. M., and A. M. Schneiderman, AIAA J., 4, 283 (1966).

57. Brown, S. C., Basic Data of Plasma Physics (MIT Press, 1959).

58. Massey, H., and E. Burhap, Electronic and Ionic Impact Phenomena (Oxford Press, 1952).

59. Spitzer, L., Physics of Fully Ionized Cases, Interscience (New York, 1956).

60. Dalgarno, A., and H. Yadav, Proc. Phys. Soc., A66, 173 (London, 1953).

61. Schneiderman, A. M., and R. M. Patrick, AIAA J., 4, 1636 (1966).

62. Petschek, H. E., Rev. Mod. Phys. 32, 712 (1960).

63. Lin, S. C., Phys. Fluids, 4, 1277 (1961).

64. Dobryshevskii, E. M., (English Translation) Soviet Phys. - Tech. Phys., 8, 903 (1964).

65. Hassan, H. A., Phys. Fluids, 9, 2077 (1966).

66. Burlock, J., P. Brockman, R. V. Hess, and D. R. Brooks, AIAA J. 5, 558 (1967).

67. Shapiro, A. H., The Dynamics and Thermodynamics of Compressible Fluid Flow, Ronald Press (New York, 1953).

68. Bosnjakovic, F., Aeronautical Research Laboratories Report ARL 62-359 (1962).

69. Bowditch, D. N., NASA Report TMX 52175 (1966).